MASTER

# Modelling of atmospheric pressure high current diffuse dielectric barrier discharges in a roll-to-roll geometry

van 't Veer, Kevin C.

*Award date:*
2018

Eindhoven University of Technology
Department of Applied Physics
Elementary Processes in Gas Discharges

# Modelling of atmospheric pressure high current diffuse dielectric barrier discharges in a roll-to-roll geometry

Kevin van 't Veer

September, 2018

EPG 18_14

*Supervisors:*
M.Sc. Y. Liu (DIFFER)
dr. ir. H. W. de Vries (DIFFER)
dr. D.B. Mihailova (Plasma Matters B.V.)
dr. ir. J. van Dijk (Eindhoven University of Technology)


FUJIFILM
Value from Innovation


TU/e
Technische Universiteit
Eindhoven
University of Technology
Where innovation starts


Plasma Matters.


DIFFER
Dutch Institute for
Fundamental Energy Research

# Summary

Recent experimental work, individually investigating the plasma expansion and its excitation under simultaneous low frequency and radio frequency applied voltages for atmospheric pressure dielectric barrier discharges in thin film deposition relevant roll-to-roll plasma reactors, would benefit from specific modelling due to the novelty of those geometries and tendency to use more economical gas mixtures, among others.

In the present study this is achieved by employing both one-dimensional and two-dimensional drift-diffusion plasma models from the PLASIMO plasma simulation & modelling toolkit. Specific goals are to gain a better understanding of the plasma expansion and formation mechanisms in roll-to-roll geometries as well as to gain understanding of the plasma parameters during dual frequency excitation.

In order to achieve those goals a model for an atmospheric pressure dielectric barrier discharge operating in argon is constructed (that is able to model a wide range of discharges). Mostly the retrieved discharge characteristics under low frequency excitation were found to represent an atmospheric pressure glow discharge. Both single peak and multi-peak discharge and current characteristics are observed – depending on the applied voltage and input parameters that are more fundamental to plasma physics such as the secondary electron emission coefficients and the metastable-metastable ionization rate coefficient.

It was found that metastable-metastable ionization is responsible for the local formation of a positive column. The required metastables are created during the preceding half cycle during which locally a cathode fall area existed momentarily where excitation took place. The existence of the positive column causes a memory charge effect which in turn causes the subsequent breakdown to occur at a reduced external applied voltage. Under those conditions the gas voltage is able to again exceed the breakdown voltage, causing a multi-peak behavior in the discharge and current characteristics.

The discharge has also been considered from a very first breakdown, which is identified as a Townsend breakdown. The later breakdowns in steady state are not developing in a same manner. This modelling approach is a requirement for the specific modelling of the roll-to-roll geometries for which the plasma was observed to expand over multiple cycles to an eventual width. In both one-dimensional and two-dimensional modelling the same atmospheric pressure glow was observed. In the latter the negative glow features were seen to expand laterally along the dielectric surfaces. It is assumed that this phenomenon causes the first peak in the current characteristics to be less pronounced compared to one-dimensional modelling results. This observation from modelling makes comparisons to experimental current characteristics non trivial despite very good agreements in other spatially resolved model output and related experimental observations.

# Samenvatting

Onlangs uitgevoerd experimenteel onderzoek, waarin afzonderlijk van elkaar de plasma expansie en de plasma excitatie bij het gelijktijdig aanbieden van een laag frequente en een radio frequente spanning in specifieke plasmareactoren relevant voor het deponeren van dunne films is onderzocht, heeft baat bij het specifiek modelleren van deze plasma's als gevolg van, onder andere, de noviteit van de gekromde geometrieën in deze plasmareactoren en de neiging naar het gebruik van meer economische gas mengsels.

In de huidige studie wordt dit bereikt door gebruik van zowel de één als twee dimensionale drift-diffusie plasma modellen uit de PLASIMO simulatie & modelleringsomgeving. De specifieke doelen zijn om een beter begrip te krijgen van de plasma expansie en formatie mechanismen in de plasma reactoren met gekromde elektroden en om meer inzicht te krijgen in plasma eigenschappen tijdens excitatie met twee frequenties.

Om dit te bewerkstelligen is een model opgezet voor een diëlektrische barrière ontlading werkend onder atmosferische druk en opererend in argon gas om een breed scala aan relevante ontladingen te modelleren. In de meeste gevallen bleek de ontlading een glimontlading onder atmosferische druk te vertegenwoordigen. Zowel enkele als meerdere pieken in de ontlading en stroomkarakteristieken zijn waargenomen. Dit was afhankelijk van de aangelegde spanning en ook input parameters voor het model die meer fundamenteel zijn in de plasma fysica zoals de emissie coëfficiënt van secundaire elektronen en de snelheid coëfficiënt voor de ionisatie tussen twee metastabiele atomen.

Het bleek dat de ionisatie tussen twee metastabiele atomen verantwoordelijk is voor de lokale formatie van een positieve kolom. De benodigde metastabiele atomen worden gecreëerd gedurende de vorige halve cyclus van de spanning waar zich plaatselijk en tijdelijk een kathode gebied met verval van het elektrisch potentiaal bevond. Hier vindt excitatie van atomen in de grondtoestand plaats. De gevormde positieve kolom zorgt voor een lading gerelateerd geheugeneffect welke ervoor zorgt dat de volgende gasontlading bij een lagere extern opgelegde spanningen kan plaatsvinden. Onder deze omstandigheden is de potentiaalverdeling over het gas zodanig dat het gas opnieuw doorgeslagen kan worden. Dit zorgt voor meerdere pieken in zowel de ontlading als stroomkarakteristieken.

De gasontlading is ook gemodelleerd vanaf een daadwerkelijke eerste ontlading welk geïdentificeerd werd als een Townsend ontlading. De latere ontladingen in de stabiele toestand ontwikkelen zich niet op de zelfde manier. Deze aanpak van modelleren is noodzakelijk voor het modelleren van de plasma expansie bij gekromde elektroden waarbij het plasma zijn uiteindelijke breedte bereikte over meerdere perioden van de aangelegde spanning. In zowel het één als twee dimensionaal modelleren werd de atmosferische glimontlading waargenomen. In het laatste geval bleek de negatieve gloed van de glimontlading zich lateraal te expanderen langs de diëlektrische barrières. Het wordt aangenomen dat dit verschijnsel ervoor zorgt dat de eerste piek in de stroomkarakteristieken minder uitgesproken is in vergelijking met het één dimensionale geval. Deze observatie maakt dat vergelijkingen met experimenteel verkregen stroomkarakteristieken niet triviaal zijn. Dit ondanks de zeer goede overeenkomsten die waargenomen zijn tussen het experimentele plasma en de uit het model verkregen ruimtelijke plasma eigenschappen.

# Acknowledgements

I would like to thank from DIFFER, Hindrik de Vries for accepting me for this position and Yaoge Liu for his guidance and enthusiasm, from the Eindhoven University of Technology, Jan van Dijk for his guidance and care over the past period and Leroy Schepers for his time and help related to oxygen modelling attempts. Sergey Starostin, from FujiFilm Manufacturing Europe B.V., for his fresh input and enthusiasm and from Plasma Matters B.V., Diana Mihailova for her time in explaining PLASIMO and her critical feedback on early models, Wouter Graef for helping me run PLASIMO and for the small discussions very early on in this project, Jesper Janssen for his extremely clear explanations and all members of the PLASIMO meeting for thinking along.

# Contents

# 1. Introduction (dielectric barrier discharges)

A dielectric barrier discharge is a specific type of plasma. Most generally two opposing electrodes are used, covered with a dielectric barrier. One electrode can be grounded and the other has a time-varying voltage applied, such as sinusoidal. At some point the discharge gas breaks down, due to a high enough electric field, and a plasma is formed. The current through the plasma now deposits charge on the dielectric barrier where it accumulates, causing the electric field between the electrodes to reduce and the plasma to extinguish. This process is then repeated during the next half cycle and the plasma is formed again, in principle inverted between the electrodes. This process continues, effectively maintaining the dielectric barrier discharge.

The dielectric barrier discharge (DBD) is a possible plasma source at atmospheric pressure (AP) with many applications caused by the, ongoing, increasing understanding of the beneficial diffuse AP DBD. Applications include sterilization, plasma medicine and surface modification [1]–[7]. These applications are in part possible due to the AP DBD being able to provide a plasma at relatively low gas temperatures while electrons are still highly energetic.

Starostin et al. [8] have shown the deposition of moisture barrier layers on polymeric substrates using an AP DBD in a roll-to-roll, curved electrode geometry with promising scalability of the process. In better understanding the above applications, not only is research of the specific exploited mechanics necessary – such as precursor dissociation and deposition mechanisms, but also a fundamental understanding of the AP DBD itself [3]. The latter is the focus of the present study.

Past experimental work [9]–[11] has shown how an AP DBD is formed in both parallel and curved electrode configurations. Experiments were performed in mixtures of argon, oxygen and nitrogen. An initial Townsend-like discharge that transits into a glow like discharge was observed. The transition was found to be initiated by a single or multiple high intensity glow spots which are followed by a lateral expanding wave while the plasma extinguishes at the original location of the glow spot. Recently [12], the roll-to-roll geometry, the gas flow, the dielectric barrier layer and its transport were found to significantly influence the plasma expansion and formation towards steady state.

In these studies, typically low frequency (LF) excitation was used. Liu and coworkers [13], [14] demonstrated the benefits of dual frequency (DF) plasma excitation of an AP DBD operated in cost effective argon and oxygen gas mixtures by using a 200 kHz LF and 13.56 MHz radio frequency (RF) applied voltage for the first time. The DF discharge exhibited beneficial behavior of both LF and RF discharges, improving on single LF through better uniformity and a more continuous discharge at higher input power [13]. The LF component is responsible for excitation and ionization processes near the dielectric boundaries while the RF component slows down the gas ionization processes [14]. Combined, this allows to modify the electron energy distribution function (EEDF) through the separate RF and LF amplitudes.

The goal of this thesis is to support those novel experimental results [9]–[11], [13], [14] by modelling of similar AP DBDs with a focus on roll-to-roll reactors and the plasma formation therein.

## 1.1. Experimental setup

The setups used in the related experimental studies are of significance and will be described here briefly.

Figure 1.1 shows two varieties of roll-to-roll plasma reactors. One with a symmetric electrode setup and one with an asymmetric setup. The reactors are open to ambient air [8]. The symmetric one uses two metal rotating drum electrodes with a radius of 120 mm and a width exceeding the effective discharge width of 150 mm [11]. The asymmetric setup consists of a flat bottom electrode with a length of 100 mm. The top electrode is curved with a radius of 60 mm. The electrode widths are 45 mm [14]. Generally the electrodes are maintained at a specific temperatures, i.e. 30 °C [14]. Typical gas gaps were in the order of 0.5 to 1 mm. Polyethylene naphthalate (PEN) and polyethylene terephthalate (PET) are mostly used as the dielectric barrier with a thickness of 100 µm [11], [14], generally serving also as the thin film deposition substrate, transported at low speeds, i.e. 40 mm/min [14]. The low frequency plasma excitation frequency is approximately 200 kHz [11]. In dual frequency studies, a 13.56 MHz radio frequency component is added [14]. The applied voltage depends on the specific gas mixture but is typically a few kV [11].

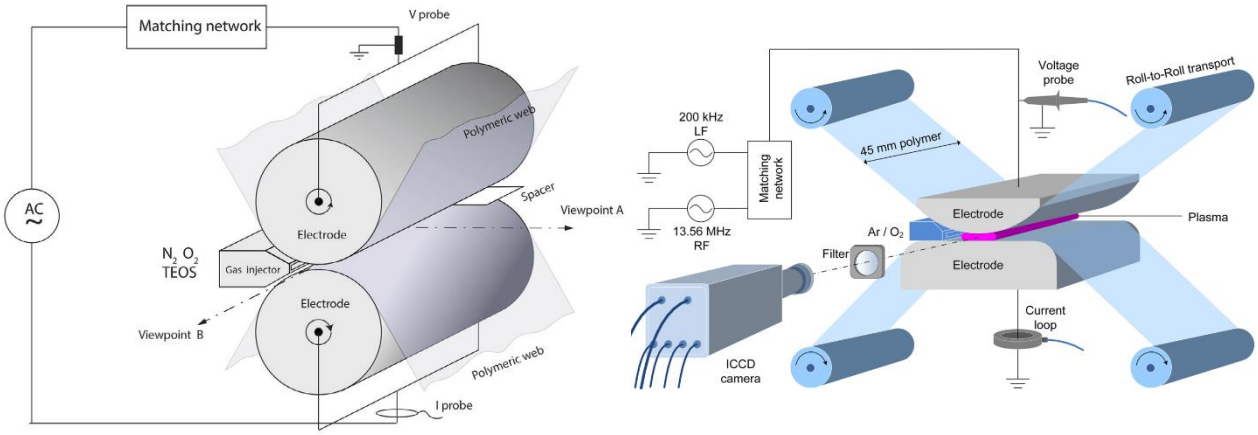


Figure 1.1. Schematics of the experimental roll-to-roll plasma reactors for both the symmetric electrode setup [11] (left) and the asymmetric electrode setup [14] (right).

## 1.2. Project goals

The underlying goal of this work is to support the experimental work through modelling. The modelling is carried out through PLASIMO's [15] drift-diffusion code [16]. The initial, required, goal is:

1. To obtain a stable and steady state plasma model with which it is possible to model a wide range of (AP DBD) discharges.

The goals that serves to complement the past experimental research are:

2. To gain insight into the plasma parameters under dual frequency excitation.

3. To understand the plasma dynamics in two dimensional roll-to-roll geometries.

This study focusses on discharges in argon. Argon is chosen mainly based on recent experiments where argon/oxygen gas mixture have been used, with argon the main component (often $\geq 80/20, \mathrm{Ar/O_2}$). Fundamental research to the various modes of AP DBDs is often conducted in other gases such as both helium [17]–[22] and nitrogen [21], [23], while such research is less reported for

the case of argon [24]–[26]. Still, Starostin and coworkers have shown that the more economical gas mixtures are relevant [8]–[14]. Modelling argon also serves as a basis for modelling admixtures with argon and also an eventually transition to oxygen or nitrogen based gas mixtures involving argon [8], [11].

## 1.3. Outline of this thesis

The thesis is divided into three parts, the preliminaries, the modelling results and the overall conclusions.

**Part 1: Preliminaries**

**Chapter 2** summarizes (the underlying equations of) the PLASIMO drift-diffusion code. This includes a description of the relevant boundary conditions and a brief description of the order in which the (semi-)implicit calculations are performed.

**Chapter 3** discusses the model input concerning the plasma argon chemistry as used throughout this study. This chapter also includes some reference material concerning comparisons in reaction rate coefficients and ionization paths.

**Chapter 4** presents the translation from the experimental plasma reactors to the (two-dimensional) grids that can be implemented in PLASIMO. It also contains a **section (4.5)** which describes PLASIMO's grid generation. This chapter introduces the bipolar coordinate system. This introduction is very descriptive. Generally, the considerations in this chapter are in depth. This chapter can be skipped without loss of continuity.

**Part 2: Results**

***Chapter 5, 6, 7 and 8*** *contribute to the first project goal as formulated in section 1.2 and to the understanding of the general discharge mechanisms and influence of model input parameters.* ***Chapter 9*** *is after the second goal and* ***chapter 10*** *after the third goal, both of which complement the past experimental research.*

*The chapters in* ***part 2*** *are related to each other and do refer to each other, still they can be read separately, on their own.*

**Chapter 5** reports on the (spatial) discharge structure and the plasma chemistry. Individual chemical processes are considered and a chemical model with a reduced amount of reactions is introduced to apply this scheme in two-dimensional modelling to save on computational time. Stepwise ionization and associative metastable-metastable ionization are considered as well as briefly dissociative recombination.

**Chapter 6** further considers the plasma chemistry, but is dedicated to the total metastable-metastable ionization and investigates its role in the formation of a positive column and the overall discharge and current characteristics.

**Chapter 7** summarizes the discharge structure similarly to chapter 5 but considers the discharge from a first breakdown towards steady state, instead of considering steady state only and reports on the observed breakdown mechanisms.

In **chapter 5, 6 and 7** secondary electron emission was used but the influence of the coefficients and the chosen value were not considered in particular.

**Chapter 8** contains a numerical study focused on the various secondary electron emission processes. Electron emission by each argon minority species is considered in isolation and the influence of combined (atomic and molecular) ion-electron emission coefficients is investigated.

**Chapter 9** presents results of dual frequency plasma excitation. As output of the present study a paper has been submitted for publication[1]. In this chapter some excerpts from this paper – relevant to the participation – are presented (verbatim), it is shown that modelled results exhibited excellent agreement with experimental results (also conducted in argon).

**Chapter 10** contains the two-dimensional modelling results were the discharge is compared to one-dimensional modelling results. The formation and expansion is considered within single half cycles and from a first breakdown towards steady state.

**Part 3: Conclusions**

**Chapter 11** gives the overall conclusions, preceded by a brief discussion and followed by other miscellaneous recommendations.

[1] Liu, Y., van 't Veer, K., Peeters, F., Mihailova, D., van Dijk, J., Starostine, S., Van de Sanden, R., De Vries, H. "Numerical simulation of atmospheric-pressure 200 kHz / 13.56 MHz dual-frequency dielectric barrier discharges" Accepted for publication in Plasma Sources Science and Technology

# Part 1:
# Preliminaries

# 2. The drift-diffusion model

Throughout this study the drift-diffusion model of PLASIMO is used. PLASIMO itself provides a user friendly solution to plasma modelling offering various modules and solvers for a wide range of applications [15]. The first version of the code was developed by Hagelaar [27]. Integration into PLASIMO was achieved later by van Dijk and Brok [28]. Since then the code was significantly extended by Mihailova [16] and used in other studies (such as [29]). Currently the code is actively supported by Mihailova et al. through the Eindhoven University of Technology spin off company Plasma Matters B.V. and by the research group EPG (Elementary Processes in Gas Discharges) of the university itself [30].

Here the equations governing the model will be described, starting from the Boltzmann equation [31]

$$\frac{\partial f_p}{\partial t} + \mathbf{v} \cdot \nabla_{\mathbf{x}} f_p + \mathbf{a} \cdot \nabla_{\mathbf{v}} f_p = \left.\frac{\partial f_p}{\partial t}\right|_{cr} \tag{2.1}$$

which describes the distribution $f_p(\mathbf{x}, \mathbf{v}, t)$ of particles $p$ with velocity $\mathbf{v}$ and position $\mathbf{x}$ and its evolution in time $t$, with $\mathbf{a}$ the particle acceleration and $\nabla_{\mathbf{x}}$ and $\nabla_{\mathbf{v}}$ the gradient with derivatives with respect to the position and velocity components respectively. The $cr$ term accounts for movement of particles and appearing and disappearing particles in the phase space $(\mathbf{x}, \mathbf{v})$ of $f$ due to various collisional or radiative processes. Calculating the first three moments of the Boltzmann equation by proper multiplication and integration over the velocity space yields conservation equations.

The 0th moment: multiplication by the mass $m_p$ and performing integration over velocity space yields the particle balance

$$\frac{\partial n_p(\mathbf{x}, t)}{\partial t} + \nabla \cdot \mathbf{\Gamma}_p(\mathbf{x}, t) = S_p(\mathbf{x}, t) \tag{2.2}$$

describing the evolution of the species density $n_p$, with $\mathbf{\Gamma}_p = n_p \mathbf{u}_p$ the flux density, $\mathbf{u}_p \equiv \langle \mathbf{v} \rangle_p$ the average particle velocity and $S_p$ the source term accounting for both gains and losses of particles of type $p$ [16].

The 1st moment: multiplication by the momentum $m_p \mathbf{v}$ and integrating yields the momentum balance. This balance equation is used after neglecting viscosity and inertia and using scalar treatment of the pressure, denoted $P_p$, by assuming that it is isotropic [31]. In addition, assuming variation of the average particle velocity in time to take place on timescales much larger than the average collision time [16] yields the simplified, time-independent, momentum balance

$$-\nabla P_p + n_p m_p \mathbf{a} + \mathbf{R}_p = 0 \tag{2.3}$$

$$-\nabla\left(n_p\left(k_B T_p\right)\right) + q_p n_p \mathbf{E} + \mathbf{R}_p = 0 \tag{2.4}$$

where the ideal gas law $P_p = n_p k_B T_p$ is used and the force $m_p \mathbf{a}$ on the particles is taken to be due to an electric field $\mathbf{E}$ only with $q_p$ the charge of the particle and $\mathbf{R}_p$ is the momentum transfer rate due to collisions between particle $p$ and $q$ given by [16]

$$\mathbf{R}_p = -n_p \sum_q m_{pq} \nu_{pq} \left(\mathbf{u}_p - \mathbf{u}_q\right) \tag{2.5}$$

where $m_{pq}$is the reduced mass

$$m_{pq} = \frac{m_p m_q}{m_p + m_q} \tag{2.6}$$

$\nu_{pq}$ is the momentum transfer frequency between particles $p$ and $q$. In principle the summation is over all particles, however noting the dominance of the background gas $p \equiv 0$ and assuming it stationary ($\mathbf{u}_0 \equiv 0$), approximates and reduces the summation such that [16]

$$\mathbf{R}_p = -n_p m_{p0} \nu_{p0} \mathbf{u}_p \tag{2.7}$$

Finally, under the assumption of uniform temperature [16] equation 2.7 and 2.4 combined give the drift-diffusion equation for the particle flux density $\mathbf{\Gamma}_p$

$$\mathbf{\Gamma}_p = \mu_p \mathbf{E} n_p - D_p \nabla n_p \tag{2.8}$$

$$\mu_p = \frac{q_p}{m_p \nu_{p0}} \tag{2.9}$$

$$D_p = \frac{\left(k_B T_p\right)}{m_p \nu_{p0}} \tag{2.10}$$

where $\mu_p$ and $D_p$, the mobility and diffusion coefficient respectively, are defined. The expressions provided here are valid only for near-Maxwellian energy distribution functions [16], in which case the transport coefficients $\mu_p$ and $D_p$ are related to each other by the Einstein relation

$$\frac{D_p}{\mu_p} = \frac{\left(k_B T_p\right)}{q_p} \tag{2.11}$$

This relation can be used to calculate the diffusion coefficient for charged particles from the mobility. For electrons $p = \mathrm{e}$ the effective temperature is used:

$$k_B T_\mathrm{e} = \frac{2}{3}\varepsilon \tag{2.12}$$

where $\varepsilon$ is the mean electron energy. The ion ($p = i$) temperature is calculated using a more rigorous effective temperature [16]:

$$k_B T_i = k_B T_0 + \frac{m_i + m_0}{5m_i + 3m_0} m_0 (\mu_i E)^2 \tag{2.13}$$

By a *local field approximation*, ion mobility's are taken as functions of the reduced electric field $E/N$ [16] – in practice look up tables from literature [32] – with $N$ the background gas density. If not available, a collision integral method [33] is used in this study. The electron mobility is calculated by solving the EEDF (electron energy distribution function) from the Boltzmann equation (using BOLSIG+ [34]) at various reduced fields to which a mean electron energy $\varepsilon$ is assigned, calculated from the EEDF itself, such that $\mu_\mathrm{e}$ is given as a function of $\varepsilon$. For remaining particles, i.e. metastables, the diffusion coefficient is found in literature or also calculated using a collision integral method.

The 2nd moment: multiplication by the kinetic energy $m_p v^2/2$ and integrating over velocity space yields the energy balance

$$\frac{\partial n_p \varepsilon_p}{\partial t} + \nabla \cdot n_p \varepsilon_p \mathbf{u}_p + \nabla \cdot P_\mathrm{e} \mathbf{u}_\varepsilon + \nabla \cdot \mathbf{q}_p = S_{\varepsilon_p} \tag{2.14}$$

where the assumption of isotropic pressure [31] was immediately substituted [16], $\mathbf{q}_p$ is the heat flux density and $S_{\varepsilon_p}$ the energy source accounting for both gain and loss. The energy balance is solved for the electrons $p = \mathrm{e}$ only, defining the mean electron energy ($\varepsilon_\mathrm{e} \equiv \varepsilon$) density $n_\varepsilon \equiv n_\mathrm{e}\varepsilon$. By using the effective temperature (equation 2.12), the ideal gas law – to express $P_\mathrm{e}$ in $n_\varepsilon$ – and assuming that the heat flux density is proportional to the energy gradient [16],

$$\mathbf{q}_\mathrm{e} = -\frac{5}{3} n_\mathrm{e} D_\mathrm{e} \nabla \varepsilon \tag{2.15}$$

in addition to using the particle flux (equation 2.8). Then, by collecting all divergence terms of equation 2.11 followed with appropriate substitution, the mean electron energy flux density $\mathbf{\Gamma}_\varepsilon$ can be defined as

$$\mathbf{\Gamma}_\varepsilon = \frac{5}{3} \mu_\mathrm{e} \mathbf{E} n_\varepsilon - \frac{5}{3} D_\mathrm{e} \nabla n_\varepsilon \tag{2.16}$$

The result is that the electron energy balance can be expressed in the form of a continuity equation.

$$\frac{\partial n_\varepsilon}{\partial t} + \nabla \cdot \mathbf{\Gamma}_\varepsilon = S_\varepsilon \tag{2.17}$$

Equation 2.2 (with 2.8) and 2.17 (with 2.16) are the balance equations of interest. The source terms $S$ are described by the included plasma chemistry. For the particle balance equation the source term is given by

$$S_p = \sum_r c_{r,p} R_r \tag{2.18}$$

where $c_{r,p}$ is the stoichiometric number indicating the number of particles $p$ created in reaction $r$ and $R_r$ is the rate. It is positive, negative or zero. The mean electron energy source term is given by

$$S_\varepsilon = \Gamma_\mathrm{e} \cdot \mathbf{E} - \sum_r \varepsilon_{th,r} R_r - L_\varepsilon \tag{2.19}$$

where the first term is an energy gain due to acceleration by the electric field, the second and last term $L_\varepsilon$, typically energy losses, are due to inelastic and elastic reactions respectively. The threshold energy, i.e. the energy lost or gained in reaction $r$ is denoted by $\varepsilon_{th,r}$. Here the summation over $r$ includes reactions with electrons only. The rate $R_r$ is given by

$$R_r = k_r \prod_q n_q \tag{2.20}$$

where $k_r$ is the rate coefficient. The product is over 1, 2 or 3 particle densities, depending on the amount of reacting bodies in reaction $r$. BOLSIG+ [34] is also used to calculate the elastic loss term in

the mean electron energy source term (equation 2.19) and for the rate coefficient of all two-body electron impact reactions. Other rate coefficients are taken from literature.

The main continuity equations (2.2 and2.17) are coupled to the Poisson equation to solve for the electric field and potential.

$$\nabla \cdot (\epsilon \mathbf{E}) = -\nabla \cdot (\epsilon \nabla V) = \rho = \sum_p q_p n_p \tag{2.21}$$

where $\epsilon$ is the dielectric constant, $V$ the electric potential and $\rho$ the space charge density, which does include and account for surface charges and discontinuities [16].

The boundary conditions of interest for the Poisson equations are given for the potential $V$ as Dirichlet or Homogenous Neumann for electrode and open boundaries respectively. For a dielectric-plasma boundary the following boundary condition is used [27]:

$$\epsilon_{wall} \mathbf{E}_{wall} \cdot \hat{\mathbf{n}} - \epsilon_0 \mathbf{E}_{gas} \cdot \hat{\mathbf{n}} = \sigma \tag{2.22}$$

$$\sigma = \int \mathbf{j} \cdot \hat{\mathbf{n}} \, dt \tag{2.23}$$

$$\mathbf{j} = \sum_p q_p \mathbf{\Gamma}_p \tag{2.24}$$

where $\epsilon_{wall}$ is the dielectric constant of the wall, i.e. the dielectric material, $\mathbf{E}_{wall}$ the electric field in it, $\epsilon_0$ permittivity of vacuum (the gas), $\mathbf{E}_{gas}$ the electric field in the discharge gas, $\sigma$ the surface charge density and **j** the current density. Note that the surface charge is assumed to be stationary after being deposited on the wall [16].

The boundary conditions for the particle balance equations (2.2) are Homogenous Neumann for open boundaries. For material boundaries, the general boundary condition is given by [27]:

$$\mathbf{\Gamma}_p \cdot \hat{\mathbf{n}} = n_p \left( \alpha_p \mu_p \mathbf{E} \cdot \hat{\mathbf{n}} + \frac{1}{4} v_{th,p} \right) \tag{2.25}$$

$$\alpha_p = \begin{cases} 1, & \mu_p \mathbf{E} \cdot \hat{\mathbf{n}} > 0 \\ 0, & \mu_p \mathbf{E} \cdot \hat{\mathbf{n}} \leq 0 \end{cases} \tag{2.26}$$

$$v_{th,p} = \sqrt{\frac{8 k_B T_p}{\pi m_p}} \tag{2.27}$$

where $v_{th,p}$ is here defined as the thermal velocity. Note that reflection and its coefficient were not expressed in equation 2.25 [27] as they are not used in this study. Equation 2.25 can be seen as a general boundary flux determined by a combination of a mobility limited and kinetically limited flux term [35], first and second term respectively. The second term can be derived by calculating the average flux in one direction, i.e. $n_p \langle v_z \rangle_{\mathbf{v}}$ from the Maxwellian velocity distribution yielding $\mathbf{\Gamma}_p \cdot \hat{\mathbf{n}} = n_p v_{th,p}/4$ [31].

For the electron particle balance this boundary condition is modified with one additional term accounting for secondary electron emission [27].

$$\boldsymbol{\Gamma}_{\mathrm{e}} \cdot \hat{\mathbf{n}} = n_{\mathrm{e}} \left( \alpha_{\mathrm{e}} \mu_{\mathrm{e}} \mathbf{E} \cdot \hat{\mathbf{n}} + \frac{1}{4} v_{th,\mathrm{e}} \right) - \sum_{p} \gamma_p \, \boldsymbol{\Gamma}_p \cdot \hat{\mathbf{n}} \tag{2.28}$$

The boundary conditions on continuity equation 2.14, describing the mean electron energy density, is consistent with the boundary conditions on the electron density, thus given by [27]:

$$\boldsymbol{\Gamma}_{\varepsilon} \cdot \hat{\mathbf{n}} = n_{\varepsilon} \left( \alpha_{\mathrm{e}} \frac{5}{3} \mu_{\mathrm{e}} \mathbf{E} \cdot \hat{\mathbf{n}} + \frac{1}{3} v_{th,\mathrm{e}} \right) - \sum_{p} \gamma_p \, \varepsilon_{\gamma,p} \boldsymbol{\Gamma}_p \cdot \hat{\mathbf{n}} \tag{2.29}$$

where $\varepsilon_{\gamma,p}$ is the mean initial energy of emitted electrons due to particles of type $p$. The second term can be derived by calculating the average energy flux $n_{\mathrm{e}} \langle m v^2 v_z / 2 \rangle_{\mathbf{v}}$ from the Maxwellian velocity distribution yielding $\boldsymbol{\Gamma}_{\varepsilon} \cdot \hat{\mathbf{n}} = 2 k_B T \boldsymbol{\Gamma}_{\mathrm{e}} \cdot \hat{\mathbf{n}}$ [31] and combining with equation 2.12.

In PLASIMO the calculations are performed (semi-)implicitly [16], in the following order:

1. Initialization of time and densities including mean electron energy density.
2. Determination of the time step.
3. Calculation of the rate coefficients and transport coefficients.
   (Principally involving equation 2.9 and 2.10.)
4. Update electrode potentials.
5. Calculate the electric potential and electric field.
   (Principally involving equation 2.21-2.24.)
6. Calculate the particle densities.
   (Principally involving equation 2.2, 2.8, 2.25 or 2.28.)
7. Calculate mean electron energy source term and its density.
   (Principally involving equation 2.17, 2.19 and 2.29.)
8. Check end of simulation, repeat from step 2.

# 3. The argon chemistry input

In this study an argon atmospheric pressure dielectric barrier discharge is modelled. To that end an argon chemistry model is constructed from existing literature. As a start the model described by Sobota et al. [24] is considered because in that study a focus lay on a first breakdown using low initial conditions for the species densities. There, a set of 10 reactions was reported of which 6 were used in the presented results. This reduction was made based on the time scales of interest, removing all recombination reactions – including, amongst others, molecular to atomic ion conversion, radiative decay and three body recombination. It was noted to not make a difference in the presented results. However, also noted was that the breakdown process can depend on a wide range of variables. As such – and because interest lies also beyond a first breakdown, i.e. a periodic steady state discharge – the argon chemistry used in this present study is based on the whole set as reported by Sobota [24] with alterations and additions mainly after the studies of Sun et al. [36] and Kolev et al. [37]. The alterations and additions are for example the inclusion of other three body reactions and different treatment of photons. Note that [36] is a reduction of [37] where two effective reactions were introduced to replace $Ar_2^*$ and Ar(4p). Those reactions are not used in present study as they were found to not produce a stable plasma model (over a wide range of conditions). The authors do indeed note that those approximated rate coefficients do not necesairly work well under different discharge conditions than theirs.

The various species under consideration are introduced first in section 3.2 after which the included reactions are presented and discussed in section 3.2.

## 3.1. The species list

In total four species are used in this description of an argon discharge. The electron e, an effective excited state $Ar^*$ that represents all four 4s states (two metastable and two resonant states), the atomic ion $Ar^+$ and the molecular ion $Ar_2^+$. For the argon (Ar) background gas, a uniform gas temperature is assumed. Together with the assumption that both the excitation and ionization degree [31] is very low the background gas density is treated as a constant: $n \approx p/k_B T_g$.

Table 3.1 lists the species and their transport coefficients. The ion mobilities were all available as look up tables as a function of the reduced electric field [32]. The diffusion coefficients of the charged particles are calculated using the Einstein relation (see chapter 2 and equation 2.11). The diffusion coefficient for $Ar^*$ is calculated from the collision integrals, using the method reported by Janssen [33], resulting in a value that is independent of the reduced electric field but dependent on the temperature through, among others, the collision integral itself. The reported value is calculated at 450 K.

Table 3.1. Species involved in the argon chemistry, the (source of the) transport coefficients and the initial densities.

| P# | Species | $\varepsilon_{th}$ (eV) | $\mu_p N$ | $D_p N$ ($m^{-1}s^{-1}$) | $n_p(0)$ ($m^{-3}$) [24] [1] |
|---|---|---|---|---|---|
| 1 | e | 0 | $\mu_e N(\varepsilon)$ [38] | Einstein | $10^9$ |
| 2 | Ar | | constant background gas | | |
| 3 | $Ar^*$ | 11.55 | no charge | $6.45163 \cdot 10^{20}$ [33] | $10^{-4}$ |
| 4 | $Ar^+$ | 15.759 | $\mu_{Ar^+} N(E/N)$ [32] | Einstein | $10^9$ |
| 5 | $Ar_2^+$ | 14.5 [39] | $\mu_{Ar_2^+} N(E/N)$ [32] | Einstein | $10^{-4}$ |

[1] Here the actuall minimal density value in the drift-diffusion model is reported ($10^{-4}$ $m^{-3}$). It can be considered an arbitrarily value, essentially representing zero.

## 3.2. The reactions

Table 3.2 lists all the reactions used for the argon chemistry.

Table 3.2. The reactions governing the argon plasma chemistry in this study, their rate coefficients and its main source.

| R# | Abbr. | Reaction | Rate coefficient |
|---|---|---|---|
| 1 | | $e + Ar \rightarrow Ar + e$ | $k_1(\varepsilon)$ [38] |
| 2 | EXC | $e + Ar \rightarrow Ar^* + e$ | $k_{EXC}(\varepsilon)$ [38] |
| 3 | DEXC | $e + Ar^* \rightarrow Ar + e$ | $k_{DEXC}(\varepsilon)$ [38] |
| 4 | SI | $e + Ar^* \rightarrow Ar^+ + e + e$ | $k_{SI}(\varepsilon)$ [38] |
| 5 | DI | $e + Ar \rightarrow Ar^+ + e + e$ | $k_{DI}(\varepsilon)$ [38] |
| 6 | MMI | $Ar^* + Ar^* \rightarrow Ar^+ + e + Ar$ | $(1/(1+\beta)) \cdot 1.2 \cdot 10^{-15}(300/T[\mathrm{K}]))^{1/2} \mathrm{m^3 s^{-1}}$ [40] [1] |
| 7 | MMAI | $Ar^* + Ar^* \rightarrow Ar_2^+ + e$ | $(\beta/(1+\beta)) \cdot 1.2 \cdot 10^{-15}(300/T[\mathrm{K}])^{1/2} \mathrm{m^3 s^{-1}}$ [40] [1] |
| 8 | AMC | $Ar^+ + Ar + Ar \rightarrow Ar_2^+ + Ar$ | $2.5 \cdot 10^{-43}(300/T[\mathrm{K}])^{3/2}\ \mathrm{m^6 s^{-1}}$ [41] |
| 9 | MAC | $Ar_2^+ + Ar \rightarrow Ar^+ + Ar + Ar$ | $5.22 \cdot 10^{-16} \mathrm{T^{-1}} \exp(-1.304/\mathrm{T[eV]})\ \mathrm{m^3 s^{-1}}$ [36] |
| 10 | DR | $e + Ar_2^+ \rightarrow Ar^* + Ar$ | $7 \cdot 10^{-13} \cdot (300/T_e[\mathrm{K}])^{1/2}\ \mathrm{m^3 s^{-1}}$ [41] |
| 11 | TBR | $e + Ar^+ + e \rightarrow Ar + e$ | $8.75 \cdot 10^{-39} \mathrm{T_e[eV]^{-9/2}}\ \mathrm{m^6 s^{-1}}$ [42] |
| 12 | TBR | $e + Ar^+ + Ar \rightarrow Ar + Ar$ | $1.5 \cdot 10^{-40}(300/T[\mathrm{K}])^{2.5}\ \mathrm{m^6 s^{-1}}$ [36] |
| 13 | RAD | $Ar^* \rightarrow Ar + h\nu$ | $(1.15/\pi)(\lambda_{4s}/6H)^{1/2} \cdot 3.145 \cdot 10^8\ \mathrm{s^{-1}}$ [39] [2] |

[1] $\beta$ is the adopted branching factor defined as 0.9 by Pavlík et al. [43]. See text, equation 3.1 and 3.2

[2] $\lambda_{4s}$ is the effective wavelength attributed to the lumped Ar(4s) state after Gregorio et al. [39]. See text, equation 3.5.

Reaction R1 is the elastic collision between electrons and the background gas. This reaction occurs as the last term in the mean electron energy source term (equation 2.19). R2 through R5 are the basic two body electron involving reactions – excitation, de-excitation, ionization from metastable (stepwise ionization) and direct ionization respectively. The rate coefficients of all those reactions are determined using BOLSIG+ [34], which also produces the electron mobility.

The cross sectional data comes from the Morgan database through LXcat [38]. The BOLSIG+ input does also include the total excitation cross section, such that the EEDF and elastic power loss of the electrons – calculated from the EEDF – also take into account loss due to excitation collisions to higher energy states that are assumed to immediately decay back to the ground state. Effectively describing an additional energy transfer path. The calculated rate coefficient for this cross section data is not used. Electron-electron collisions are considered too, with a given ionization degree of $1 \cdot 10^{-7}$. The influence of both those inclusions on the calculated EEDF is shown in Figure 3.1. For high reduced fields, the ionization degree was still too low to make a significant difference. The used BOLSIG+ input throughout this study does include the electron-electron collisions, for completeness, but will not be considered especially.

R6 and R7 are metastable-metastable ionization processes, with the later associative. Sobota et al. [24] only reports R6. Rate coefficients are reported without temperature dependencies throughout. The used value is taken from Balcon et al. [41] where a temperature dependency is included, also using one metastable-metastable ionization reaction. Sun et al. [36], [37] does use both reactions but does not specifically relate them to each other concerning the rate coefficient, their source for the metastable-metastable ionization rate coefficient is Gregorio et al. [39]. Here the associative process is not described. The source for the associative process used by Sun et al. is Bultel et al. [44] who describe the formation processes of the dimer ions, including the associative ionization with a rate coefficient taken from Bogearts and Gijbels [40] with an added temperature dependence of the same

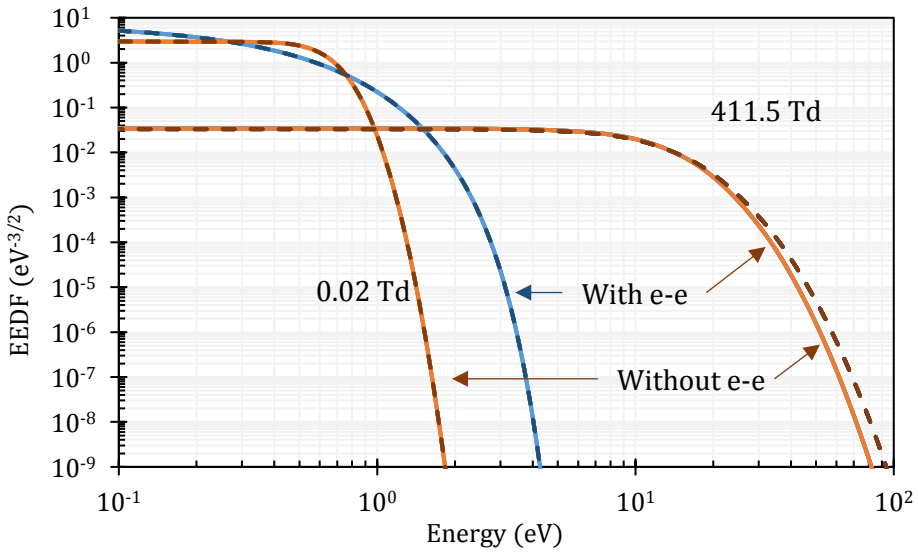


Figure 3.1. Comparison of the electron energy distribution function (EEDF) calculated using BOLSIG+ [34], including reactions R1-R5, at a low (0.02 Td, $\varepsilon = 0.4$ eV) and high (411.5 Td, $\varepsilon = 9.5$ eV) reduced electric field with and without taking into account electron-electron (e-e) collisions, blue and orange respectively. Solid lines do not include the total excitation reaction (cross section data) in the BOLSIG+ input data. The dashed dark lines do. The orange dashed dark line represents the data used throughout this study.

form as was found in [41]. Bogearts and Gijbels did indicate the difficulty of finding rate coefficients for those two reactions. It is their formulation that is principally used in the present study to which temperature dependency is added as found in [41], [44]. Bogearts and Gijbels branched the two reactions from a total rate coefficient consistent with [24], [41]. They took the actual total value ($1.2 \cdot 10^{-15}$ $\mathrm{m^3 s^{-1}}$) from a review, on studies on the release of fast electrons from reactions involving excited atoms, by Kolokolov and Blagoev [45]. The branching factor ($\beta = 0.9$) is given by Pavlík et al. [43] who also investigated the influence of the branching factor in a numerical model. Metastable atom and electron densities were found to not be influenced significantly by this branching factor. In present study a similar investigation is made in section 5.2.2. Furthermore Bogearts and Gijbels noted that their eventual rate coefficient for the associative ionization was similar to the value adopted by Neeser et al. [46]. The rate coefficients used, in this study, are:

$$k_{\mathrm{MMI}} = \left(\frac{1}{1+\beta}\right) \cdot 1.2 \cdot 10^{-15} \cdot \left(\frac{300}{T}\right)^{\frac{1}{2}} \ \mathrm{m^3 s^{-1}} \tag{3.1}$$

$$k_{\mathrm{MMAI}} = \left(\frac{\beta}{1+\beta}\right) \cdot 1.2 \cdot 10^{-15} \cdot \left(\frac{300}{T}\right)^{\frac{1}{2}} \ \mathrm{m^3 s^{-1}} \tag{3.2}$$

where the subscripts MMI and MMAI denote the regular and associative metastable-metastable ionization respectively. The rate coefficient $k_{\mathrm{MMAI}}$ is consistent with Sun et al. [36] besides a reported factor 1/2 (which is explicitly stated as such) of which the origin is unclear. The total rate at which the metastable-metastable collision occurs is consistent with Sobota et al. [24]. Compared to Sun et al. [36], the evaluated rate coefficient $k_{\mathrm{MMI}}$ is also similar. Metastable-metastable in its entirety is considered in chapter 6.

R8 and R9 are the atomic to molecular ion conversion and molecular to atomic ion conversion respectively. R10 through R12 include the recombination processes; dissociative recombination and three body recombination both with an electron and argon ground state atom as the third body, respectively.

R13 accounts for the radiative decay, here treated with an effective escape factor $g_{eff}$ as defined by Gregorio et al. [39] accounting for collisional broadening derived from Holstein's [47], [48] formulation and derivation of effective escape factors for an infinite slab ([48], equation 6.5). The rate coefficient $\nu_{\mathrm{RAD}}$ used is:

$$\nu_{\mathrm{RAD}} = g_{eff}(H) \cdot 3.145 \cdot 10^{8}\ \mathrm{s}^{-1} \tag{3.3}$$

$$g_{eff}(H) = \frac{1.15}{\pi}\left(\frac{\lambda_{4s}}{6H}\right)^{1/2} \tag{3.4}$$

$$\begin{aligned} \lambda_{4s} &= \frac{\lambda_{^3P_1} + \lambda_{^1P_1}}{2} \\ &= \frac{106.7 + 104.8}{2} = 105.75\ \mathrm{nm} \end{aligned} \tag{3.5}$$

where $H$ is the characteristic dimension of the plasma reactor [37], here taken as the gas gap[1]. Typical values of interest are of order $10^5\ \mathrm{s}^{-1}$ for $\nu_{\mathrm{RAD}}$. This is in agreement with other literature using approximated values for their specific situation [41] and direct use thereof in other studies [25].

### 3.2.1. Comparison of the rate coefficients

Figure 3.2 compares the rate coefficients $k_r$ to each other. Figure 3.2a compares the BOLSIG+ [34] calculated rate coefficients and $k_{\mathrm{DR}}$. Figure 3.2b compares all the reactions in which one species and the background gas only collide with each other by calculating an effective (reaction) frequency through multiplication with the constant density of Ar. Figure 3.2c compares $Ar^*$ related reactions as a function of the metastable density together with other effectively constant rate coefficients in a similar fashion. The three body recombination reactions are not displayed. Figure 3.2b already indicates that molecular to atomic ion conversion is relatively inefficient. In chapter 5 an overall reduction of the reactions included in the drift-diffusion model through the eventual rate contributions is considered.

[1] For models with non-uniform gap size, the local gap size was used.

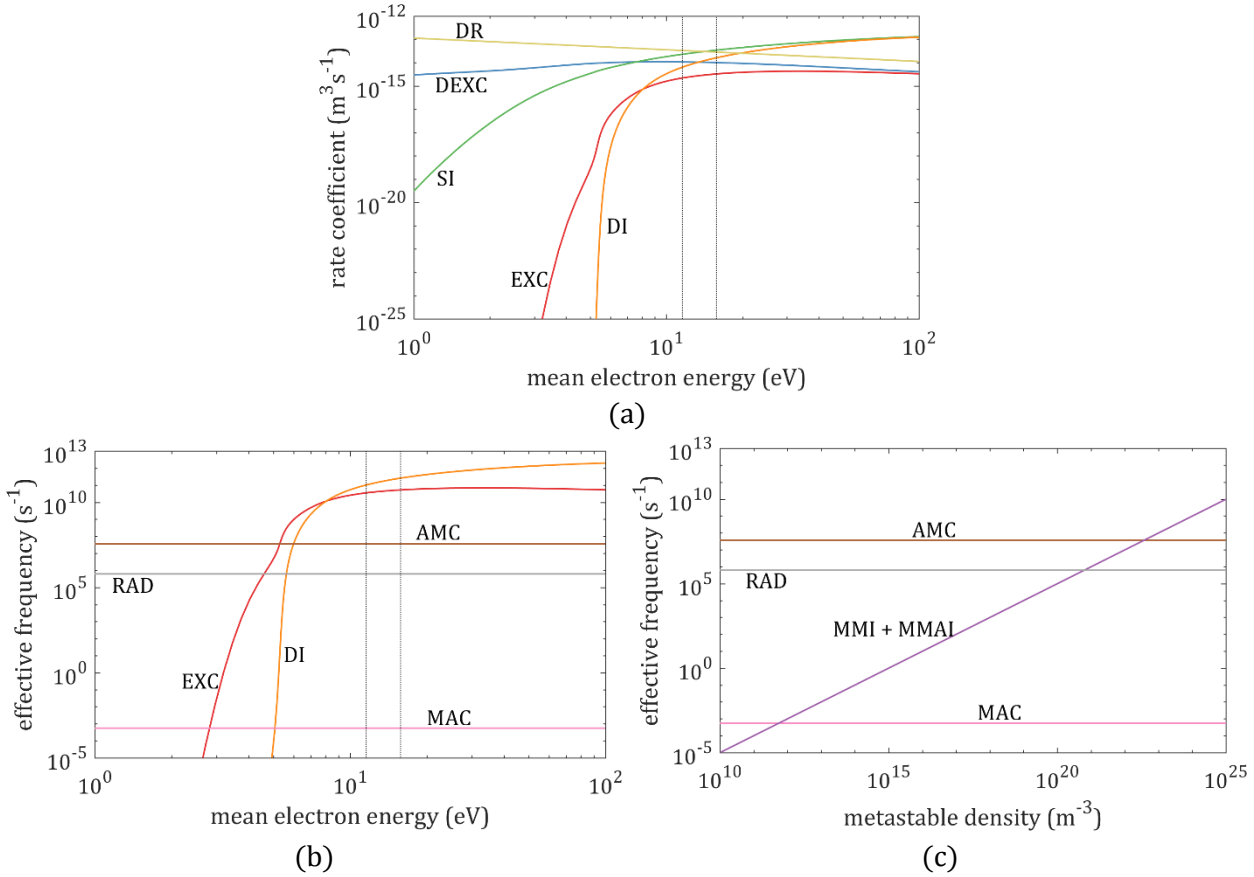


Figure 3.2. Comparison of various rate coefficients. Comparison of (two-body) electron impact processes (a). Comparison of collisions solely with the background gas through an effective frequency (b), including radiative decay. Comparison of metastable related reactions through an effective frequency as a function of the metastable density (c), including other constant reactions. The mean electron energy axes have indicated the excitation and ionization threshold energy, 11.55 and 15.759 eV [38] respectively. The abbreviations are listed in table 3.2. The reported value for radiative decay assumes $H = 0.6$ mm.

### 3.2.2. Ionization pathways summary

The argon chemistry describes both the atomic ions $Ar^+$ and the molecular ions $Ar_2^+$.

Starting from the ground state, the atomic ions can be formed by direct ionization

$$e + Ar \xrightarrow{1} e + e + Ar^+ \tag{3.6}$$

or by excitation and subsequent stepwise ionization

$$\begin{aligned} e + Ar &\xrightarrow{1} e + Ar^* \\ e + Ar^* &\xrightarrow{2} e + e + Ar^+ \end{aligned} \tag{3.7}$$

or alternatively through metastable-metastable ionization

$$\begin{aligned} e + Ar &\xrightarrow{1} e + Ar^* \\ Ar^* + Ar^* &\xrightarrow{2} e + Ar + Ar^+ \end{aligned} \tag{3.8}$$

finally molecular to atom ion conversion is also an option

$$Ar_2^+ + Ar \xrightarrow[4]{3} Ar^+ + Ar + Ar \tag{3.9}$$

Path 3.9 is preceded by either 3.10 or 3.11.

The molecular ions can also be formed through metastable-metastable ionization

$$\begin{aligned} e + Ar &\xrightarrow{1} e + Ar^* \\ Ar^* + Ar^* &\xrightarrow{2} Ar_2^+ + e \end{aligned} \tag{3.10}$$

and atomic to molecular ion conversion

$$\begin{aligned} e + Ar &\xrightarrow{1} e + Ar^* \\ e + Ar^* &\xrightarrow{2} e + e + Ar^+ \\ e + Ar &\xrightarrow{1} e + e + Ar^+ \\ Ar^+ + Ar + Ar &\xrightarrow[2]{3} Ar_2^+ + Ar \end{aligned} \tag{3.11}$$

# 4. Geometry input

Here the translation from the geometrics of the experimental setup to the PLASIMO input will be given. PLASIMO uses orthogonal curvilinear coordinate systems, including support for user defined systems. In PLASIMO the current implementation is through the user interface using a cell matrix to define the inner geometry. The used cell matrixes will also be given (section 4.4).

*The specifics of the plasma reactor geometry and the implementation is essential in the construction of the model. This introduction of the bipolar coordinate system is very descriptive. Generally, the considerations in this chapter are in depth. This chapter can be skipped without loss of continuity.*

The experimental plasma reactor [11] consists of two electrodes covered by a dielectric opposite of each other with the gas gap in between. The electrodes are generally curved, but the electrode shape is not necessarily identical. The dielectric barrier discharge is ignited vertically in the experiments.

A basic, symmetric, two dimensional model will be described in Cartesian coordinates first (section 4.1). This cannot be implemented exactly. The geometry is then described using the bipolar coordinate system [49] (section 4.2) which does allow for implementation in PLASIMO (section 4.3). At this point the symmetric case is modified to represent asymmetric electrodes (section 4.3.1). The actual input of PLASIMO in the form of *CellMatrices* for a one and two-dimensional case will be given (section 4.4) after which the grid generation of PLASIMO is explained (section 4.5).

## 4.1. Cartesian description of the two-dimensional model

First a symmetric case will be considered with electrodes of same radius opposing each other. Here described in Cartesian coordinates $(x, y)$.

The electrodes are assumed to have radius $R_E$, the full gaseous gap is $d_g$ and $d_\epsilon$ is a single dielectric thickness. In the middle of the gap, $y = 0$ is chosen. The smallest gas gap is chosen at $x = 0$. The center of the electrodes should then lie at $(0, \pm b)$ given by

$$b = \frac{d_g}{2} + d_\epsilon + R_E \tag{4.1.1}$$

The electrodes themselves can be described by the circles

$$x^2 + (y \mp b)^2 = R_E^2 \tag{4.1.2}$$

The negative sign indicates the top electrode. The most straightforward assumption for the dielectric layer is that the electrodes are covered uniformly. The dielectric would then describe the same circle with a slightly different radius.

$$x^2 + (y \mp b)^2 = r_\epsilon^2 \tag{4.1.3}$$

$$r_\epsilon = R_E + d_\epsilon \tag{4.1.4}$$

The model boundary on the east and west side will be set to a fixed distance such that those boundaries lie on $(\pm l, 0)$. Furthermore those boundaries are chosen to be orthogonal to the electrode boundaries. This can also be described with circles. It is assumed that those circles need an offset $a$ in the $x$ direction to describe all $l$. Such that the left and right boundary of the model are described by

$$(x \pm a)^2 + y^2 = r^2 \tag{4.1.5}$$

$$r + a \equiv l \tag{4.1.6}$$

The positive sign indicates the left boundary circle. Circles written in the form of equation 4.1.2 and 4.1.5 can be rewritten to the expanded form.

$$x^2 + y^2 + (2g)x + (2f)y + c = 0 \tag{4.1.7}$$

where $(2g)$, $(2f)$ and $c$ are constants. Two circles are orthogonal to each other if the orthogonality condition [50] is met.

$$2g_1g_2 + 2f_1f_2 = c_1 + c_2 \tag{4.1.8}$$

Expanding equation 4.1.2 and 4.1.5 into 4.1.7 and applying 4.1.8 gives

$$\alpha^2 = r^2 - a^2 \tag{4.1.9}$$

$$\alpha^2 \equiv b^2 - R_E^2 \tag{4.1.10}$$

From 4.1.9 and 4.1.6, $r$ and $a$ can be solved. The left and right boundary are then given by

$$\left(x \pm \frac{l^2 - \alpha^2}{2l}\right)^2 + y^2 = \left(\frac{l^2 + \alpha^2}{2l}\right)^2 \tag{4.1.11}$$

The positive sign indicates the left boundary circle. Figure 4.1 shows the above for an arbitrary case.

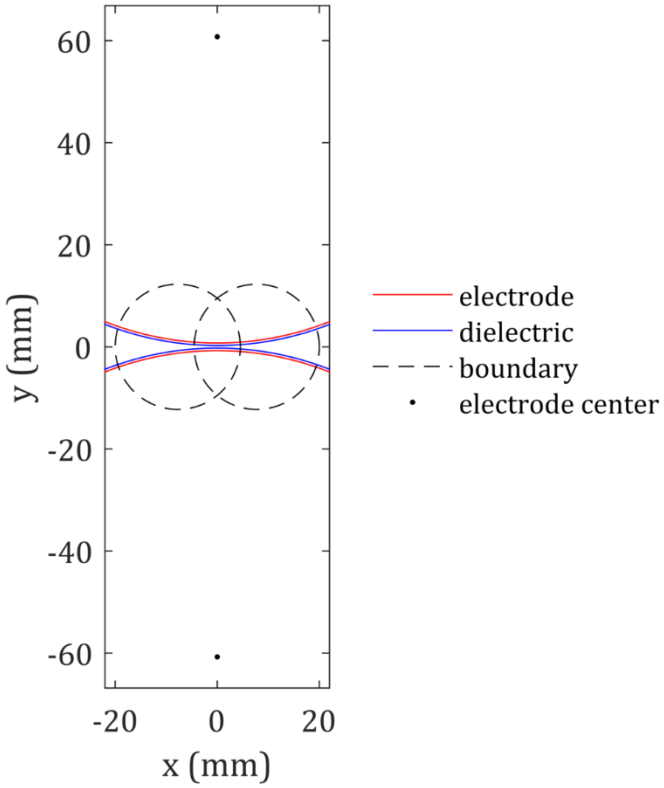


Figure 4.1. Basic description of the model geometry using Cartesian coordinates as described by equation 4.1.1 (electrode center), 4.1.2 (electrodes), 4.1.3 (dielectric) and 4.1.11 (boundary). Only the outer (left and right) arcs of the boundary circles, crossing the electrodes describe the actual boundary. Arbitrary values were chosen.

Models as in Figure 4.1 can't be used directly in PLASIMO. PLASIMO (currently) only uses orthogonal coordinate systems. Here the dielectric foil is not orthogonal to the boundary. The outer boundaries (electrode and left/right boundary) were chosen to be orthogonal. This can be described using the bipolar coordinate system, which is supported by PLASIMO.

## 4.2. The bipolar coordinate system (conventional definition)

Standard coordinate systems such as Cartesian $(x, y)$ – used in section 4.1 – and polar $(r, \theta)$ are probably well known. Those systems map said coordinates to a point $\vec{x}$ in a Cartesian reference frame, were $\vec{x} = (x, y)$ and $\vec{x} = (r\cos\theta, r\sin\theta)$ for those two examples. Consequently, for the polar coordinate system $x(r, \theta) = r\cos\theta$ and $y(r, \theta) = r\sin\theta$ can be defined. In this present study the bipolar coordinate system with coordinates $(\sigma, \tau)$ is used.

The standard definition of the bipolar coordinate system is [49]

$$x(\sigma, \tau) = \alpha \frac{\sinh\tau}{\cosh\tau - \cos\sigma} \tag{4.2.1}$$

$$y(\sigma, \tau) = \alpha \frac{\sin\sigma}{\cosh\tau - \cos\sigma} \tag{4.2.2}$$

with ranges $\sigma \in [0, 2\pi)$ and $\tau \in (-\infty, +\infty)$. Note that $\tau$ always appears in hyperbolic functions and $\sigma$ in trigonometric functions.

The scale factors $h$ are required as PLASIMO input.

$$h_\sigma = h_\tau = \frac{\alpha}{\cosh\tau - \cos\sigma} \tag{4.2.3}$$

The scale factors are related to the unit vectors and are used in general definitions of operators (e.g. the Laplacian). Section 4.5 discusses the meaning of the scale factors and their need.

Equation 4.2.1 and 4.2.2 describe circle arcs. For constant $\sigma$ the circle terminate in the foci $(\pm\alpha, 0)$. For $\sigma = \pi$ the line $y = 0$ is retrieved, $\sigma \in [0, \pi)$ describes positive $y$ and $\sigma \in (\pi, 2\pi)$ describes negative $y$. The line $x = 0$ corresponds to $\tau = 0$. Figure 4.2 shows this behavior.

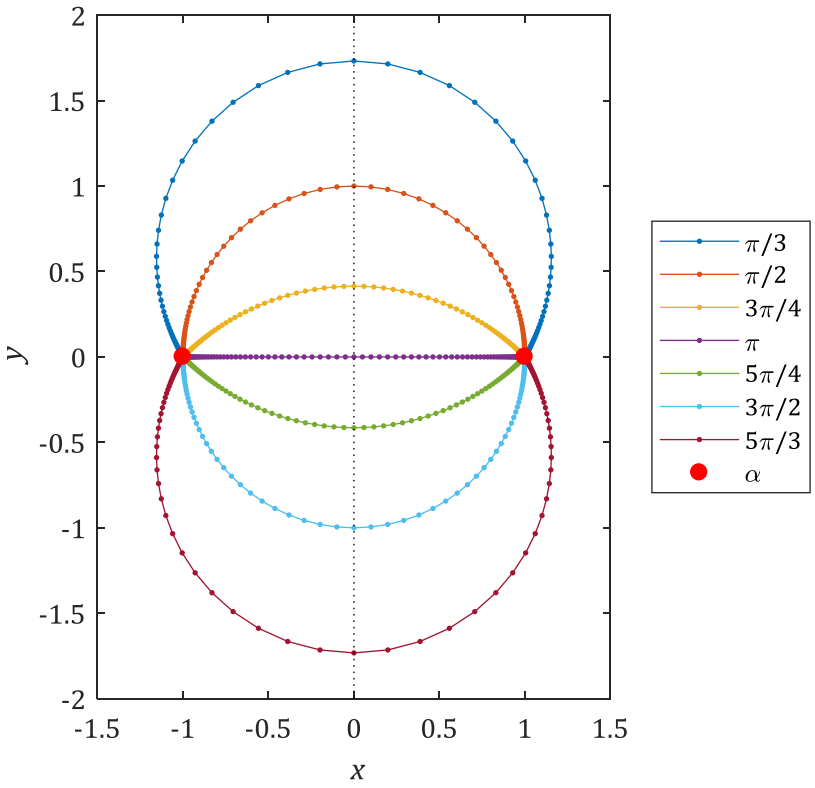


Figure 4.2. Curves of constant $\sigma$ (legend) plotted by equation 4.2.1 and 4.2.2, terminating in the foci $\alpha = 1$. With $\tau \in [-4,4]$ discretization includes $\tau = 0$ which lie on $x = 0$. One full circle is shown through the combination of $\sigma(= \pi/2)$ and $\sigma + \pi$.

The isocurves – curves of constant coordinate – are given by

$$x^2 + (y - \alpha \cot \sigma)^2 = \frac{\alpha^2}{\sin^2 \sigma} \tag{4.2.4}$$

$$(x - \alpha \coth \tau)^2 + y^2 = \frac{\alpha^2}{\sinh^2 \tau} \tag{4.2.5}$$

for $\sigma$ and $\tau$ respectively. They form non concentric circles on the $x = 0$ and $y = 0$ axis respectively. Note that in drawing equation 4.2.4 through a circle parameterization of $x$ and $y$ in $t$

$$\begin{cases} x(t) = r \cos t + a \\ y(t) = r \sin t + b \end{cases} \tag{4.2.6}$$

that for $t \in [0,2\pi]$ all bipolar coordinate lines are already drawn by $\sigma \in [0, \pi)$. Instead if one would want to visualize with 4.2.4 the coordinate lines of $\sigma$ in this way, $t \in [0, \pi]$ is recommended. This range does not indicate in general the actual termination of $\sigma$ curves in the foci $\alpha$ – requiring a range $t(\sigma)$, but gives a better idea of the evolution of $\sigma$ over the full range $[0,2\pi)$ (positive $y$ to negative $y$) – $\pi$ is excluded in this description. This is depicted in Figure 4.3. The second coordinate, $\tau$, is more straight forward. Negative values result in circles with $x < 0$, large $|\tau|$ create smaller circles, enclosing the relevant focal point $\alpha$. Values close to 0 create larger circles, 0 itself is excluded in this description. Figures 4.4 shows those curves of constant $\tau$.

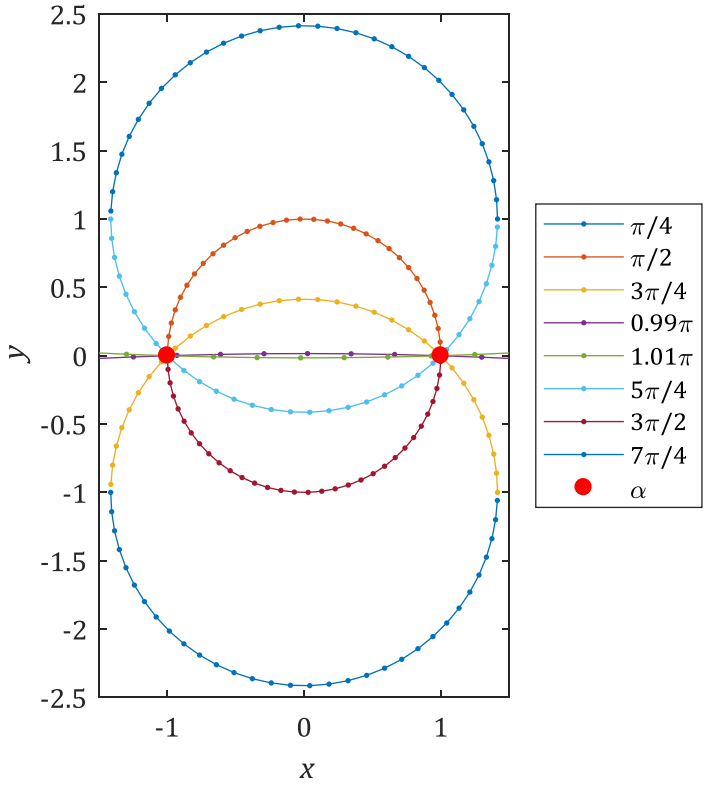


Figure 4.3. Curves of constant $\sigma$ plotted by a circle parametrization in $t \in [0, \pi]$ of equation 4.2.4. Through the combination of $\sigma$ and $\pi + \sigma$ three full circles are shown here.

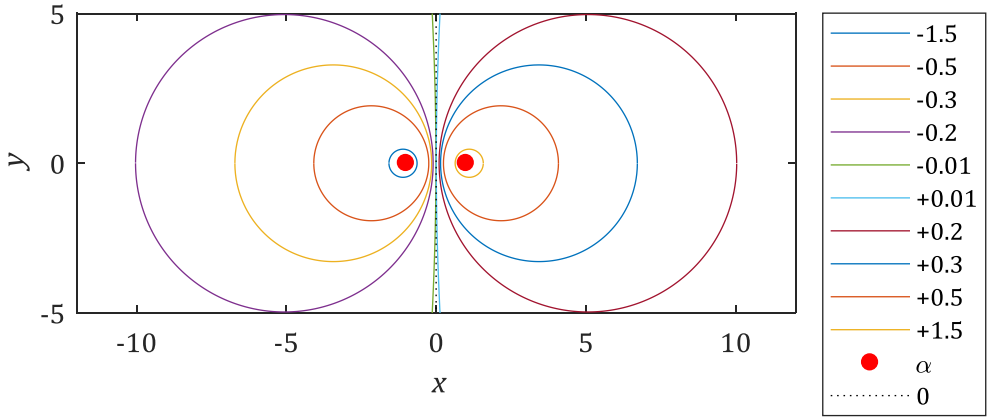


Figure 4.4. Curves of constant $\tau$ plotted by a circle parametrization in $t \in [0,2\pi]$ of equation 4.2.5 except for $\tau = 0$ which is drawn through equation 4.2.1 and 4.2.2.

Multiplying equation 4.2.4 and 4.2.5 with $\cos^2\sigma + \sin^2\sigma = 1$ and $\cosh^2\tau - \sinh^2\tau = 1$ respectively yields [49]

$$\sigma(x,y) = \operatorname{atan}\left(\frac{2\alpha y}{x^2 + y^2 - \alpha^2}\right) \tag{4.2.7}$$

$$\tau(x,y) = \operatorname{atanh}\left(\frac{2\alpha x}{x^2 + y^2 + \alpha^2}\right) \tag{4.2.8}$$

In above equations one should be aware of the discontinuities and asymptotic behavior.

The standard form (equation 4.2.1 and 4.2.2) of the bipolar coordinate system will not be used exactly, section 4.3 will introduce a modified (rotated) form.

## 4.3. Bipolar description

To describe the outer boundaries, as were introduced in section 4.1 with a Cartesian description, through the conventional bipolar coordinate system that was introduced in section 4.2, conceptually the Cartesian described boundaries are rotated counter clockwise 270° such that the powered electrode is now on the right instead of on top. This is the setup that will initially be described with the bipolar system.

The electrode boundaries, now on the left and right and centered about $(\pm b, 0)$, correspond to curves of constant $\tau$. Comparing this to equation 4.2.5 gives

$$\alpha \coth\tau \equiv b \tag{4.3.1}$$

$$\frac{\alpha}{\sinh\tau} \equiv R_E \tag{4.3.2}$$

where $R_E$ was the electrode radius. From this can be derived that the electrode boundaries are described by a single $\tau \equiv \tau_E$, which also fixes the location $\alpha$ of the foci [49]

$$\tau_E = \operatorname{acosh}\frac{b}{R_E} \tag{4.3.3}$$

$$\alpha^2 = b^2 - R_E^2 \tag{4.3.4}$$

This alpha was also already defined in the Cartesian description (equation 4.1.10) upon choosing the outer boundaries to be orthogonal to each other. One outer model range is now described by $\tau \in [-\tau_E, +\tau_E]$.

The open boundaries, now located top and bottom with outer boundaries at $(0, \pm l)$, correspond to curves of constant $\sigma$. Comparing equation 4.2.4 to condition 4.1.6 yields

$$\sigma_0 = 2\operatorname{atan}\frac{\alpha}{l}, \qquad l \geq 0 \tag{4.3.5}$$

where the constraint on $l$ has been introduced to ensure that $\sigma_0 \in [0, \pi]$ such that $\sigma \in [\sigma_0, 2\pi - \sigma_0]$ describes the second model range.

The dielectric layer on the electrodes should also be described by a constant coordinate $\tau \equiv \tau_\epsilon$. Considering the smallest gap between the electrodes, the dielectric gas interface should lie at $(x, y) = (d_g/2\,, 0)$. Substituting this in equation 4.2.8 yields

$$\tau_\epsilon = 2\,\mathrm{atanh}\frac{d_g}{2\alpha} \tag{4.3.6}$$

Compared to equation 4.2.8 the form has been simplified according to the derivation in appendix I.A. Note that $\alpha$ is still according to equation 4.3.4, fully determined by the outer (electrode) boundaries.

In order to have the model represent a vertical discharge, with the powered and grounded electrode again on top and bottom respectively, the actual implementation of the bipolar coordinate system (equation 4.2.1 and 4.2.2) is rotated counter clockwise by 90°.

$$x(\sigma, \tau) = -\alpha\frac{\sin\sigma}{\cosh\tau - \cos\sigma} \tag{4.3.7}$$

$$y(\sigma, \tau) = \alpha\frac{\sinh\tau}{\cosh\tau - \cos\sigma} \tag{4.3.8}$$

Figure 4.5 shows the eventual bipolar model after this rotation. Equation 4.2.7 and 4.2.8, giving the relations $\sigma(x, y)$ and $\tau(x, y)$, were derived from the conventional definition of the bipolar coordinate system. This does not hold for the rotated system (equation 4.3.7. and 4.3.8). Appendix I.B presents the relations $\sigma(x, y)$ and $\tau(x, y)$ that were used in this study for this latter case, while also ensuring the result lies properly in the range $\tau \in [-\tau_E, +\tau_E]$ and $\sigma \in [\sigma_0, 2\pi - \sigma_0]$.

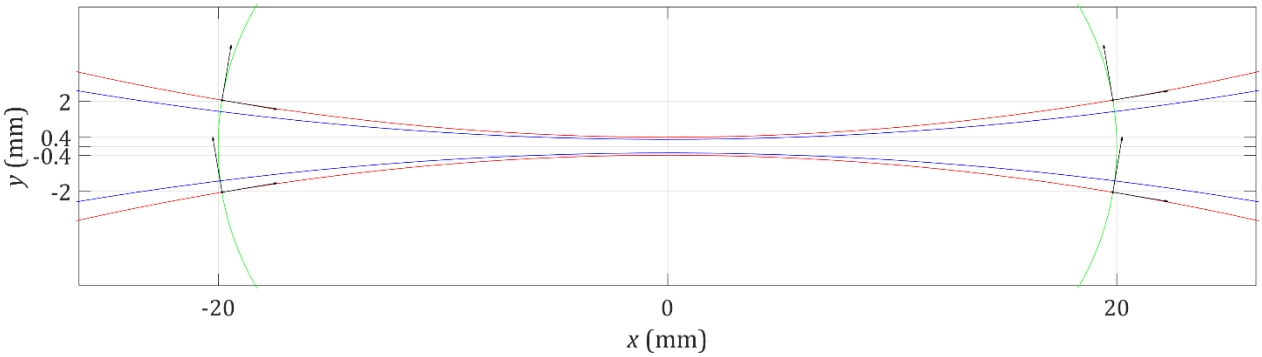


Figure 4.5. The eventual geometric model based on the bipolar coordinate system after rotation (equation 4.3.7 and 4.3.8). The electrode boundary in red, the open boundaries in green and the dielectric profile imposed by the coordinate system in blue. The $y$ axis indicate the electrode position at the smallest gap. In addition the unit vectors are indicated at the intersections (also indicated on the $y$ axis) of the outer boundaries. Axes to scale. The values $R_E = 120$, $l = 20$, $d_g = 0.6$ and $d_\epsilon = 0.1$ mm was used here.

### 4.3.1. An asymmetric case: flat bottom electrode

In the bipolar description of the 2D model, the electrode setup has been described symmetric up till now. Some experiments are conducted in a plasma reactor with a flat bottom and curved top electrode [14]. In order to describe this, the model boundaries for $\tau$ are redefined as $\tau \in [0, +\tau_E]$ this removes the lower half of the original description (below $y = 0$). The *CellMatrix* (introduced in the next section 4.4) is not altered. By using a new effective gap size $d_g'$ and setting $d_g \to d_g'$ with

$$d_g' = 2\big(d_g + d_\epsilon\big) \tag{4.3.9}$$

The adjusted range results in the correct configuration[1]. The boundary $\tau_E$ is still calculated with the original expression (equation 4.3.3) after this substitution (4.3.9). The upper boundary $\tau_\epsilon$ is also still calculated as before with the substitution. The bottom dielectric lies at $d_\epsilon$ instead of $d_g'/2$ – at the minimum gap – such that

$$\tau_{\epsilon,flat} = 2\,\mathrm{atanh}\frac{d_\epsilon}{\alpha} \tag{4.3.10}$$

were the subscript indicates that this value belong to the description of the flat electrode. Figure 4.6 shows a contour plot of the 2D model from an actual simulation – implemented by means of the description given here – together with the analytical curves of $\tau_\epsilon$ and $\tau_{\epsilon,flat}$ which actually do not actively occur in the code (see next section 4.4).

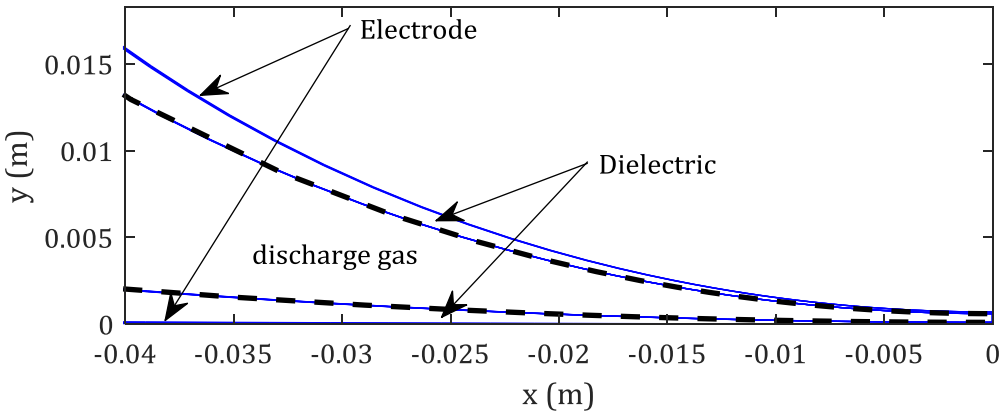


Figure 4.6. Excerpt of the contours of an asymmetric 2D model implemented with bipolar coordinates and the analytical values for the dielectric interfaces (dashed lines), visually validating the substitution of $d_g \rightarrow d_g'$ (equation 4.3.9).

### 4.3.2. Constraints on the dielectric thickness

In the bipolar coordinate system the electrode boundary was derived as $\tau_E$ (equation 4.3.3), during this derivation the foci $\alpha$ of the coordinate system were also defined. The dielectric is described by $\tau_\epsilon$ (equation 4.3.6) by assuming the actual dielectric thickness at the smallest gap size. Because $\alpha$ is fixed by the outer model boundary and $\tau$ forms non concentric circles, the circle of constant $\tau_\epsilon$ does not and cannot describe proper uniform coverage of the electrode by the dielectric (equation 4.1.3). This is also shown in both Figure 4.5 and 4.6. However in the two-dimensional modelling in present study, the main interest lies on the inherently non-homogenous electric field due to the plasma reactor geometry. While those constraints on the dielectric layers do not allow for a completely correct representation of the experimental setup, it does not remove the inhomogeneous electric field. In principle the two-dimensional modelling efforts under those constraints should still hold valuable insights into the plasma formation and expansion in those roll-to-roll geometries.

## 4.4. PLASIMO input: 1D *CellVector* and 2D *CellMatrix*

A 1D model is also used throughout the study for faster computation time, the discharge direction is considered only – across the smallest gap. The model should describe all the material interfaces. In

[1] Consider that in the original case, the positive half consisted of $d_g/2$ and $d_\epsilon$ before reaching the electrode. Now the full $d_g$ and an additional $d_\epsilon$ is needed in the space of what was originally $d_g/2$, noted $d_g'/2$ .

PLASIMO the inner dimensions are defined only through the *CellVector/CellMatrix* and material allocation. The complete model lengths is set.

The 1D model is defined on $y \in [-y_0, +y_0]$ with $y_0 = d_g/2 + d_\epsilon$, $d_g$ the full gaseous gap size and $d_\epsilon$ a single dielectric thickness. The plasma region is then $y \in (-d_g/2\,, +d_g/2)$.

The *CellVector* is shown in Figure 4.7. The required blocks of the interior (dielectric layer and discharge gas) can be determined by

$$\frac{N_\epsilon}{N_g + 2N_\epsilon} = \mathrm{rat}\left(\frac{d_\epsilon}{d_g + 2d_\epsilon}\right) \tag{4.4.1}$$

where $N_\epsilon$ and $N_g$ are the amount of cell blocks per dielectric layer and for the full gas gap respectively and $\mathrm{rat}(x)$ gives the rational fraction approximation of $x$.

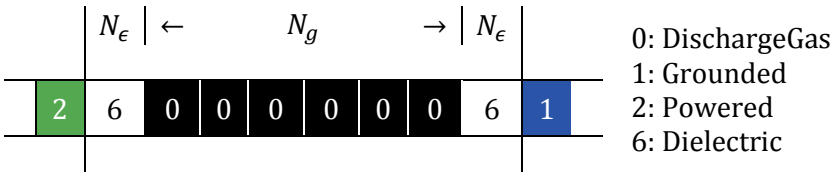


Figure 4.7. The used *CellMatrix/Vector* as required for the PLASIMO input for the one dimensional models. The long vertical lines differentiate the interior from the boundary materials. Indices 1 and 2 are the electrodes. Shown configuration valid for e.g. $d_g = 0.6$ mm and $d_\epsilon = 0.1$ mm.

The resulting grid can be refined through options other than the cell matrix itself, introduced in section 4.6.

This *CellVector* will also be the basis for the *CellMatrix* of the 2D model.

In two-dimensional models, the discharge will be defined to run from top to bottom, i.e. vertical, similar to the experimental plasma reactor. The cell matrix/vector in Figure 4.7 is taken twice, side by side, to better reflect symmetry. The additional boundaries in the two dimensional model are designed such that it could support flow. Figure 4.8 shows the basic 2D model *CellMatrix*.

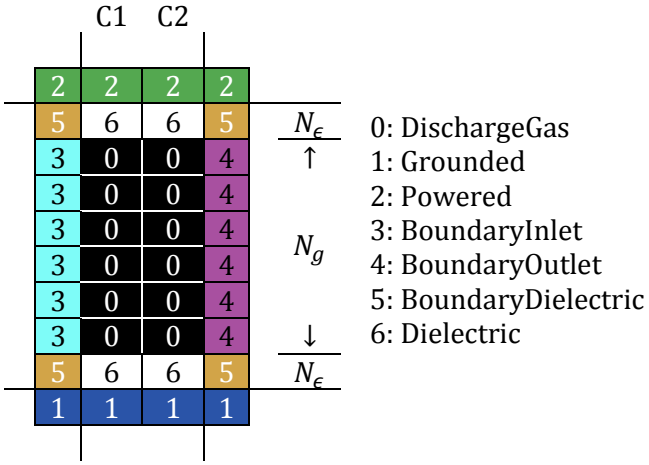


Figure 4.8. The basic *CellMatrix* as required for the PLASIMO input for two-dimensional models. The lines differentiate the interior from the boundary materials. Indices 1 and 2 are the electrodes. Shown configuration valid for i.e. $d_g = 0.6$ mm and $d_\epsilon = 0.1$ mm.

In principle the model is symmetric over the discharge gas, in the horizontal direction. Aiming for less computation time, half of the full 2D model can be simulated. To do this, column C2 in Figure 4.8 is removed (in addition, the full model dimensions should be adjusted accordingly – flow should not be used).

This 2D *CellMatrix* is applied to the bipolar coordinate system having coordinate ranges $\tau \in [-\tau_E, +\tau_E]$ and $\sigma \in [\sigma_0, 2\pi - \sigma_0]$ (or $\sigma \in [\sigma_0, \pi]$ for the half model), however the amount of blocks in the CellMatrix were still determined using equation 4.4.1. Figure 4.9 indicates the boundaries in the Cartesian case and in the bipolar case. Comparing those boundaries yields that the ratio used in equation 4.4.1 becomes

$$\frac{d_\epsilon}{d_g + 2d_\epsilon} \rightarrow \frac{\tau_E - \tau_\epsilon}{2\tau_E} \tag{4.4.2}$$

It can be shown that

$$\frac{\tau_E - \tau_\epsilon}{2\tau_E} \approx \frac{d_\epsilon}{d_g + 2d_\epsilon} \tag{4.4.3}$$

as long as $b/R_E \approx 1$, $d_g/2\alpha \ll 1$ and $R_E D \ll R_E^2\left(d_g + 2d_\epsilon\right)^2$ were $D$ is defined as

$$D \equiv \frac{d_g^3}{4} + \frac{3d_g^2 d_\epsilon}{2} + 3d_g d_\epsilon^2 + 2d_\epsilon^3 \tag{4.4.4}$$

The derivation of this statement is given in appendix I.C. Those conditions are readily met as typically $d \ll R_E$ (for both subscripts) in interests of this study. As an example for $d_g = 0.6$, $d_\epsilon = 0.1$ and $R_E = 120$ mm [11], the Cartesian ratio yields 0.1250 while the bipolar ratio yields 0.12509. In this case $b/R_E = 1.00\overline{3}$, $d_g/2\alpha = 0.0306$ and $R_E D = 1.5 \cdot 10^{-11}$ while $R_E^2\left(d_g + 2d_\epsilon\right)^2 = 9.2 \cdot 10^{-9}$. The Cartesian ratio rationalizes to 1/8 while the precise bipolar ratio rationalizes to 515/4117 such that a cumbersome 4117x2 instead of 8x2 cells[1] would be necessarily in the cell matrix to describe the model interior. Changing to $R_E = 60$ mm and $d_g = 1$ mm, the Cartesian and bipolar ratio are $0.83\overline{3}$ and 0.835 respectively. The above does mean that the value of $\tau_\epsilon$ does not actively occur in the PLASIMO input in current geometry implementation.

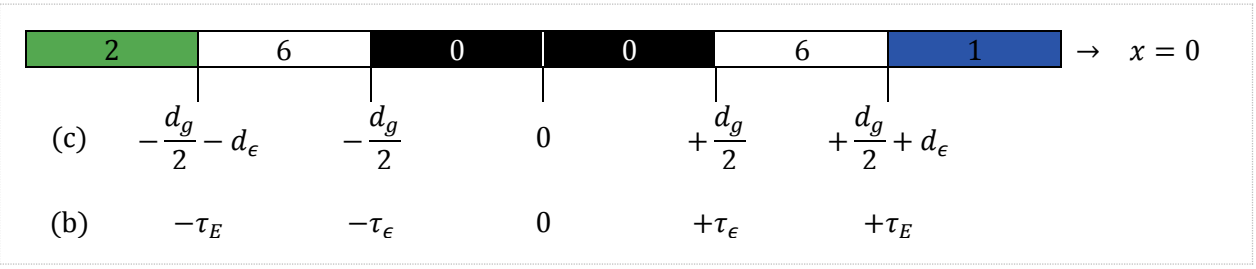


Figure 4.9. The material interface definitions along the center of a vertical discharge in the Cartesian (c) and bipolar (b) definitions. With 0: the discharge gas, 6: the dielectric and 1 and 2: the electrodes.

[1] PLASIMO allows for grid refinement through other options than the *CellMatrix* itself (see equation 4.5.12), a grid of ~4117 effective cells in the discharge direction is approximately one order of magnitude larger than actively used in the models throughout this study.

## 4.5. Grid generation

Section 4.2 gave some examples of coordinate systems and introduced the bipolar coordinate system with coordinates $(\sigma, \tau)$. Here those coordinates will be given the general name $p_i$ which are mapped to Cartesian reference frames $(x, y, z)$ through $\vec{x} = \vec{x}(p_1, p_2, p_3)$ in the 3D case.

Internally PLASIMO works with normalized coordinate systems ($\in [0,1]$), to that end $s_i \in [0,1]$ is introduced. The actual coordinates $p_i$ relate to $s_i$ through the outer coordinate ranges (minimum and maximum values of $p_i$) by

$$p_i = p_{i,min} + s_i\left(p_{i,max} - p_{i,min}\right) \tag{4.5.1}$$

Consequently $s_i = s_i(p_i)$ normalizes $p_i$. An addition normalized coordinate system $c_i \in [0,1]$ is introduced. Those normalized systems are related to each other by the *stretch functions* $f_i$

$$s_i = f_i(c_i) \tag{4.5.2}$$

The *stretch functions* $f_i(c_i)$ are also normalized, $f_i \in [0,1]$, with addition constrains

$$f_i(0) = 0 \tag{4.5.3}$$

$$f_i(1) = 1 \tag{4.5.4}$$

$$f_i'(c_i) > 0, \qquad 0 \le c_i \le 1 \tag{4.5.5}$$

In total, the normalized *computational grid* $c_i$, the *stretch functions* $f_i(c_i)$, the normalized *stretched grid* $s_i = f_i(c_i)$, the *scaled grid* $p_i = p_{i,min} + s_i\left(p_{i,max} - p_{i,min}\right)$ and the *projected grid* $\vec{x} = (p_1, p_2, p_3)$ were defined and introduced, such that also $\vec{x} = \vec{x}(c_1, c_2, c_3)$.

In order to perform proper calculations based on the *computational grid* $\vec{c}$, physical values for the lengths $L_i$ (and related area and volume) are required. A physical distance $dL_i$ should correspond to a displacement $dc_i$, given by

$$dL_i = h_i^{(c)} dc_i \tag{4.5.6}$$

where $h_i^{(c)}$ is the scale factor with respect to the *computational grid*. Considering the range of $c_i$ it follows that

$$L_i = h_i^{(c)} \tag{4..7}$$

Those scale factors are given by

$$h_i^{(c)} = \left|\frac{d\vec{x}(c_1, c_2, c_3)}{dc_i}\right| \tag{4.5.8}$$

Using equation 4.5.8, 4.5.1 and 4.5.2 it follows that

$$h_i^{(c)} = h_i^{(p)}\left(p_{i,max} - p_{i,min}\right) f_i'(c_i) \tag{4.5.9}$$

where

$$h_i^{(p)} = \left| \frac{d\vec{x}(p_1, p_2, p_3)}{dp_i} \right| \tag{4.5.10}$$

which are known relations for any orthogonal (curvilinear) coordinate system. For the bipolar coordinates $h_i^{(p)}$ was given in section 4.2, equation 4.2.3.

Equation 4.5.10 and 4.5.8 show the need for the definition of the scale factors – a required input for user defined grids in PLASIMO. PLASIMO also offers the option for user defined *stretch function* $f_i$. This requires both $f_i(c_i)$ and $f_i'(c_i)$ to be given explicitly.

The *computational grid* $c_i$ is discretized into $N_i \in \mathbb{Z}^>$ points having indexes $k_i \in [0, N)$, the equidistant $c_i \in [0,1]$ is then calculated with

$$c_i(k_i) = \frac{k_i}{N_i - 1} \tag{4.5.11}$$

For *stretch functions* other than $f_i(c_i) = c_i$, the *stretched grid* $s_i$ will be unevenly distributed, as will be the coordinates $p_i$.

Section 4.4 introduced the *CellVector* and *CellMatrix*. Figure 4.7 showed that the *CellVector* consists of interior and exterior blocks, the latter representing the boundary. The number of interior blocks is here defined as $\eta_i \in \mathbb{Z}^>$. The $N_i$ points in the *computational grid* is then calculated by

$$N_i = \eta_i \cdot 2^{1+b_i+\beta} + 1 \tag{4.5.12}$$

where the *BaseRefinementPower* $b$ and the *RefinementPower* $\beta$ are defined.

All in all, the above achieves a uniform computational mesh while being able to control the spacing of points in the physical space.

### 4.5.1. The material and control volume grids

From the *master grid* – the grid that contains all points, i.e. the equidistant *computational grid* – various sub grids are constructed on which the transport equations are solved using a control volume method [16]. In this construction a *material grid* [16] consisting of *nodal points* is staggered with a *control volume grid* [16]. The latter is represented by a separate grid for each individual dimension representing control volume surfaces – which are allocated *face points*, on which the respective fluxes are defined. Additionally, a *corner grid* is constructed. Figure 4.10 visualizes this for a 2D grid, including two boundaries.

Subdomains within the interior can be defined in the *CellVector* or *CellMatrix*. See for example Figures 4.6, 4.7 and 4.8, where the interior consists of the dielectric and discharge gas. A subdomain (for the actual plasma) containing only the discharge gas should be defined. Boundary locations of those subdomains in the eventual grid representation $\vec{x}$ are defined by the ratios as defined in the *CellMatrix*. The use of stretching functions does not displace those boundary locations – other than through the coarseness of the grid, instead the *nodal points* of the *material grid* have their material properties (e.g. being a dielectric) reallocated according to the ratios in coordinates $p_i$ as are defined in the *CellMatrix*. The grid point allocations in a subdomain at the subdomain boundaries are analogous to the boundary in Figure 4.10.

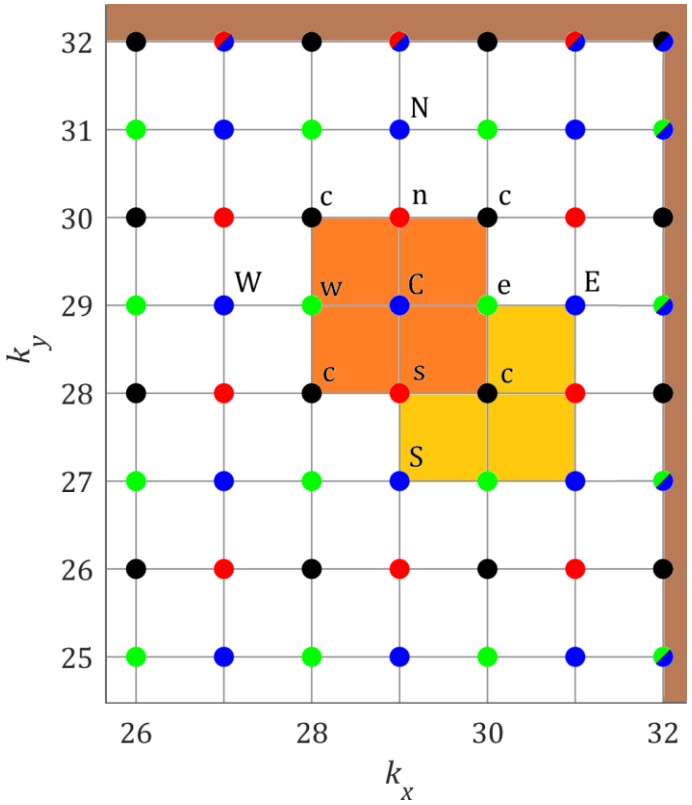


Figure 4.10. Excerpt of the master grid (all points/dots) represented by the indexes $k_i$ with $i = (x, y)$ – including the boundary ($k_i = 32$) – visualizing the *material grid* with the *nodal points* (blue ● and uppercase C, N, S, E, W) and the *volume grid* with the *face points* on which the fluxes in the $x_1$-direction (green ● and lowercase w and e) and $x_2$-direction (red ● and lowercase s and n) are defined. The *corner* points are also drawn (black ● and lowercase c). A single cell of the staggered *material grid* (yellow ■) and the *control volume grid* (orange ■, on top) are drawn. The boundary is colored brown (■). The boundary shares allocation of the *nodal points* with *face points* (◕ and ◕) and *corner points* (◕). This Figure, and the labels C, N, S, E, W, n, s, e and w, are after, and analogous to, Figure 3.1 of [16]. Some definitions have changed.

### 4.5.2. The grid generation applied to the bipolar coordinate system

Starting from Figure 4.8, the 2D *CellMatrix*, $\eta$ is counted as $\eta_i = (8,2)$. For clarity, low refinements are chosen, $b_i = (1,2)$ and $\beta = 0$. From equation 4.5.12 follows $N_i = (33,17)$. This creates $33 \times 17$ points. Using equation 4.5.11, $\vec{c}$ is constructed, shown in Figure 4.12a. This example uses 1-point stretch function (for both coordinates)

$$f_i(c_i) = c_i - \frac{3}{2}\left(c_i^2 - c_i\right) + 3\left(c_i^3 - c_i^2\right) \tag{4.5.13}$$

PLASIMO support n-point stretch functions, of which the 1-, 2-, 3- and 4-point stretch function were often used in this study. Those stretch function are defined such that they allow an increased grid density at $n$-specific points. Those stretch functions are based on polynomials of order $2n + 1$. The derivation is rigorous, it was chosen to not present it here however appendix I.D gives a general solution. Figure 4.11a shows a couple of 1-point stretch functions and Figure 4.11b shows the corresponding grid density, equal to the reciprocal of the derivative of the stretch function $(1/f_i'(c_i)$. The stretch function that is actually used in this example sets the grid density to 4 at $c_i = 0.5$.

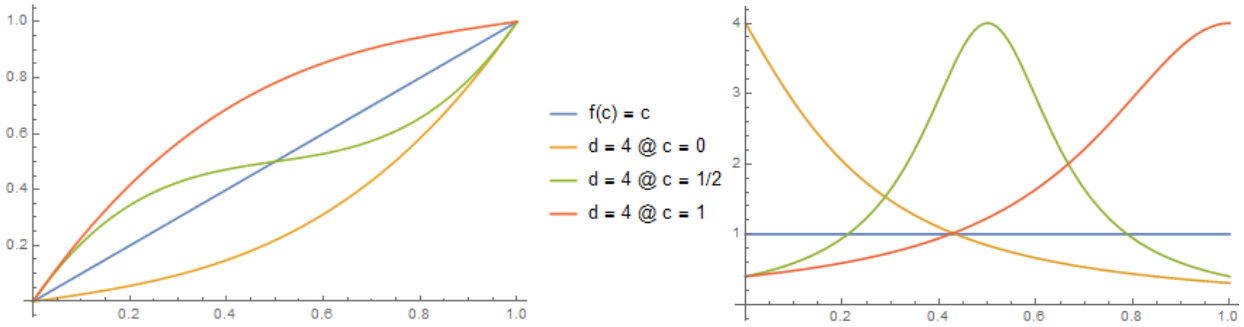


Figure 4.11. Examples of 1-point stretch functions (left) where a grid density $d$ is fixed on a location $c$. The right Figure shows the grid density, the reciprocal of the derivative of the stretch function.

Figure 4.12b shows the *stretched grid* by equation 4.5.2. The next step is to calculate the *project grid* using equation 4.5.1. For the bipolar coordinate system $(p_1, p_2) \equiv (\sigma, \tau)$, the boundaries were defined in section 4.3 as $\sigma \in [\sigma_0, 2\pi - \sigma_0]$ and $\tau \in [-\tau_E, +\tau_E]$. Using equation 4.3.3, 4.3.4, 4.3.5 and 4.1.1 and choosing $l = 20$ mm, $R_E = 120$ mm, $d_g = 0.6$ mm and $d_\epsilon = 0.1$ mm results in Figure 4.11c. Finally, equation 4.3.7 and 4.3.8 (the rotated bipolar coordinate system) is used to map this to cartesian coordinates $(x, y)$, shown in Figure 4.13.

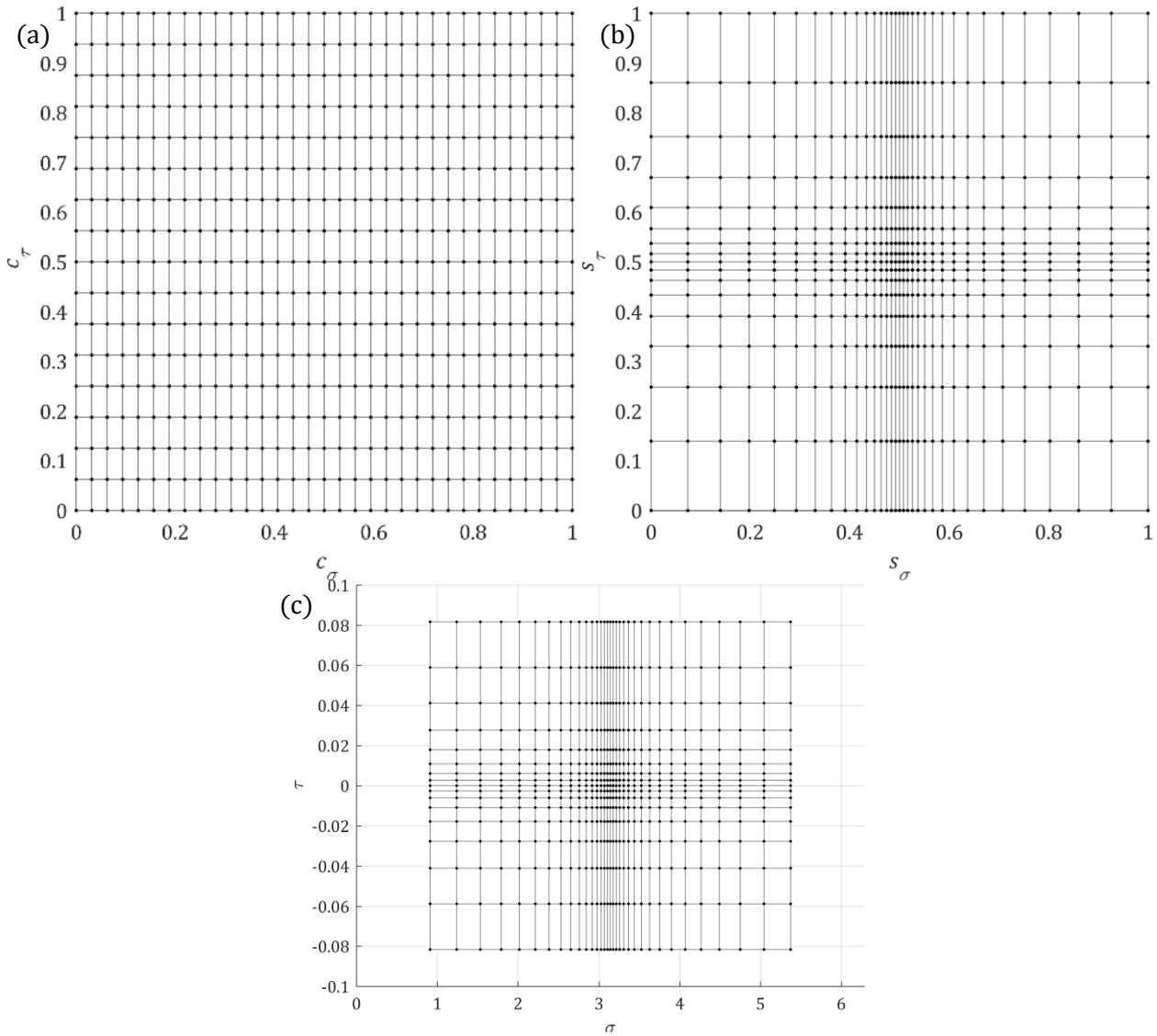


Figure 4.12. Various intermediate grid steps in the generation of the *master grid* showing the equidistant *computational grid* $c_i$ (a), the *stretched grid* $s_i$ (b) and the *scaled grid* $\vec{p} \equiv (\sigma, \tau)$ (c).

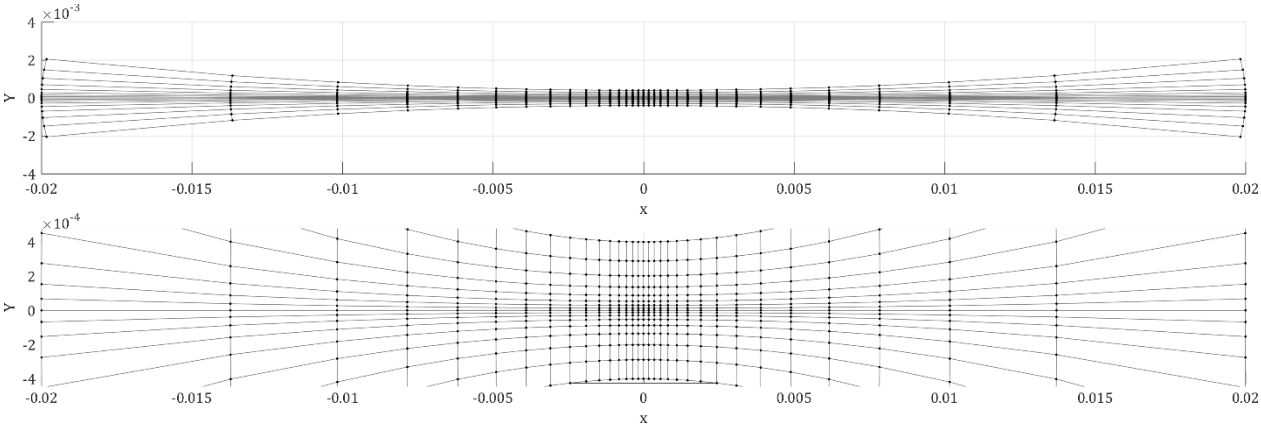


Figure 4.13. The eventual *projected grid* for a bipolar coordinate system showing the full master grid (a) and a detail of the narrow gap (b). Axes represent meters.

# Part 2:
# Results

# 5. Atmospheric pressure argon dielectric barrier discharge: structure and main processes


## Abstract

An atmospheric pressure argon dielectric barrier discharge is modelled. The structure of the discharge is reported through the current and voltage characteristics and spatial temporal data of various plasma parameters, including the reaction rates. Especially stepwise ionization and associative metastable-metastable ionization are considered as well as briefly dissociative recombination. The modelling results for discharges with a reduced amount of reactions are also presented.


Section 5.1 shows the discharge structure through the electric field and mean electron energy, the species densities, volume charge, reaction rate, spatially averaged rate contributions and the species production to destruction ratio. Section 5.2 modifies the chemistry input and considers the role of stepwise ionization, direct ionization, associative metastable-metastable ionization and dissociative recombination. The conclusions are given in section 5.3.

## 5.1. Discharge structure and reaction rates

The discharge is presented for one specific set of conditions. The results are that of one-dimensional models. The background gas temperature is 450 K [51], the pressure is 1 atm, the dielectric thickness is 0.1 mm, the dielectric constant is 3.4 and the gas gap is 1 mm. The applied voltage is sinusoidal with an amplitude of 1 kV at a frequency of 200 kHz (see also section 1.1). The secondary electron emission coefficient for all non-constant argon species is set as 0.1. Of specific interest are the gas gap, applied voltage amplitude and the secondary electron emission coefficient – in this chapter fixed to aforementioned values. This set is found to be representative of plasma characteristics over a wide range for those three specific input parameters, showing all features that can occur.

### 5.1.1. Electrical characteristics

Figure 5.1 shows the current and voltage characteristics [1]. A first sharp current peak is observed and a broad shoulder that shows a multi-peak behavior, the latter does not yet occur very strongly.

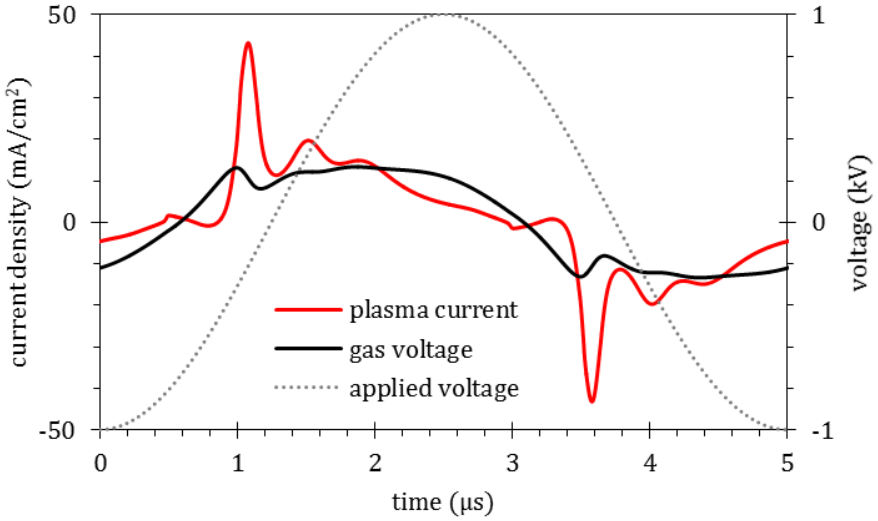


Figure 5.1. Current and voltage characteristics during one steady state voltage cycle.

### 5.1.2. Species densities and volume charge

In Figure 5.2 an overview is given of all the species densities considered during one cycle. The coordinate $y$ represents the position along the smallest part of the gaseous gap with $y = 0$ the center between the electrodes (see also Figure 1.1). The sheath is visualized with a solid line, retrieved by calculating an equivalent sharp electron step [52], here calculated in post processing by finding the minimal $\Sigma(s)$ at each time set with

$$\Sigma(s) \equiv \int_{-d_g/2}^{s} n_e(y)dy - \int_{s}^{+d_g/2} \left(n_{ions}(y) - n_e(y)\right)dy\,, \qquad -\frac{d_g}{2} \le s \le +\frac{d_g}{2} \tag{5.1}$$

Based on the electron density, the discharge presents a glow-like structure with a cathode fall, negative glow, faraday dark space, positive column and anode dark space region [53]. The maximum electron density in the negative glow and positive column is about equal. The atomic ions are found in the cathode fall, mainly during the first breakdown, they are also observed at the wall. The molecular ions are present both in the negative glow peak and the cathode fall. A high density is observed at the wall as well as a clear non-zero density throughout the whole plasma and an elevated density in the positive column region. The density of metastables increases rapidly at the initial breakdown and continues so in the cathode fall. The density from the previous discharge lingers on, decreasing continuously.

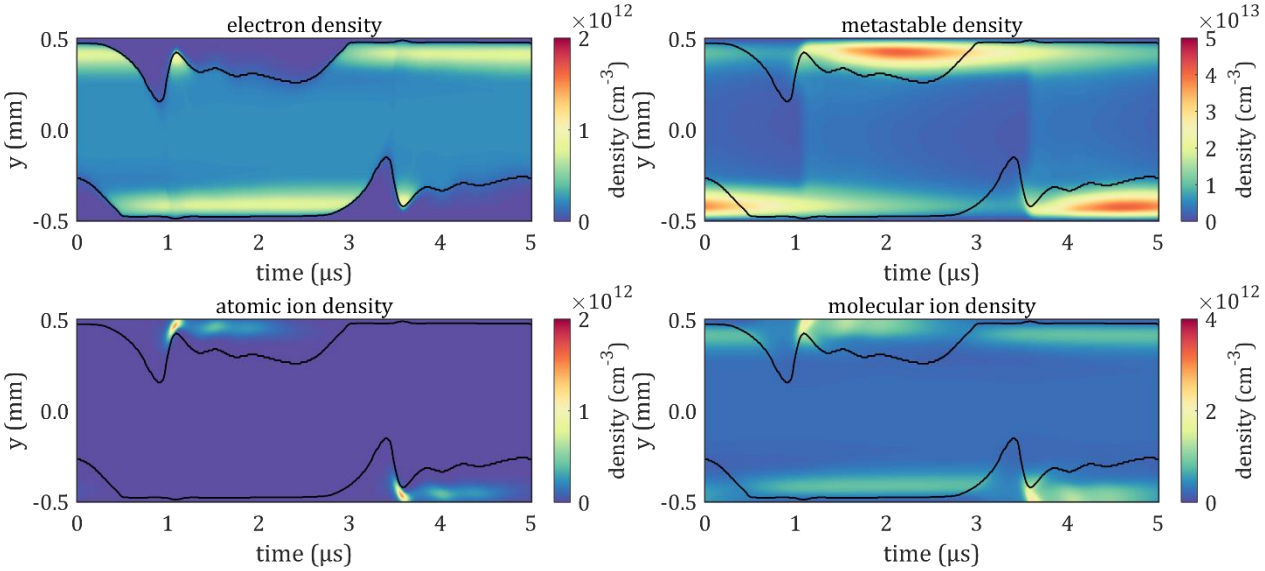


Figure 5.2. All densities during a steady state voltage cycle corresponding to Figure 5.1. Including the sheath edge drawn with a solid line.

Figure 5.3 shows the density profiles at the time of maximum electron density in the negative glow. It indicates that the plasma bulk is neutral during the glow-like plasma structure. The location of the calculated sheath edge is also shown. It is seen that the molecular ion density increases throughout going from the plasma bulk into the cathode fall, before decreasing towards the wall.

Figure 5.4 shows the volume charge density. Here it is indicate that the plasma bulk is neutral also during the whole voltage cycle.

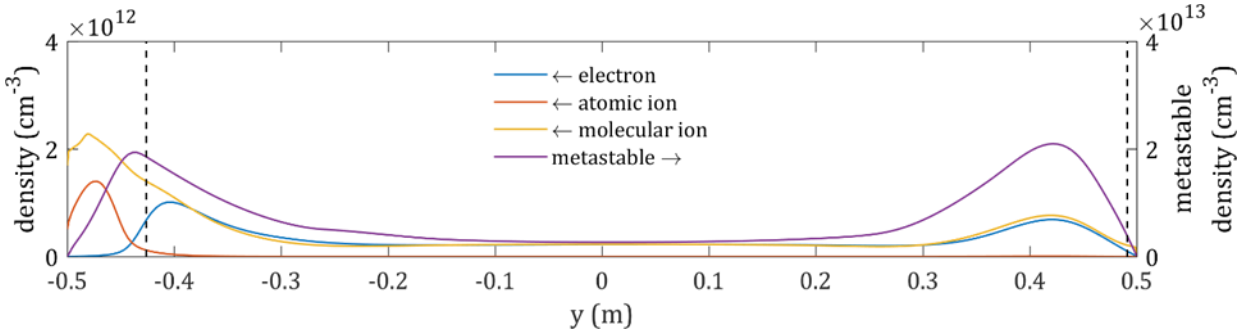


Figure 5.3. The density profiles along the gas gap at the maximum electron density in a negative glow peak. The sheath edges are shown with dashed lines. The instantaneous cathode is on the left. The metastables are approximately one order higher in density and uses the separate right axis.

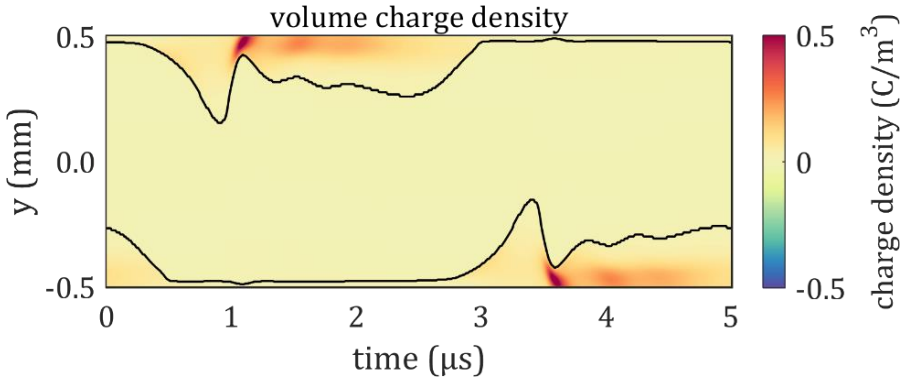


Figure 5.4. The volume charge density during a steady state voltage cycle corresponding to Figure 5.1. Including the sheath edge drawn with a solid line.

### 5.1.3. Electric field and mean electron energy

Figure 5.5 shows the electric field and Figure 5.6 shows the mean electron energy density as calculated from the model. High energies are correctly separated from the plasma bulk indicated by the sheath edge. The maximum absolute electric field is about 4 kV/mm, the maximum energy is about 8 eV. The electric field in the bulk looks uniform. The plasma bulk remains energetic (~5 eV) after the initial breakdown during some time while there is still a plasma sheath. At those observed energies the rate coefficients $k_r$ of stepwise ionization (SI), direct ionization (DI) and excitation (EXC) are approximately ordered as $k_{\mathrm{SI}} > k_{\mathrm{DI}} \geq k_{\mathrm{EXC}}$ for 8 eV and $k_{\mathrm{SI}} \gg k_{\mathrm{EXC}}$ and $k_{DI} \to 0$ for 5 eV, based on Figure 3.2.

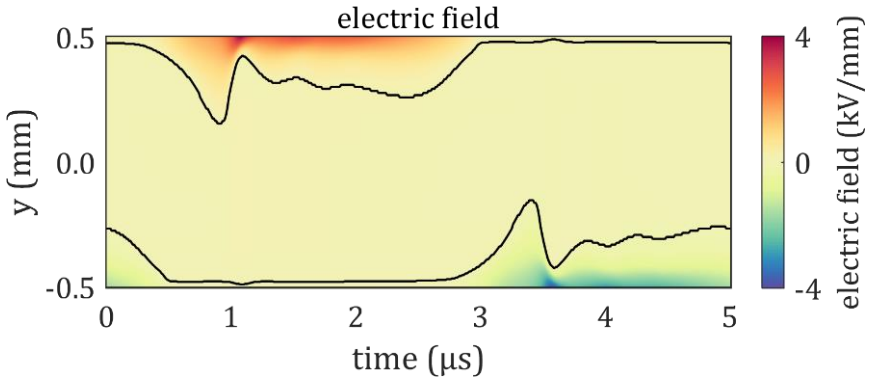


Figure 5.5. The electric field during a steady state voltage cycle corresponding to Figure 5.1. Including the sheath edge drawn with a solid line.

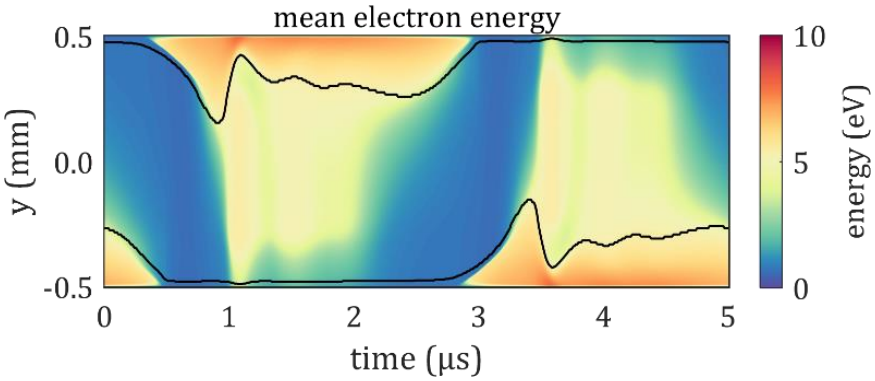

Figure 5.6. The mean electron energy during a steady state voltage cycle corresponding to Figure 5.1. Including the sheath edge drawn with a solid line.

### 5.1.4. Spatial temporal reaction rates

Figure 5.7 (next page) shows the spatial temporal reaction rates for all the 12 reactions in the fluid model (see Table 3.2) during one half cycle. In the following text the Figure is described by considering the eventual dependencies in the model of the calculated rate (equation 2.20) per reaction.

Excitation (5.7a) and direct ionization (5.7b) depend on the electron density and the mean electron energy. Excitation occurs both in the plasma sheath and in the bulk during breakdown. Direct ionization occurs in the sheath only and is overall smaller in feature size compared to excitation, due to higher required electron energy.

De-excitation (5.7e) and stepwise ionization (5.7i) both depend on the electron and metastable density and the mean electron energy. Both occur on the sheath edge and in the positive column, but stepwise ionization is more local. In considering those reactions the densities are equal for both. Both occur at low energies but the de-excitation has a higher rate coefficient (Figure 3.2a) and stepwise ionization still has a threshold energy.

Regular and associative metastable-metastable ionization (5.7f and 5.7j respectively) depend on the metastables only – required twice. The rates are completely determined by its density. Atomic to molecular ion conversion (5.7c) depends on the atomic ion density only and thus occurs in the sheath only, requiring the atomic ion to initiate this reaction locally. The inverse conversion (5.7g) depends on the molecular ion density only. The rate and rate coefficient (Figure 3.2) is significantly lower.

Dissociative recombination (5.7k) depends on the mean electron energy and electron and molecular ion density. The electron density has sharp cutoffs on the sheath edge, restricting this reaction to mainly take place in the bulk. This reaction predominantly takes place in the positive column and negative glow. Note also that the rate coefficient is lower for higher mean electron energy (Figure 3.2a) – as found in the sheath (Figure 5.6).

The three body recombination with an electron as the spectator (5.7d) depends on the electron and atomic ion density and on the mean electron energy, having lower rate coefficient at higher energies (Table 3.2). Due to this energy dependence the reaction does not occur at the negative glow. The rate is extremely low. Recombination with an argon atom as the spectator (5.7h) does not depend on the mean electron energy. This reaction also takes place in the positive column (hardly visible), however due to the lack of the energy dependency it is more pronounced around the sheath edge of the negative glow, which has simultaneous high electron and atomic ion density.

The radiative decay (5.7l) depends on the metastable density only, directly reflecting the metastable density (Figure 5.2).

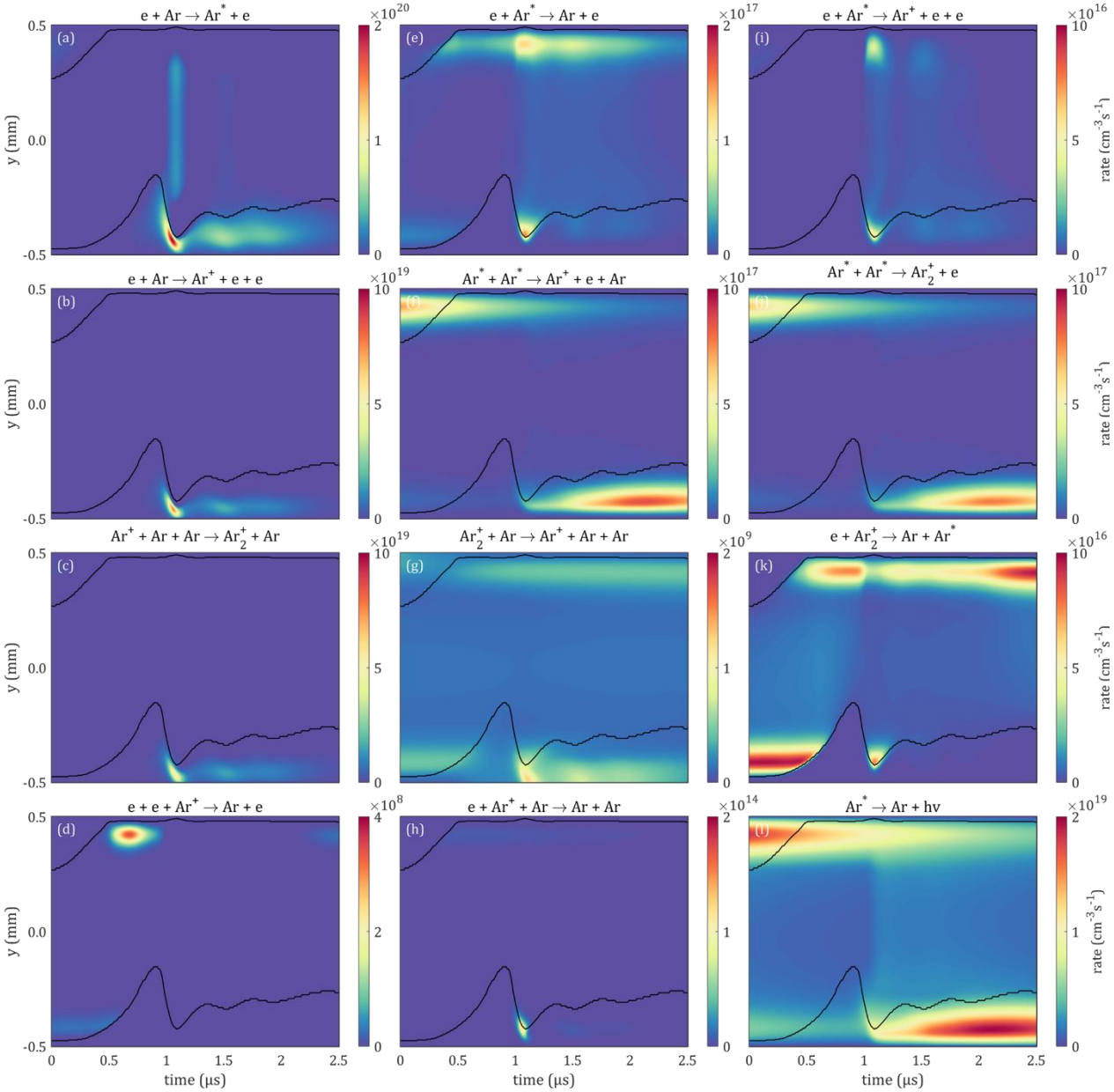


Figure 5.7. The spatial temporal reaction rate of all the reactions included in the model (table 3.2) during one half cycle (duration 2.5 μs – second half of the full cycle of Figure 5.1 and 5.2). Including the sheath edge drawn with a solid line.

### 5.1.5. Spatial averaged temporal rate contributions

To determine the actual importance of each reaction described in the model, the spatial averaged reaction rate contributions are given in Figure 5.9 (next page). All reactions are given for transparency.

Molecular to atomic ion conversion (5.9j) and the two three body recombination reactions (5.9k and 5.9f) can be neglected as the rate (Figure 5.7d, 5.7g and 5.7h) and rate contributions are very low.

The results of de-excitation (5.9g) is the destruction of one metastable and the production of one ground state atom. The latter is treated as a constant such that only the destruction is relevant. However this process is insignificant compared to radiative decay (5.9l) which is the main loss of metastables. This reaction can thus be neglected. Other metastables losses are the two metastable-metastable ionization processes (5.9c and 5.9i) and stepwise ionization (5.9b).

Stepwise ionization (5.9b) had a relatively low rate – (Figure 5.7) $O{\sim}10^{16}$ compared to $O{\sim}10^{19}$ $\mathrm{cm^{-3}s^{-1}}$ for direct ionization. The average contribution to both the electron and atomic ion production as well as the metastable loss is very low. This reaction could be neglected. However this ionization process took place in the positive column structures instead of being related to the negative glow and cathode fall only, see Figure 5.7. Section 5.2.1 considers the role of stepwise ionization in more detail.

Figure 5.8 shows the complementary ratio between the production and destruction of each species.

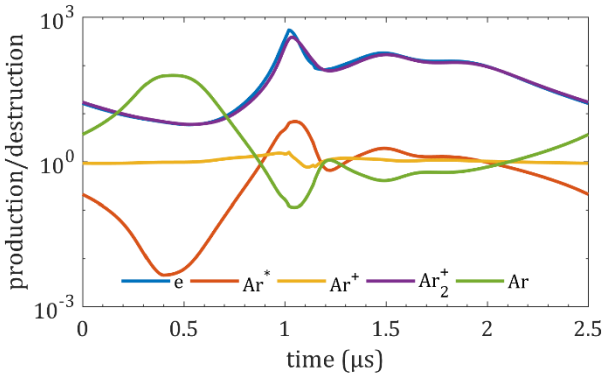


Figure 5.8. The production to destruction ratio of all the species taking part in the reactions (table 3.1) during one half cycle (duration 2.5 μs – second half of the full cycle of Figure 5.1 and 5.2).

Excitation (5.9a) is the main production of metastables during the discharge, dissociative recombination (5.9e) in other regions such as before the discharge and in the positive column (Figure 5.7) at a lower rate (5.7k compared to 5.7a). Effectively metastables are lost due to radiative decay (5.9l), which occurs in the whole volume.

Direct ionization (5.9h) is the main source of atomic ions. Metastable-metastable ionization produces the ion before the discharge (5.9c) at a lower rate. The latter also takes place in the positive column (Figure 5.7). Overall the average production to destruction ratio is near unity, indicating that conversion to the molecular ions (5.9d) – which is the only significant loss of the atomic ions – takes place immediately.

The molecular ions are formed due to conversion from atomic ions (5.9d). Before breakdown, metastable-metastable associative ionization (5.9j) also has a significant contribution. The latter is

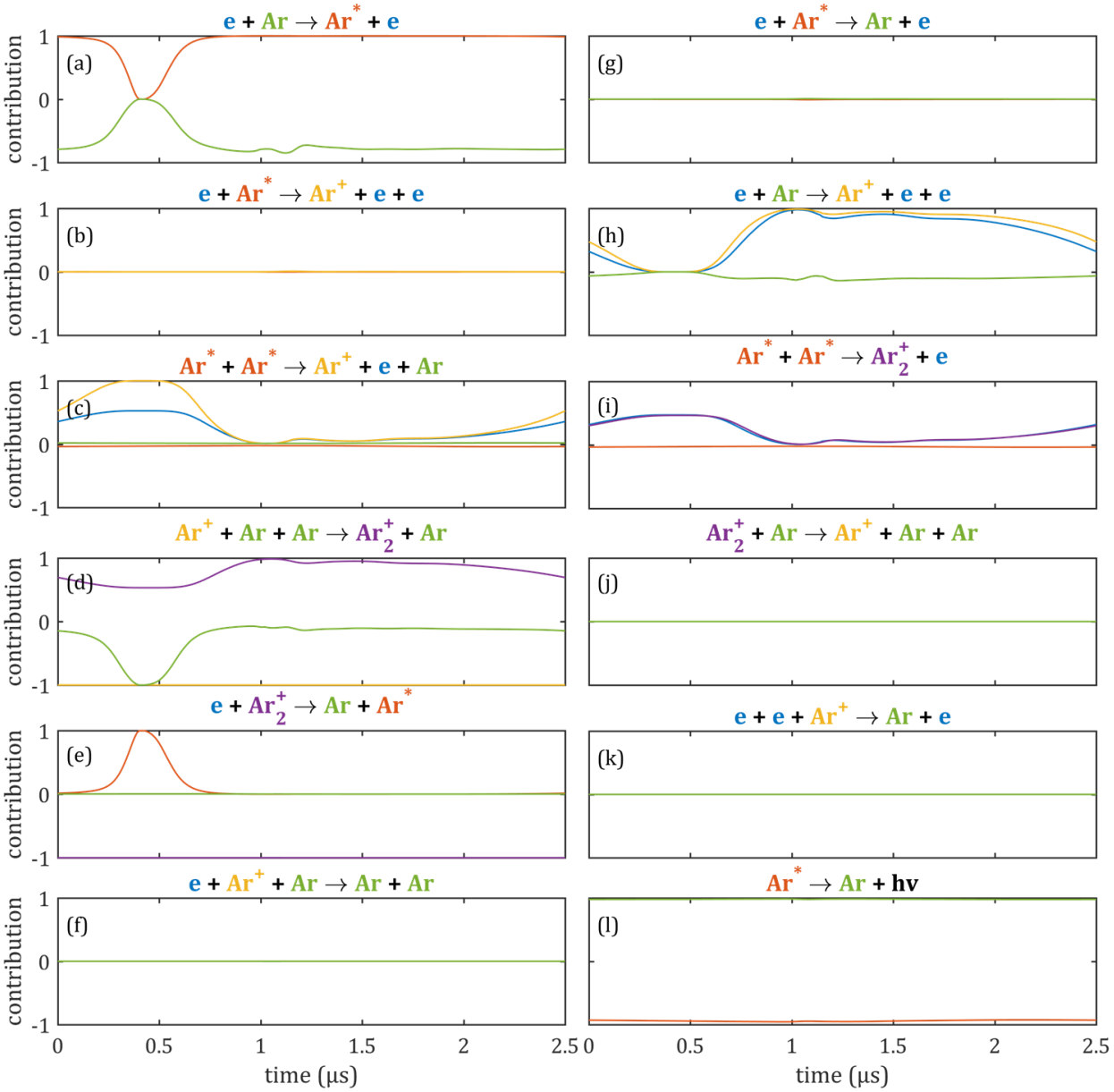


Figure 5.9. The spatial averaged temporal reaction rate contribution of all the reactions included in the model (table 3.2) during one half cycle (duration 2.5 μs – second half of the full cycle of Figure 5.1 and 5.2). The plotted colors correspond to the title colors. The lines may overlap. Axes normalized from -1 to +1.

less restricted to the negative glow only (Figure 5.7j compared to 5.7c). Overall the production is much higher than the destruction which is only due to dissociative recombination (5.9e), still a steady state plasma is reached. This reaction rate analysis does not take into account fluxes to the wall.

Electrons are created in any of the ionization processes. Direction ionization (5.9h) and both metastable-metastable ionization processes (5.9c and 5.9j) can be recognized as the main electron production during and before the breakdown respectively. The only significant loss is dissociative recombination (5.9e). The production to destruction ratio is high and like the molecular ions. This can be expected as any ionization produces one electron and any atomic ion ends up as the molecular ion, both of which are required for their own destruction. Dissociative recombination takes place mainly in the bulk while the production takes place mainly in the sheath areas (Figure 5.7k compared to 5.7c and 5.7j).

## 5.2. The main processes

In the following subsections the chemistry input of the model is modified to learn about the role of the various processes and their importance. Stepwise ionization and the branching of the metastable-metastable ionization into the regular and associative kind are considered separately.

As a side note, direct ionization was found a necessity to step into a discharge and consequently maintain the periodic breakdowns.

### 5.2.1. On stepwise ionization

Stepwise ionization was seen to have a lower rate than direct ionization. Those two processes do not take place in the same area. Stepwise ionization takes in in the positive column and other bulk areas whereas direct ionization does not, due to the difference in energy dependence.

Sobota et al. [24] considered the formation of a discharge in argon with and without any ionization processes involving metastables. The discharge formation was seen to behave differently and had been slowed down significantly. In this present section only stepwise ionization is excluded and the steady state discharge at the maximum negative glow electron density (see Figure 5.3) is discussed.

Figure 5.10 compares the original discharge, full model, to the same model with stepwise ionization removed, through the change in the density profiles that were presented in Figure 5.3.

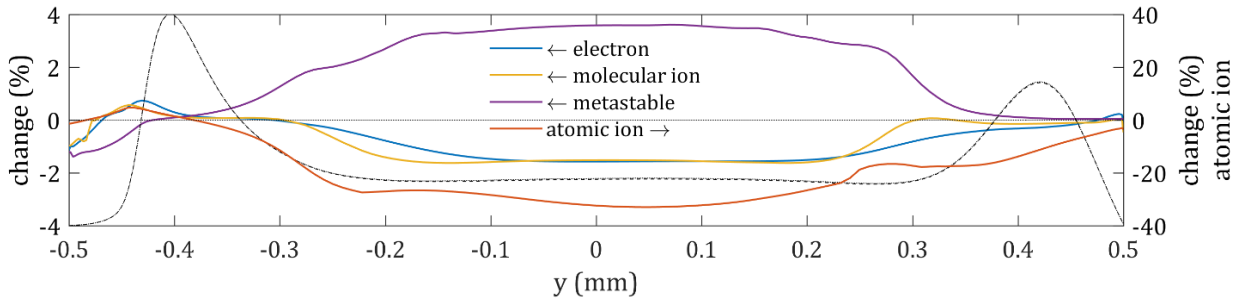


Figure 5.10. Change in the density profiles comparing the full chemistry input against a model without stepwise ionization. The atomic ion change is one order larger, displayed on the right axis. The electron density profile is included as background – arbitrary scale, dashed line, as a reference to the glow discharge structure. The instantaneous cathode is on the left. (Electron density profile of both models are plotted, indistinguishably overlapping each other.)

The profiles were extracted again at the maximum electron density in the first negative glow peak. Between the two models that are compared to each other, this moment in time did not change. In terms of absolute change; the electron and molecular ion density profiles changed 1 to 2%, the

metastables up to ~3%. The atomic ion density changed by approximately 40% at maximum. Figure 5.10 shows that those values mainly occur in the plasma bulk. The change in the positive column is less. The change in the negative glow is very small.

In the plasma bulk both ions as well as the electrons decreased. One ionization pathway is removed resulting in less for all of those species. Stepwise ionization can be assumed to contribute to ionization in the bulk by comparing the various ionization processes (Figure 5.7i to 5.7b, 5.7f and 5.7j) and considering the energy dependency (Figure 3.2a and Figure 5.6). This explains the large change in atomic ions in the bulk. Metastables were increased after removing stepwise ionization, it is no longer consumed for this reaction.

In general the atomic ion density is lower than the other species in the plasma. From Figure 5.3 the atomic ion density is found as approximately $10^8$ cm$^{-3}$ in the bulk area which is much smaller compared to $O{\sim}10^{12}$ cm$^{-3}$ for the electrons and main ions. Spatially averaged the atomic ion density is also approximately two orders lower. Because of this difference the changes up to 40% do not alter the discharge significantly.

Combining the above with the analysis of the actual rate – which is one order lower than other ionization mechanism from metastable states (Figure 5.7), stepwise ionization is found to be an insignificant contribution to the discharges under consideration.

### 5.2.2. On associative metastable-metastable ionization

Metastable-metastable ionization provides a path that produces either ion. The rate coefficients are constant and thus takes place over the whole discharge. The metastables are somewhat localized to the sheath regions (Figure 5.2) resulting in a reaction rate also mainly in the sheath, but lasting until the local formation of a positive column.

The retrieval of the rate coefficients (equation 3.1 and 3.2) for both metastable-metastable ionizations from literature was presented in section 3.2. The rate coefficients are related to each other through the branching factor $\beta$. This factor (0.9) was determined by Pavlík et al. [43], in the same publication this factor was varied to see the influence on their plasma (an argon flowing afterglow plasma). It was found to not influence the electron and metastables substantially. However it was noted that the branching factor does influence the ion composition in the afterglow plasma.

In general literature the associative kind is not necessarily considered [24], [25], [41], [54]. Regular metastable-metastable ionization is then considered only. The effective rate coefficient is still equal, thus two metastables still react equally, however the outcome is singular. Here the differences in including and not including the associative kind will be investigated for present conditions.

The discharge will be considered with and without the associative kind by setting the branching factor $\beta \equiv 0$ in equation 3.1 and 3.2. This effectively switches of associative ionization and attributes the full rate coefficient to the regular kind. By keeping the total rate coefficients constant, the electron production should still be equal as there is no change in the amount of ionization taking place. Atomic ion production should be higher throughout as it effectively gained an additional source term. Molecular ions are now created through atomic to molecular ion conversion only. Because the timescales of metastable-metastable ionization and subsequent conversion is not by definition the same as for direct associative ionization, the impact on the production of the molecular ion is not immediately clear.

To that end the population of the molecular ion is considered in isolation for a model with and without the associative ionization. For the latter, only the changes with respect to the full model are accounted for in this description. For the full model it follows:

$$\left.\frac{dn_{\mathrm{Ar}_2^+}}{dt}\right|_+ = k_{\mathrm{MMAI}} n_{\mathrm{Ar}^*}^2 + k_{\mathrm{AMC}} N^2 n_{\mathrm{Ar}^+} \tag{5.2}$$

The + subscript denotes production only, MMAI indicates the metastable-metastable associative ionization process and AMC the atomic to molecular ion conversion and $N$ is the background gas density. Figure 5.11a shows this schematically. Figure 5.11b shows the changes to this scheme due to the exclusion (or rather, treated as a redistribution) of associative ionization. The balance then reads:

$$\left.\frac{dn_{\mathrm{Ar}_2^+}}{dt}\right|_+ = k_{\mathrm{AMC}} N^2 n_{\mathrm{Ar}^+} + k_{\mathrm{AMC}} N^2 n'_{\mathrm{Ar}^+} \tag{5.3}$$

$$\frac{dn'_{\mathrm{Ar}^+}}{dt} = k_{\mathrm{MMAI}} n_{\mathrm{Ar}^*}^2 - k_{\mathrm{AMC}} N^2 n'_{\mathrm{Ar}^+} \tag{5.4}$$

Where $n'_{\mathrm{Ar}^+}$ is introduced as the extra atomic ion density due to the rate coefficient for metastable-metastable ionization being increased by $k_{\mathrm{MMAI}}$. From equation 5.3 and 5.4 follows:

$$n'_{\mathrm{Ar}^+} = \frac{k_{\mathrm{MMAI}} n_{\mathrm{Ar}^*}^2}{k_{\mathrm{AMC}} N^2} + n'_{\mathrm{Ar}^+,0} \exp(-k_{\mathrm{AMC}} N^2 t) \tag{5.5}$$

$$\left.\frac{dn_{\mathrm{Ar}_2^+}}{dt}\right|_+ = k_{\mathrm{MMAI}} n_{\mathrm{Ar}^*}^2 + k_{\mathrm{AMC}} N^2 n_{\mathrm{Ar}^+} + k_{\mathrm{AMC}} N^2 n'_{\mathrm{Ar}^+,0} \exp(-k_{\mathrm{AMC}} N^2 t) \tag{5.6}$$

Comparing equation 5.6 with 5.2 and not considering specific density locations; the first two terms are the same. In both equations, the term $k_{\mathrm{AMC}} N^2 n_{\mathrm{Ar}^+}$ dominates – under current conditions. Due to the reoccurrence of $-k_{\mathrm{AMC}} N^2$ in the exponent of the added term, in case of excluding associative ionization (equation 5.6), the extra term does not play a role. Both rate coefficients in the above are constant, and thus this equivalence should hold anywhere in and during the plasma. If $k_{\mathrm{AMC}} N^2$ would be very small, in both models $k_{\mathrm{MMAI}} n_{\mathrm{Ar}^*}^2$ would remain only, keeping the equivalence. If $n_{\mathrm{Ar}^+}$ is considered as more local than $n_{\mathrm{Ar}^*}$ (Figure 5.2), intermediate regimes were all terms play a role could then potentially be possible.

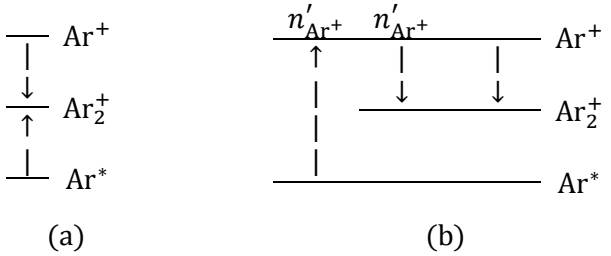


Figure 5.11. (a) Schematics representing the population of the molecular ion in the full model. (b) Illustrates the changes with respect to the full model for the model without associative ionization. The symbol $n'_{\mathrm{Ar}^+}$ is introduced as the extra population of the atomic ion due to the increased rate coefficient.

The electrons and molecular ions (and consequently the metastables) were argued to not change due to the exclusion of associative ionization. The atomic ions should increase. Comparing the full model to a model without associative ionization during a steady state half cycle results in a change of $\pm 3\%$ for the electrons, less than $\pm 1\%$ for the metastables, the atomic ion nearly doubled in the bulk ($+92\%$) and increased throughout (however $-2\%$ was observed locally) shown in Figure 5.12a. The molecular ion stayed constant in the bulk (maximum was less than $+1\%$) but decreased 3% in the sheath areas, after the breakdown as shown in Figure 5.12b. The small changes of up to 3% are judged as insignificant, thus judging that the outcome of the comparison is after the expectations. The inclusion of metastable-metastable associative ionization is not necessarily as long as the total rate coefficients stays equal. This allows the chemistry description to be reduced by one reaction. Chapter 6 considers the metastable-metastable ionization process through changes in the total rate coefficient.

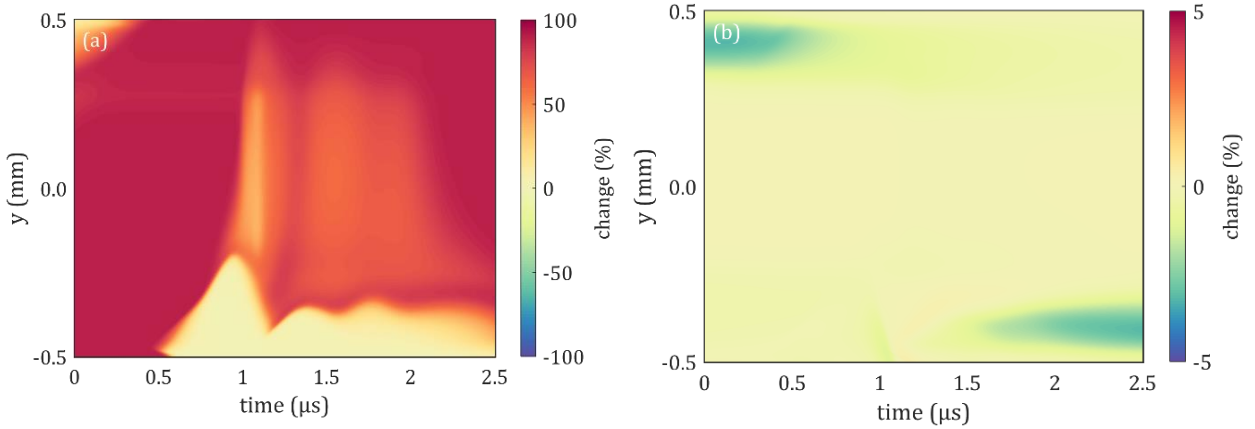


Figure 5.12. Change in spatial temporal densities of atomic ions (a) and molecular ions (b). Comparing a model without metastable-metastable associative ionization to the full model. Shown during one half cycle (duration 2.5 μs – second half of the full cycle of Figure 5.1 and 5.2).

### 5.2.3. The essential argon chemistry scheme

The full description of the argon reduced chemistry scheme involved 12 reaction (Table 3.2). Section 5.1.4 showed that the two three body recombination reactions could be neglected, such that 10 reactions remain. Similarly, molecular to atomic ion conversion was argued to be negligible, leaving 9 reactions. Section 5.1.4 also argued that neglecting de-excitation does not influence the discharge, resulting in 8 reactions down from 12.

Section 5.2.1 discussed the role of stepwise ionization. Despite being localized relatively uniquely in the discharge compared to the other ionization mechanisms, it was shown that excluding it did not have a significant impact on the discharge under current conditions. This exclusion would allow the chemistry to be described by 7 reactions.

Section 5.2.2 discussed the role of regular and associative metastable-metastable ionization and discussed the implications of accounting only for atomic ion creation through this process by keeping the total rate coefficient constant. This was shown to not have a major influence on the discharge behavior due to fast atomic to molecular ion conversion. Using this, the chemistry scheme can be chosen to be reduced down to 6 reactions.

Dissociative recombination was not yet discussed in detail specifically. It is the only (significant) loss for electrons and molecular ions and takes place mainly in low energy areas. Golubovskii et al. [17]

considered dissociative recombination especially, in an atmospheric helium barrier discharge. They observed dynamic behavior, by varying the rate coefficient, through asymmetry between positive and negative half cycles of the discharge. They reported that for slow recombination the discharge was asymmetric because the quasi neutral plasma bulk does not get destroyed significantly within one half cycle, causing the next breakdown to be much weaker during which the bulk is again destroyed, now almost completely [17]. For fast recombination (approximately a factor 100 higher) this asymmetry was lost. In present study in argon, no similar asymmetry is observed, such that in analogy to Golubovskii et al. [17], the dissociative recombination in argon can be considered fast. However decreasing the rate coefficient by a factor 10 and 100 did not result in asymmetric behavior in argon under current conditions. Instead it took longer to reach a steady state. This was also true for excluding dissociative recombination completely (approximately 4 times longer). The point at which the breakdown occurred was left unchanged. Figure 5.9 showed that the production to destruction ratio for the electrons and molecular ions was $\sim 10^2$. Because of this it is assumed that the electrons and main ions loss to the wall (anode and cathode respectively) is also an important contributor to reaching a steady state, and indeed able to govern a steady state.

In looking for the extreme, the argon chemistry scheme could potentially be reduced to 5 reactions by also excluding dissociative recombination. The reduction down to 6 reactions is still judged physical. The reduction down to 7 reactions (including stepwise ionization) is assumed to cover a wider range of discharges. In this latter scheme only processes with a very low rate and thus a very low rate contribution have been removed as well as simplifying the metastable-metastable ionization processes.

Table 5.1 gives an overview of those reductions. Figure 5.13 compares the individual species densities along the discharge profile as found at the maximum electron density in the first NG peak.

Table 5.1. Summary of the discussed reductions to the argon chemistry scheme.

| | | | | Reaction set | | | | |
|---|---|---|---|---|---|---|---|---|
| R# | Reaction | | | Full | 8R | 7R | 6R | 5R |
| 1 | $e + Ar$ | $\rightarrow$ | $Ar^* + e$ | × | × | × | × | × |
| 2 | $e + Ar^*$ | $\rightarrow$ | $Ar + e$ | × | | | | |
| 3 | $e + Ar^*$ | $\rightarrow$ | $Ar^+ + e + e$ | × | × | × | | |
| 4 | $e + Ar$ | $\rightarrow$ | $Ar^+ + e + e$ | × | × | × | × | × |
| 5 | $Ar^* + Ar^*$ | $\rightarrow$ | $Ar^+ + e + Ar$ | × | × | × | × | × |
| 6 | $Ar^* + Ar^*$ | $\rightarrow$ | $Ar_2^+ + e$ | × | × | | | |
| 7 | $Ar^+ + Ar + Ar$ | $\rightarrow$ | $Ar_2^+ + Ar$ | × | × | × | × | × |
| 8 | $Ar_2^+ + Ar$ | $\rightarrow$ | $Ar^+ + Ar + Ar$ | × | | | | |
| 9 | $e + Ar_2^+$ | $\rightarrow$ | $Ar^* + Ar$ | × | × | × | × | |
| 10 | $e + Ar^+ + e$ | $\rightarrow$ | $Ar + e$ | × | | | | |
| 11 | $e + Ar^+ + Ar$ | $\rightarrow$ | $Ar + Ar$ | × | | | | |
| 12 | $Ar^*$ | $\rightarrow$ | $Ar + h\nu$ | × | × | × | × | × |

Figure 5.13 shows that the reduction down to 6 reactions gives a results consistent with the full scheme. Removing dissociative recombination does alter the discharge slightly. The set involving 6 instead of 12 reactions is actually used in 2D modelling to save on computational time. Figure 5.14 compares the spatial averaged density evolution of the full model with a model using the 6 reactions only, including a first breakdown by initializing the model with very low densities (Table 3.1). It is shown that no small details are lost. The difference for the metastables, electrons and molecular ions

is insignificant. The atomic ion density is observed to be higher before the breakdown in the reduced model. This is attributed to the exclusion of associative metastable-metastable ionization, see section 5.2.2 and Figure 5.12. Based on Figure 5.14, the aforementioned approach, running the 2D models with this reduced set of reactions, is judged as valid even though those models will be initialized with low densities to ensure proper breakdown and plasma expansion. Chapter 10 reports on the 2D modelling results.

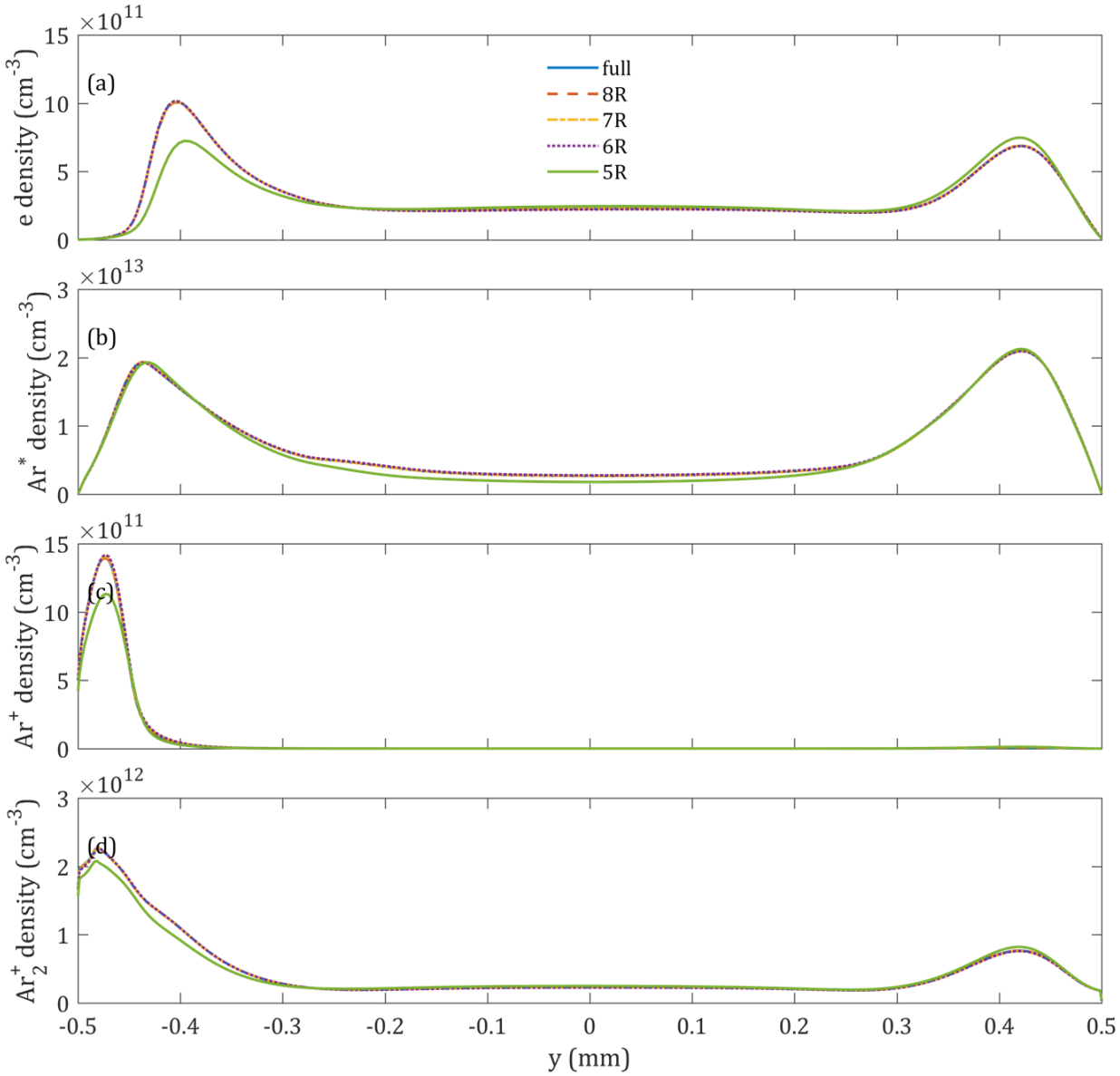


Figure 5.13. The density profiles of (a) electrons (b) metastables (c) atomic ions and (d) molecular ions along the gas gap at the maximum electron density in a negative glow peak, comparing different argon chemistry schemes with amounts of reactions (table 5.1).

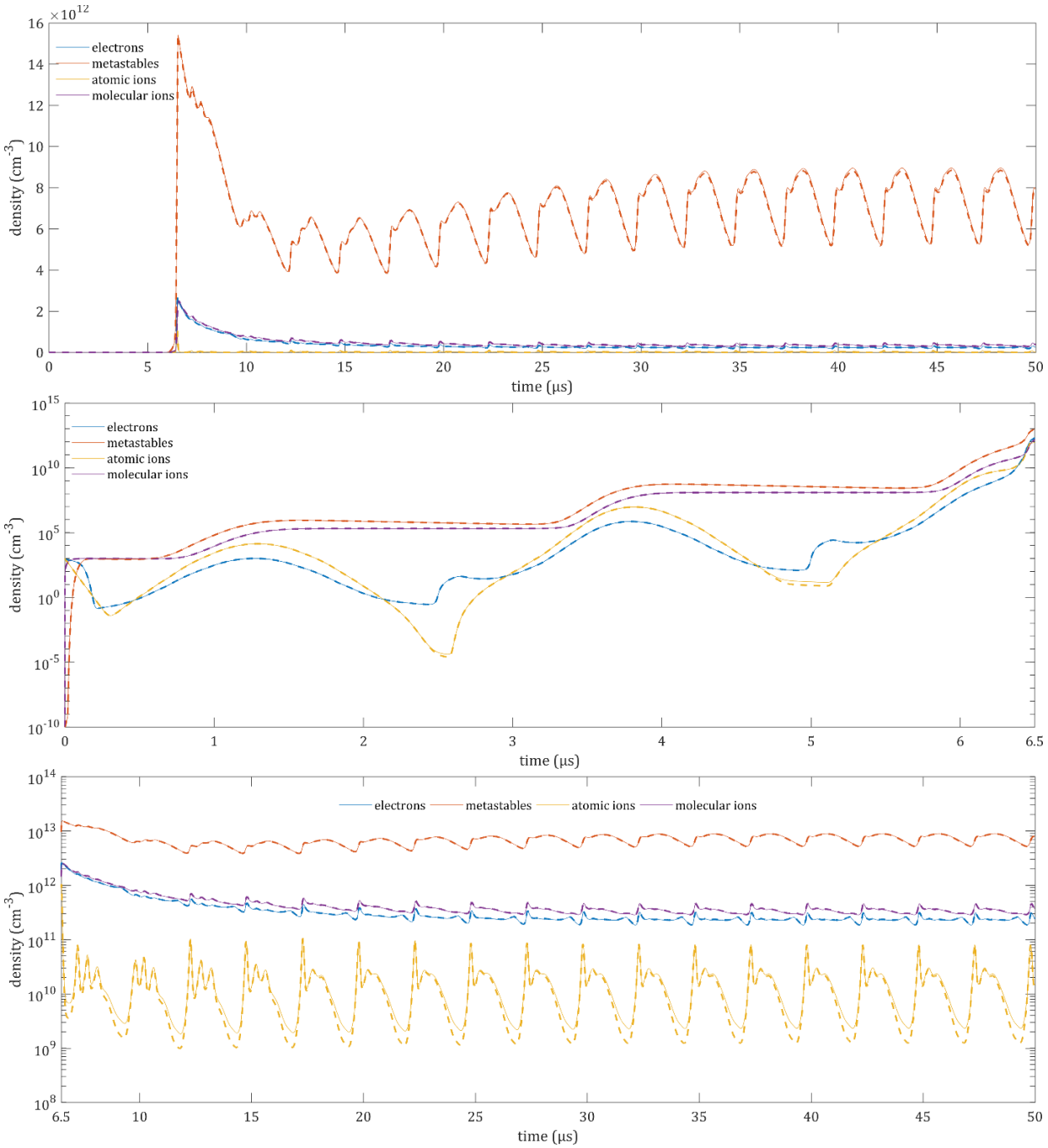


Figure 5.14. Spatial averaged density evolution. Comparison between the full model (dotted lines) and a model reduced to 6 reactions (solid lines) – see table 5.1, including a first breakdown through model initialization with low densities. The full run on a linear scale (top), the evolution during multiple voltage half cycles up to and until the first breakdown on a logarithmic scale (middle) and the remainder of the simulation run on a logarithmic scale (bottom) is shown.

## 5.3. Conclusions

A single atmospheric pressure argon DBD was reported in detail. The discharge was found to be glow-like, featuring a cathode fall, negative glow, faraday dark space, positive column and anode dark space. The specific conditions used resulted in (small) multi peak behavior during a single half cycle. Three body recombination reactions and molecular to atomic ion conversion were found to be negligible due to very low rates and rate contributions. De-excitation was argued to be negligible because the metastables were predominantly destroyed through radiative decay. Exclusion of stepwise ionization has shown that it mainly affects the atomic ion density in the plasma bulk. It did not change the discharge noticeably due to the very low density. Regular and associative metastable-metastable ionization were included in the plasma chemistry input. The use of only the regular kind with an equal total rate coefficient for metastable-metastable ionization was considered. Other than increasing the atomic ion density in low energy areas, it was found to not influence the plasma significantly under current conditions. Eventually a chemistry model considering down to six reactions was found to yield results consistent with the full model. This was true even when a first breakdown was considered by initializing the models with low densities. The reduced model includes excitation, direct ionization and (regular) metastable-metastable ionization, atomic to molecular ion conversion, dissociative recombination and radiative decay.

Dissociative recombination is the main loss of electrons and molecular ions, considering the chemistry reactions. It can be considered a fast reaction. It was shown that without this mechanic a steady state was reached on larger time scales. This was attributed to the electron and ion fluxes to the anode and cathode respectively.

# 6. Multi-peak discharge behavior and metastable-metastable ionization


## Abstract

In one-dimensional modelling a steady state glow-like atmospheric pressure argon dielectric barrier discharge is achieved. A pronounced positive column and negative glow region are found. The discharge shows multi-peak behavior within a half cycle. By manipulating the rate coefficient in metastable-metastable ionization in various artificial plasma models, the role of this process in the formation of the positive column and consequently the role of the positive column in this argon discharge is elaborated upon.


## 6.1. Multi-peak discharges in literature

Li et al. experimentally found a multi-peak discharge in argon by saw-tooth (~sinusoidal for higher frequencies) voltage excitation in a specific frequency range. Increasing the frequency from this multi-peak regime decreased the amount of peaks and their intensity. A multi-peak Townsend discharge was noted to appear if the secondary electron emission was dominated by emission through ions [55]. Supplementary modelling studies in argon showed [25] showed a frequency range under which the multi-peak behavior occurred for the saw-tooth applied voltage.

Sublet et al. experimentally observed a multi-peak mode in helium at atmospheric pressure by increasing the applied voltage. The name multi-glow mode was suggested. Each pulse was reported to start in a non-self-sustained regime, going into a Townsend discharge and ending in a subnormal glow. The gas voltage decreases during the latter, corresponding to the current peak maxima [56].

Golubovskii and coworkers [17], [23] performed modelling studies on atmospheric pressure homogenous dielectric barrier discharges in helium [17] and nitrogen [23]. Multi-peak behavior was observed in Townsend regimes. Those were attributed to a lag time between the production of ions and resonance atoms at the anode and subsequent electron emission at the cathode. Their observed glow discharges were specified by single peak behavior. Other mechanisms behind the formation of multiple current peaks during a single half cycle were mentioned. A lag time due to photoemission, which should cause relatively more frequent peaks. Multi-peaks due to volume charge was also mentioned and noted to be able to cause multi-peaks without secondary electron emission processes [17].

Petrovic et al. [18] also observed multi-peak discharges in the Townsend regime in helium over a wide voltage range and low frequency range. It was noted that accumulated charge on the dielectric increases with applied voltage, allowing memory voltage to enhance the external voltage, allowing the breakdown voltage to be exceeded again after a current is quenched. Decreasing amplitude of subsequent current peaks is explained by the memory voltage caused by the accumulated charge which weakens the electric field in later stages of the discharge [18].

Radu et al. [19] studied multi-peak discharges in helium in detail by also considering the individual peaks, however a metallic-dielectric electrode setup was used. Pseudoglow and glow discharge were found. In the psuedoglow regime the amount of current peaks reduced with increasing frequency and increased with increasing voltage. Reducing rise time in latter current peaks and the monotonically decrease of their amplitude was attributed to the prevalence of Penning ionization during later peaks compared to the first peak where the change in polarity greatly reduced the concentration of the species initiating Penning ionization. It was noted that the distinguishing feature of a glow discharge

compared to the psuedoglow discharge is that no additional current peaks are formed by increasing the voltage [19].

In this present study, the influence of metastable-metastable ionization on the discharge is considered and subsequently the discharge characteristics and multiple pulses therein. This is done by considering some parametric variations in the rate coefficient of this process.

## 6.2. Effects of varying the metastable-metastable ionization rate coefficient

The main discharge conditions under consideration is identical to the case used in chapter 5, as reiterated here. The background gas temperature is 450 K, the pressure is 1 atm, the dielectric thickness is 0.1 mm, the dielectric constant is 3.4 and the gas gap is 1 mm. The applied voltage is sinusoidal with an amplitude of 1 kV at a frequency of 200 kHz. The secondary electron emission coefficient for all non-constant argon species is set to 0.1. The full chemistry set is used (Table 3.2) and any (further) mentions of metastable-metastable ionization in this chapter refers to both the regular and associative kind. Variations in applied voltage are always indicated.

Metastable-metastable ionization is turned off gradually by defining the factor $\alpha(\%)$:

$$k_r' = \frac{\alpha}{100\%} k_r \tag{6.1}$$

where $k_r$ represents the rate coefficients of metastable-metastable ionization. The prime indicates the adjusted rate coefficient used in this section.

Figure 6.1a compares the plasma current characteristics for decreasing rate coefficients. The multi-peak characteristics are seen to systematically reduce to a smooth current shoulder after the first peak for the case of no metastable-metastable ionization. The first current peak increases with decreasing rate coefficient and the first peak occurs later. Similarly the rate coefficient was increased, to verify that the multi-peak behavior would be enhanced. This is shown in Figure 6.1b, where the trend is indeed consistent with Figure 6.1a. The secondary peaks become more pronounced, the first peak decreases in amplitude and occurs earlier.

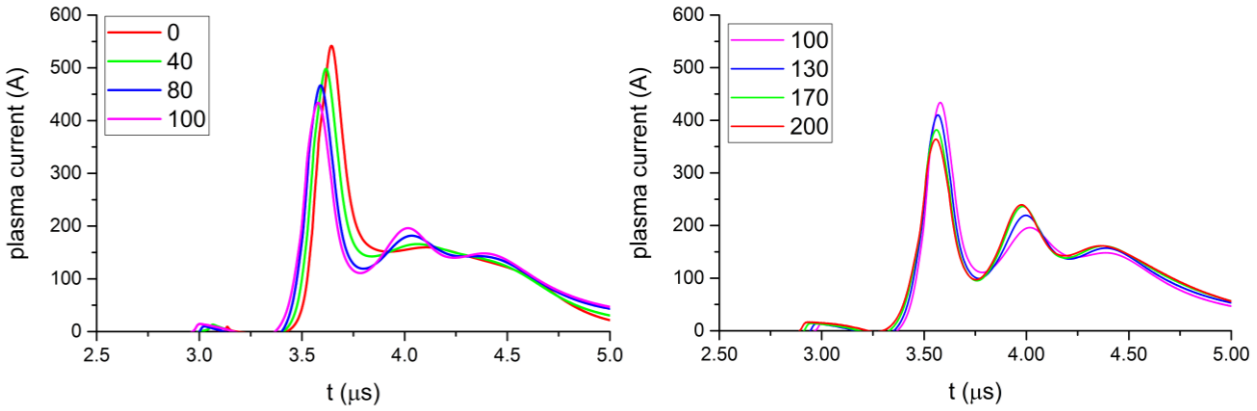


Figure 6.1. The plasma current for various $\alpha$ (%) (legend) during one voltage half cycle, gradually turning off metastable-metastable ionization processes (a) and gradually increasing the rate coefficient (b) (see equation 6.1).

Figure 6.1a showed that excluding metastable-metastable ionization results in different discharge behavior however it is no outlying case (it is reached systematically by reducing the rate coefficient to zero). Figures 6.2 compares a model with metastable-metastable ionization to a model without

over a wide range of applied voltages, to determine whether a multi-peak regime is achieved elsewhere. It is shown that the modified model does not reach a multi-peak behavior at high applied voltages, instead only a broad shoulder occurs.

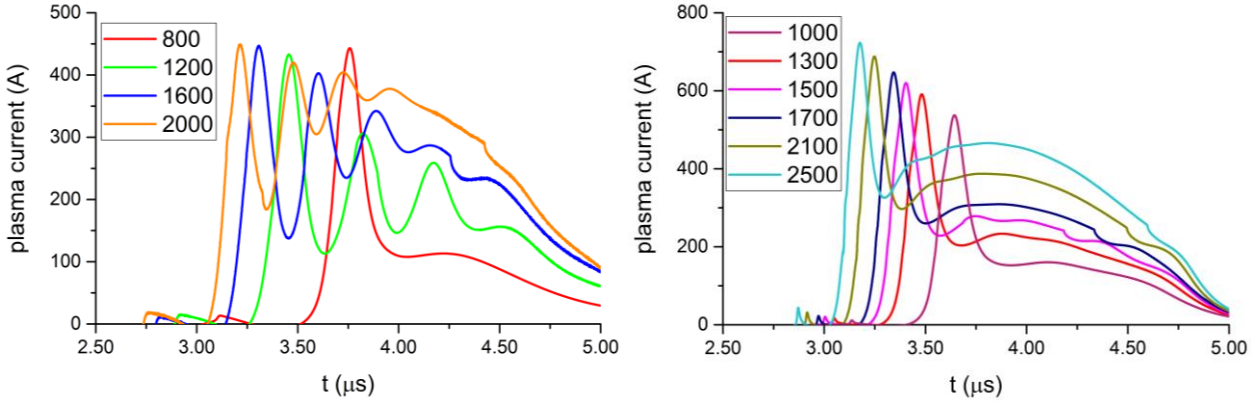


Figure 6.2. The plasma current for various applied voltages (V) (legend) during one half cycle, for the full model (a) and the model without metastable-metastable ionization (b).

Figure 6.3 compares the discharge with and without metastable-metastable ionization to each other through the current and voltage characteristic as well as the spatial temporal electron densities where the sheath edge (equation 5.1) is included. It is clearly shown through the electron density that both the multi-peak discharge behavior and the pronounced positive column have disappeared.

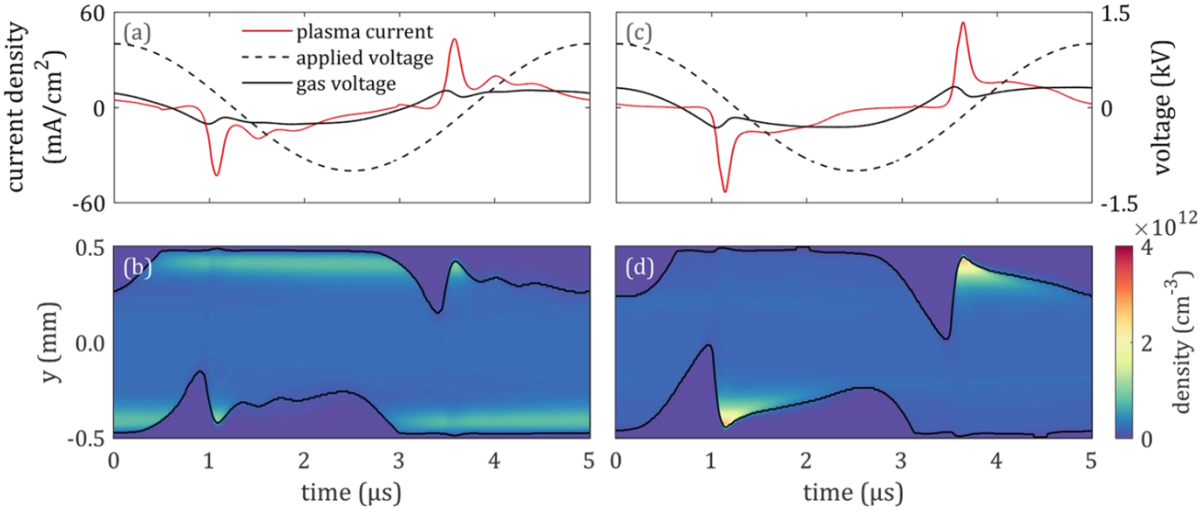


Figure 6.3. Comparison of the plasma structure between the full model (left) and the model without any metastable-metastable ionization (right), during one voltage cycle. Showing the IV characteristics (top) and the electron density (bottom).

## 6.3. Spatial and temporal steps in the metastable-metastable ionization rate coefficient

In section 6.2 metastable-metastable ionization was shown to cause the multi peak behavior. Up till now if steady state multi-peak behavior was presented, a positive column was also present. Figure 6.3d shows no multi-peak behavior and no positive column. In other modelling that yielded no multi-peaks – i.e. through different treatment of secondary electron emission or low applied voltages – a positive column was not present either. To gain more insight into the relation between the positive column and multi-peak discharge, three artificial model types involving a step (e.g. off to on) in metastable-metastable ionization (MMI) rate coefficient are introduced:

1) The full model with a spatial step. Turning MMI off in the positive side of the model.
2) The full model with a temporal step. Turning MMI off after a steady state breakdown with multi-peak characteristics.
3) The full model without MII with a temporal step. Turning MMI on after a steady state breakdown with single peak characteristics.

For the model of type 1), the rate coefficient was multiplied by the step

$$\frac{1}{1+\exp(y\cdot 10^5)}, \qquad -0.5\cdot 10^{-3} < y < +0.5\cdot 10^{-3} \tag{6.1}$$

The grid resolved this step smoothly. A steady state (with a period now equal to the applied voltage) was achieved despite the odd model configuration. Figure 6.4 shows the electron density during two periods (4 discharges). Here a positive column and a single negative glow peak as well as a negative glow with multi-peaks without a simultaneous positive column at the instantaneous anode were found together. Both the positive column and negative glow are observed in the region where metastable-metastable ionization is active only. Figure 6.5 compares the total current of this model to the full model and the model without metastable-metastable ionization. Good agreements are shown considering that the plasma is modified in an artificial way, which includes the bulk. In this specific case the secondary current peak was found to overlap completely (first and third breakdown).

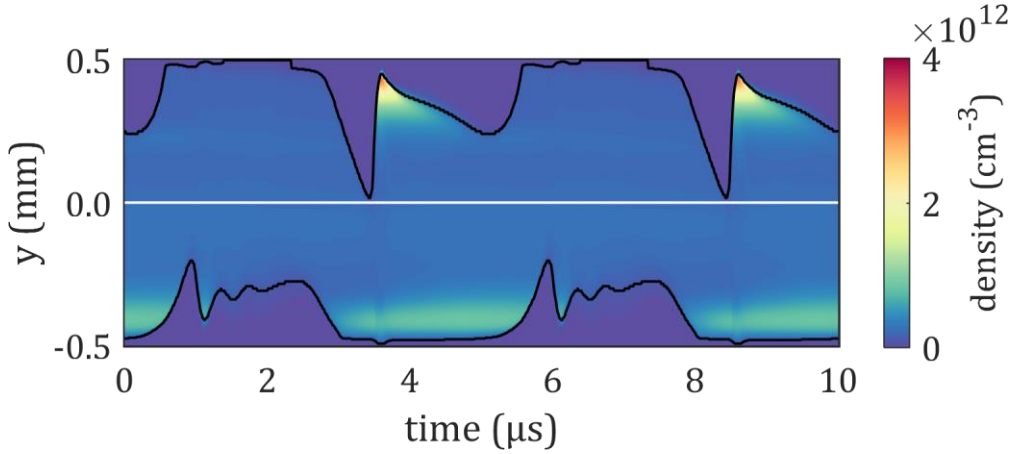


Figure 6.4. The electron density during two voltage cycles for an artificial plasma model without metastable-metastable ionization in the positive half of $y$.

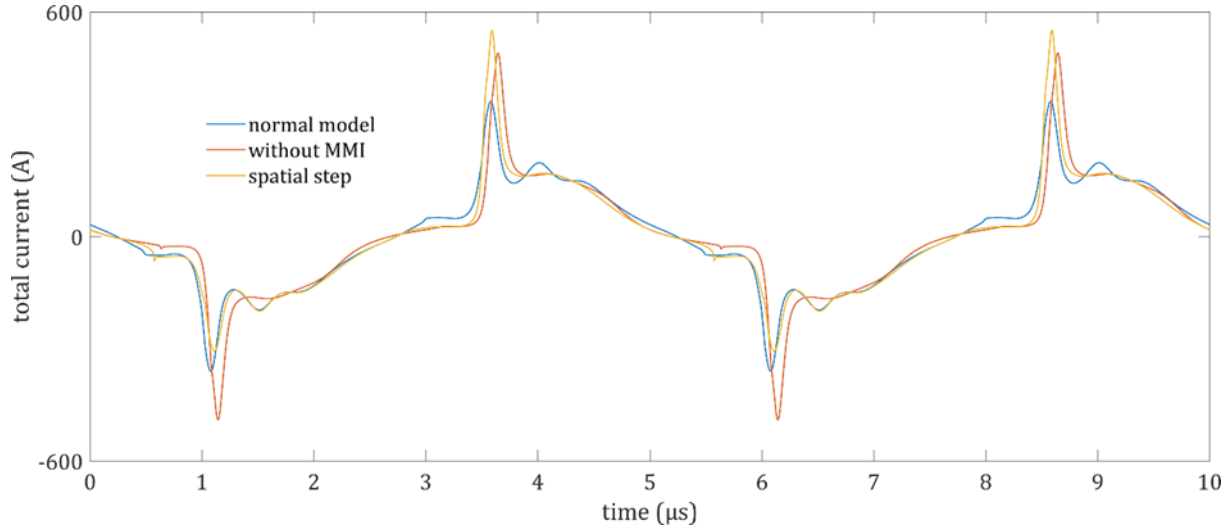


Figure 6.5. The total modelled current during two voltage cycles. Comparing the full, normal model with multi peak characteristics throughout, the same model without metastable-metastable ionization with smooth current characteristics throughout and the model with metastable-metastable ionization active only in the negative spatial half of the plasma (corresponding to the negative current breakdowns) showing alternating multi-peak and smooth characteristics.

For the model of type 2), the rate coefficient was turned off during $t \geq t_0$, $t_0$ was chosen at the onset of a steady state breakdown – corresponding to the point where the calculated sheath edge separates from the previous instantaneous anode. Figure 6.6 shows the electron density during two breakdowns before and several after this time instant. The negative glow immediately after the white line is of interest. Here in a breakdown without metastable-metastable ionization, but still preceded by a positive column, a multi peak characteristic is seen. Comparing the positive column during this breakdown itself; it is less pronounced compared to the previous breakdowns.

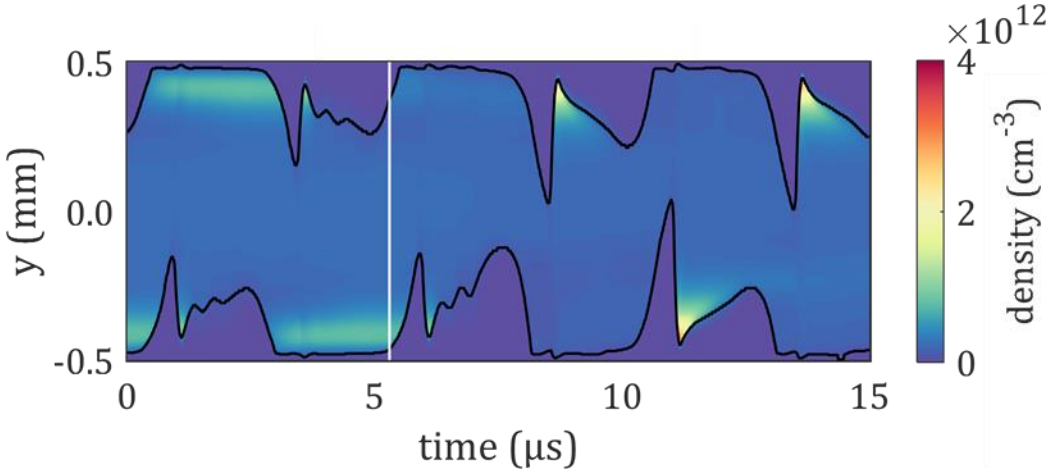


Figure 6.6. The electron density for an artificial model in which the metastable-metastable ionization processes are turned off after a steady state breakdown (white line).

For the model of type 3), the rate coefficient of metastable-metastable ionization was turned on for $t \geq t_0$. Figure 6.7 shows the electron density during two breakdowns before and a few breakdowns after turning on metastable-metastable ionization. The negative glow immediately after the white line is not preceded by a positive column and still shows a single peak characteristics despite metastable-metastable ionization taking place. The latter breakdown gradually develop a multi-peak behavior. The positive column during those breakdowns also grows in magnitude.

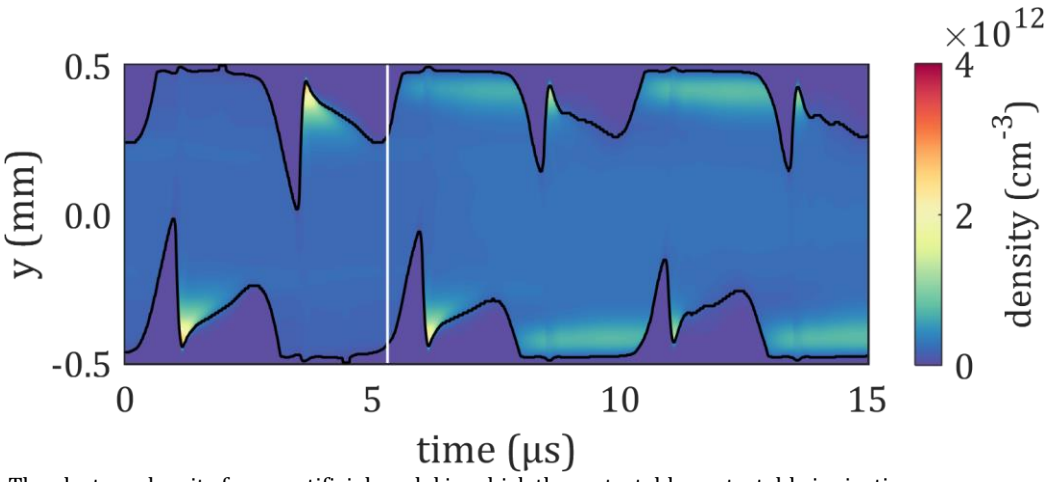

Figure 6.7. The electron density for an artificial model in which the metastable-metastable ionization processes were turned off and are turned on after a steady state breakdown (white line).

Based on those three models it is found that metastables-metastable ionization creates the positive column and that the positive column rather than metastable-metastable ionization itself causes the multi-peak behavior in the next half cycle. The first model (Figure 6.4) can be considered to reveal that secondary peaks are not related to ionization events taking place at the instantaneous anode of the same half cycle, as the lack of the positive column indicates the lack a significant ionization process there. The second model (Figure 6.6) is the only model that showed that the multi-peak behavior does not require metastable-metastable ionization in the negative glow area itself. The third model (Figure 6.7) can be considered to be the least artificial by realizing that the model ends in a steady state of the full model and that the initialization (at the step, $t = t_0$) was very close to the eventual plasma. This model also showed that the more pronounced the positive column, the more pronounced the multi-peaks.

Because of the above the multi-peak behavior is attributed to the memory effects of surface charge on the dielectric and thought of as analogous to the multi-peaks in literature attributed to Penning ionization processes in the preceding breakdowns.

## 6.4. Conclusion

Metastable-metastable ionization was found to be responsible for the formation of a positive column which in turn leads to the multi-peak discharge characteristics. It was found that a positive column and consequently significant ionization near the instantaneous anode was not a requirement within the same half cycle for the multi-peak behavior. In addition it was found that metastable-metastable ionization was not required locally at the negative glow regions for a multi-peak discharge.

From the above, the multi-peak discharge is attributed to the reduced external breakdown voltage due to the presence of the positive column in preceding breakdowns, causing memory charge on the dielectric, and a subsequent (after the initial breakdown) ability of the gas voltage to again rise above the breakdown voltage.

# 7. Overview of the current characteristics and breakdown mechanisms in atmospheric pressure argon


## Abstract

The full time domain, including periods preceding the steady state discharge, is considered in one-dimensional drift-diffusion modelling results of an atmospheric pressure argon dielectric barrier discharge. This includes a first breakdown by initializing the model with low particle densities. The breakdown mechanisms for the first breakdown and breakdowns in steady state are observed as different from each other. The former is identified as a Townsend breakdown while the latter discharges never lose their full glow-like characteristics.


## 7.1. Introduction

In essence, up till now only the steady state dielectric barrier discharge has been discussed. Section 5.2.3 did report the averaged species densities while considering a first breakdown (Figure 5.14) to confirm that a reduced chemistry model captured all the discharge characteristics even when considering a first breakdown. In this chapter the current characteristics and electron density of the same (full) model, including a first breakdown, will be briefly discussed in relation to reported observations in literature.

Gouda and Massines [20] experimentally investigated an atmospheric pressure dielectric barrier discharge in helium. Three different discharge types initiated by three different types of breakdown were reported. A glow discharge preceded by a Townsend breakdown, a filamentary discharge preceded by streamer breakdown and a homogeneous discharge preceded by streamer overlapping. In the glow discharge an *inverse current peak* [20] (or *residual current peak* [25]) is observed when the polarity of the (gas) voltage changes due to the acceleration of electrons towards the new instantaneous anode which were previously trapped in the positive column [20]. With short exposure time photographs it was shown that for the glow discharge light is observed near the anode before the current peak maximum, in latter stages the light localizes at the cathode and finally a positive column appears [20]. The homogeneous discharge, noted a transition discharge as it occurs between the filamentary and glow discharge (in helium), is reported to not rely on a memory effect (i.e. there was no light emission near the anode long before the current maximum was observed). The light intensity near the anode is reported to increase a lot, after which it crosses to the cathode similar to a glow discharge. Current maximums represent the glow discharge structure. The current reported for this transition discharge was 2-3 times higher than reported for the glow discharge. Later Massines et al. [21] reported current characteristics for first breakdowns which eventually reach a steady state Townsend or glow discharge. Any discharge is noted to require multiple half cycles to reach a reproducible one. The reported glow discharge exhibited high current compared to the Townsend discharge and the filamentary regime preceding it, however the first current amplitude was relatively low. During the second breakdown the current reached a maximum and subsequent discharges led to the steady state by again decreasing the current over several half cycles [21]. Martens et al. [57] reported based on modelling that the (steady state) glow discharges are preceded by a discharge that looks like a Townsend discharge but are actually more accurately described by a subnormal glow discharge as the electric field is not uniform before the actual glow formation. There [57] the discharge is assumed to never extinguish further than the subnormal glow discharge.

The above work is not performed specifically for argon dielectric barrier discharges. However some analogies are observed in present study. Here the current characteristics, electric field and various

species densities will be considered where appropriate. The model under investigation is the main model from previous chapters, reiterated here. The (background) gas temperature is 450 K and the pressure is 1 atm. The dielectric is 0.1 mm thick with a dielectric constant of 3.4. The gas gap is 1 mm. The applied voltage is sinusoidal with an amplitude of 1 kV at a frequency of 200 kHz. The secondary electron emission coefficients are set to 0.1. The model is initialized with very low densities (Table 3.1).

## 7.2. Modelling results: the breakdown mechanisms in argon

Figure 7.1 shows the current characteristics, electric field and electron and main ion density for the first breakdown. It is seen that it takes a few half cycles before the first breakdown occurs. The electric field is uniform up to that point. Upon breakdown, electrons are accelerated towards the anode and the electron density increases rapidly towards the instantaneous anode, causing a large current peak. Before this breakdown the electric field was very low and uniform as there was no significant volume charge in the discharge gap. The electrons at the anode do ionize and excite the argon atoms. During the same half cycle, at the instantaneous cathode a structure similar to the steady state negative glow with multi peaks is already observed. Chapter 6 investigated the multi peaks in relation to metastable-metastable ionization and the positive column in steady state discharges. There, through the introduction of three artificial plasma models, it was found that within one half cycle the multi peaks were not related to the positive column and that the multi peaks were also not related to (metastable-metastable) ionization at the instant of the negative glow itself. Instead the presence of the positive column in the preceding breakdown was found necessarily for the multi peak behavior. Here however, for the first breakdown, it is found that this does not hold. A multi peak negative glow is seen without preceding memory charge. Assuming that also here the (metastable-metastable) ionization around the negative glow itself does not cause the multi peaks, then only the instantaneous anode during the same half cycle is left as a cause even though this is in slight contrast with chapter 6. Here, during the first breakdown however, the densities are much higher and the negative glow currents are relatively low (see also later Figure 7.2).

Based on the uniform electric field before the first breakdown the first breakdown is judged as a Townsend breakdown from which quickly a glow-like discharge is formed which, through the notation of the lack of memory charge, can partly be considered analogous to the transition discharge described by Gouda and Massines [20]. The multi peak behavior here can be attributed to the high densities at the anode.

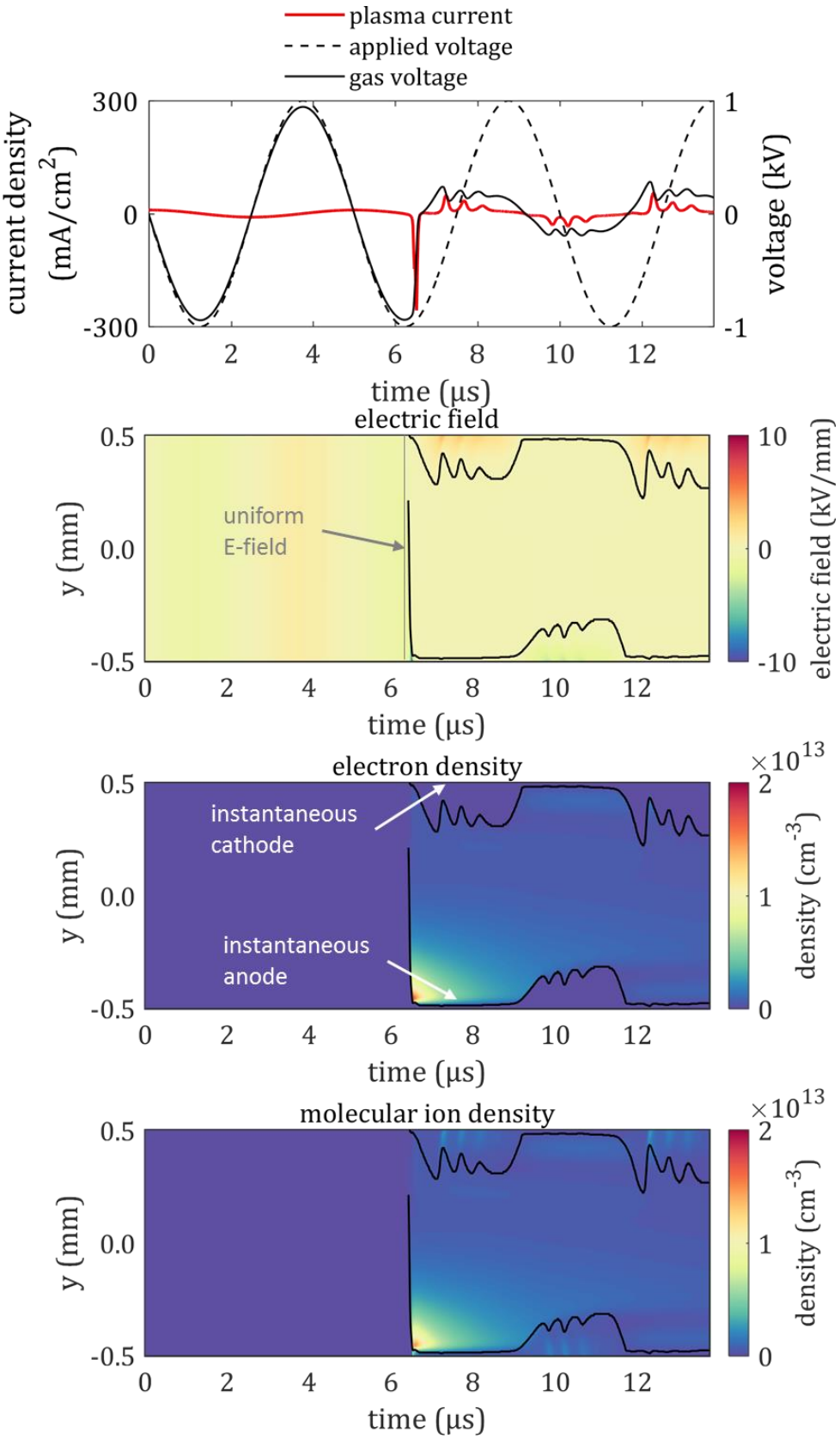


Figure 7.1. The current characteristics, electric field and electron and molecular ion densities during a first breakdown. The sheath edge calculation is also used (equation 5.1).

Figure 7.1 also showed asymmetry between the first and second half cycle (concerning the low amplitude current characteristics, best reflected through the sheath edge). Figure 7.2 considers a few half cycles, starting after the half cycle that included the first breakdown. Through the current and sheath edge the discharge is found to be asymmetric over the range shown. This is due to the high electron density created during the first breakdown of which the destruction is not fast enough. As the electrons and ions become trapped in the plasma bulk, only dissociative recombination can break those down efficiently. Note also that still positive columns are formed despite this plasma bulk and that the positive columns are differentiated from this bulk. The first few cycles in Figure 7.2 are still influenced by this bulk. The bulk is not symmetric. The positive column is slightly less intense at the side of the very first instantaneous anode, similarly the negative glow peaks are sharper and smaller there. After the bulk is fully reduced the steady state discharge reported up to now (section 5.1) is reached, approximately after 8 voltage half cycles, based on the metastable density (see Figure 5.14).

Furthermore Figure 7.2 shows that residual current peaks [20], [25] are also observed preceding each breakdown. Between the latter breakdowns, the electric field is non-uniform, considering the full gap, analogous to Martens et al. [57] who described this behavior as a subnormal glow instead of Townsend breakdowns. Comparing the spatial temporal density evolutions of argon to literature ([57] itself but also, i.e. [17]), this argon discharge can be considered to not fully extinguish between the glow discharges, more so than for other reported [17], [57] discharges.

## 7.3. Conclusions

The one-dimensional drift-diffusion model of the atmospheric pressure argon dielectric barrier discharge is used to investigate the various discharge mechanisms and regimes occurring in this discharge by including a very first breakdown through model initialization with low densities. The first breakdown occurred after two half cycles. Due to the uniform electric field preceding this breakdown, it is assumed a Townsend breakdown. The electron are accelerated towards the instantaneous anode and reach a very high density. Subsequently, a negative glow structure exhibiting multi peak behavior is immediately formed, despite a lack of memory effects. In this case those multi peaks are attributed to ionization in the plasma bulk or near the anode and subsequent ion-electron emission and the lag time between those processes. The high electron density from this breakdown gets trapped in the plasma bulk, due to this trapping the main destruction mechanism is assumed to be dissociative recombination. Positive columns are formed in all the subsequent discharges, they are clearly distinguished from the large plasma bulk. Still they are influenced by it and asymmetric behavior is observed in the sheath and current characteristics. For those subsequent glow discharges, the plasma is seen to never really extinguish in between. The discharge stays in a subnormal glow and glow mode.

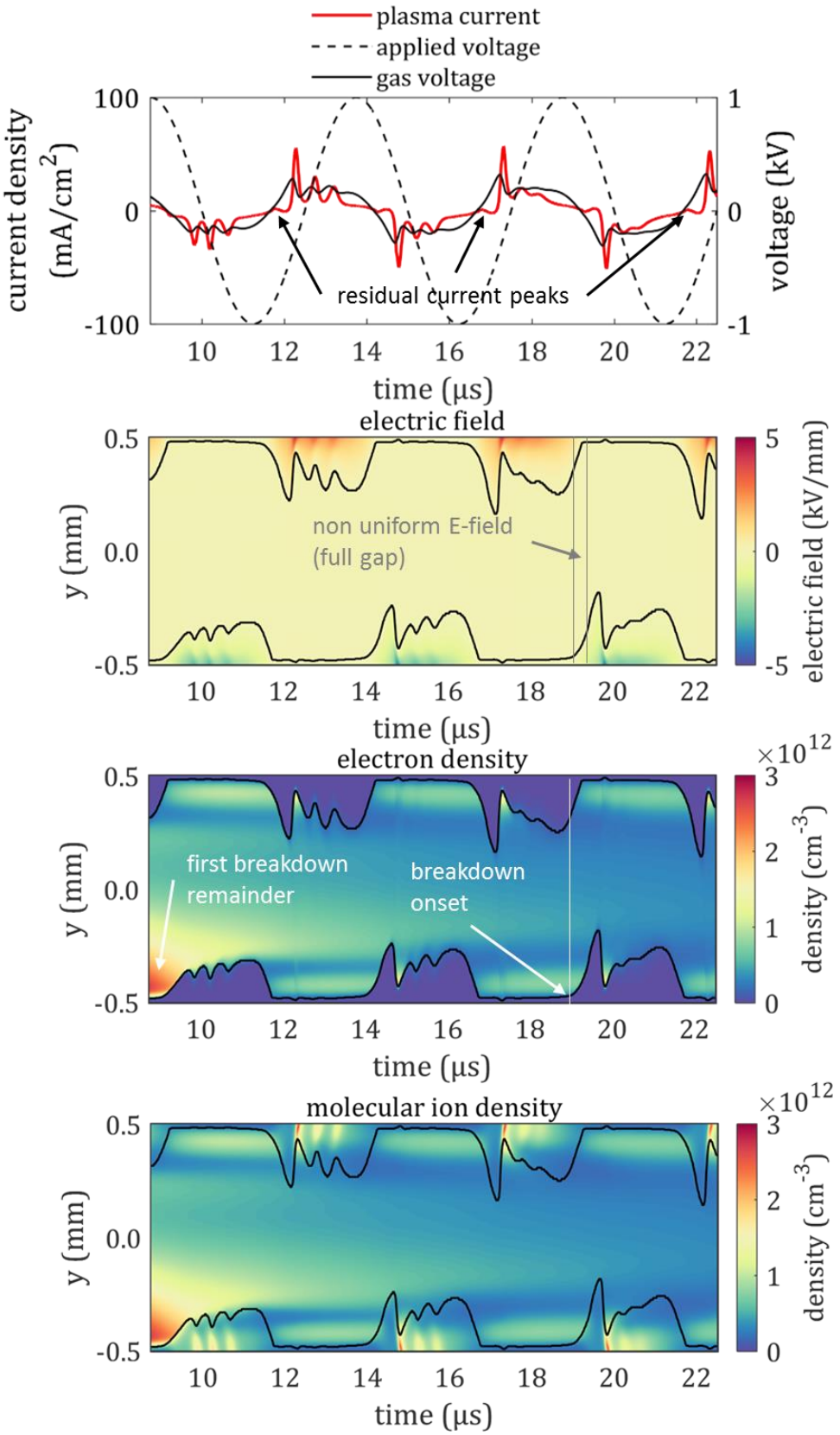


Figure 7.2. The current characteristics, electric field and electron and molecular ion densities during a few breakdown after the first breakdown. The sheath edge calculation is also used (equation 5.1).

# 8. Influence of secondary electron emission on the steady state current characteristics


## Abstract

In an atmospheric pressure argon dielectric barrier discharge the secondary electron emission processes by metastable atoms, atomic ions and molecular ions are considered in isolation. The ions are found to change the discharge in different ways, attributed to the moment at which the ions cause the electron emission and which processes those emitted electrons can participate in (direct ionization or excitation). Up to a certain point an ambiguity, between choosing the ion-electron emission coefficients equal and choosing a fixed value for the atomic ions, while varying that of the molecular ions, is shown. Through numerical studies with combinations of those coefficients, methods are proposed to determine the relation between, or values of, the ion secondary electron emission coefficients by considering multiple aspects of the current characteristics in possible comparison of modelling to experimental measurements.


## 8.1. Introduction

In this chapter the one-dimensional drift-diffusion model is used to investigate the influence of secondary electron emission (SEE) processes on the argon discharge as reported in the previous chapters. Common practice is to consider those processes by a fixed value for the secondary electron emission coefficient $\gamma_p$ (e.g. 0.1 or 0.01) [36], [41], [58], equal for all argon minority species $p$ in the discharge. Metastables are sometimes neglected and most notably there is likely no distinction made between the molecular and atomic ions, considering the assigned SEE coefficients.

In this chapter the current characteristics will be considered over a wide range of the applied voltage (500 to 2500 V) and electron emission will be considered for each species (metastables, atomic ions and molecular ions) separately over a wide range (0 and 0.01 to 0.1 for $\gamma_p$). The remaining conditions are kept equal to the previous reported discharges as reiterated here. The background gas temperature is 450 K, the pressure is 1 atm, the dielectric thickness is 0.1 mm, the dielectric constant is 3.4 and the gas gap is 1 mm. The applied voltage is sinusoidal at a frequency of 200 kHz. The full chemistry set is used (Table 3.2).

With those standard conditions (and an applied voltage of 1 kV as reported in previous chapters) a steady state discharge was also achieved without considering secondary electron emission. Figure 8.1 compares the current characteristics. With the 1 kV applied voltage, only the model inclusive of SEE is in a multi-peak regime, the model without SEE shows only one broad current peak.

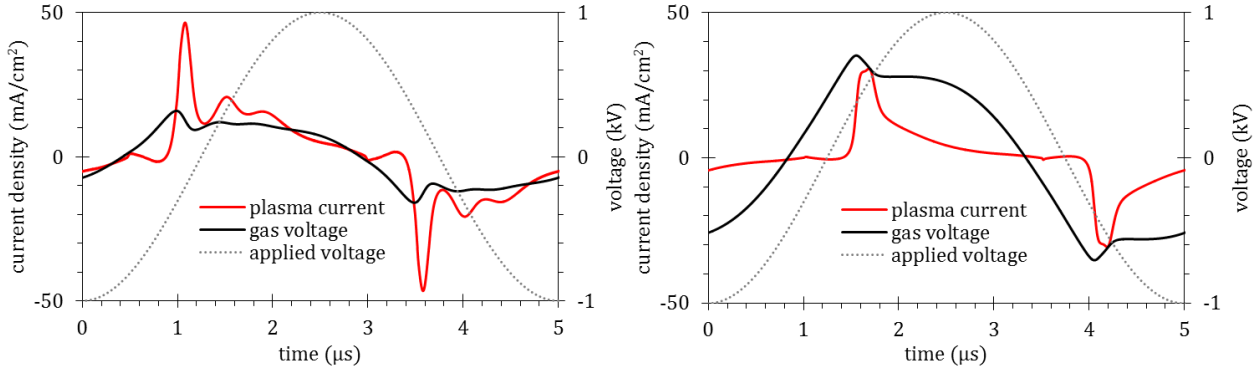


Figure 8.1. Comparison of the current and voltage characteristics for the standard conditions reported up till now (left), which includes secondary electron emission ($\gamma_p = 0.1$) and the same conditions without electron emission (right).

## 8.2. Considering individual secondary electron emission processes

Here secondary electron emission due to metastables, atomic ions and molecular ions are considered in isolation to determine the influence of each process on the discharge current characteristics.

The steady state current characteristics are retrieved from modelling over an applied voltage range of 500 to 2500 V (in steps of 100 V) and for SEE coefficients $\gamma_p$ of 0 to 0.1 (in steps of 0.01). Considering the low voltages especially, the models were initialized with high densities. The plasma current is calculated based on a simple equivalent circuit [1] for the dielectric barrier discharge. The calculation involves the charge-voltage (Q-V) Lissajous Figures from which the $C_{cell}$ and $C_{diel}$ capacitances (of the full reactor and the dielectric only, respectively) are determined [1]. In preceding chapters this was done manually, here however a large amount of individual models are reported. Thus, the capacitance of the dielectrics $C_{diel}$ is assumed constant, given by

$$C_{diel} = \frac{\epsilon_r \epsilon_0}{2 d_\epsilon} \cdot A \tag{8.1}$$

where $\epsilon_r = 3.4$ is the dielectric constant of the dielectric barrier, $\epsilon_r$ the vacuum permittivity $d_\epsilon = 0.1$ mm is the thickness of a single dielectric barrier and $A \equiv 1$ m$^2$ the discharge area, such that $C_{diel} = 150$ nF. The capacitance of the full reactor $C_{cell}$ is still determined from the Lissajous Figures, however this determination is automated. Appendix II.A gives a summary of the calculation of the plasma current as used throughout present study and illustrates how the $C_{cell}$ values were retrieved automatically for model batches. Figure 8.1 had the required $C_{cell}$ values calculated in this way also (55 nF with SEE and 24 nF without). Appendix II.B contains Figures illustrating the calculated values of $C_{cell}$, for model batches, this appendix is referred to in the relevant Figures reporting the plasma currents.

Yoshinaga et al. [26] studied numerically the influence of the separate SEE coefficients on Townsend's second ionization coefficient. Both electron emission by metastables and photons were considered also, the latter through integrating the rate of radiative decay to determine an effective photon flux. In PLASIMO this is not implemented, in present study metastables will be considered only instead of both metastables and photons, among others. It is assumed that the influence of electron emission by photons is similar to the metastables due to their close relation and both having undirected flux (not influenced by the electrical field). The metastables are considered in present study for completeness and because of the study by Yoshinaga [26], were it was shown to influence Townsend's second ionization coefficient for high $pd$ values ($> 1$ Torr cm).

Figure 8.2 shows the current voltage characteristics at an applied voltage of 1 kV and emission coefficient of 0.1 while considering electron emission by metastables only – for comparison against Figure 8.1. Compared to no SEE, the current is increased as well as already having a current shoulder after the initial peak, which was not the case without any electron emission.

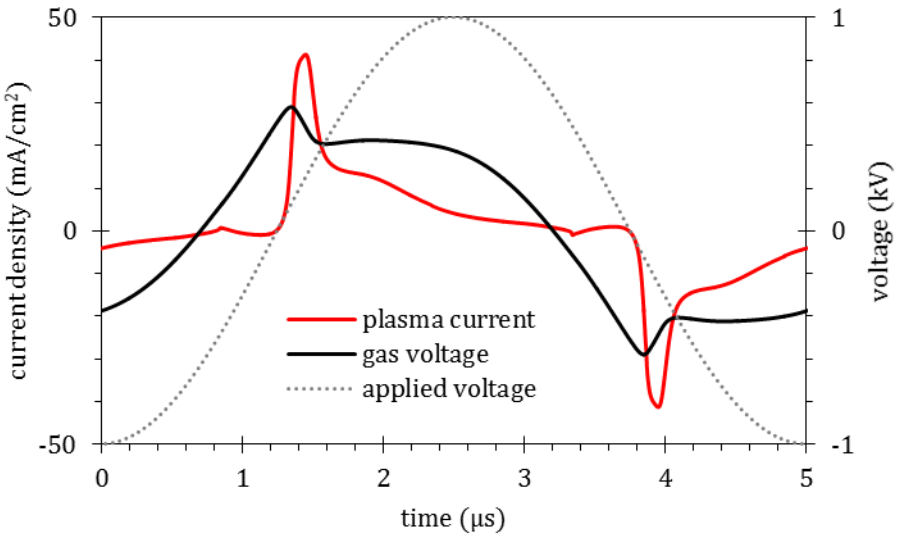


Figure 8.2. The current and voltage characteristics while only considering electron emission by metastable atoms.

Figure 8.3 shows the corresponding maximum plasma current (in the first peak) for all conditions (up to 21 voltages values × 11 SEE coefficient values). Here the set without SEE is included, which is clearly an outlying case. It does not continue the smooth behavior found between any $\gamma_{Ar^*}$ value. The current maximum is seen to be rather constant, over the range of 0.01 to 0.1 for $\gamma_{Ar^*}$, for any given applied voltage.

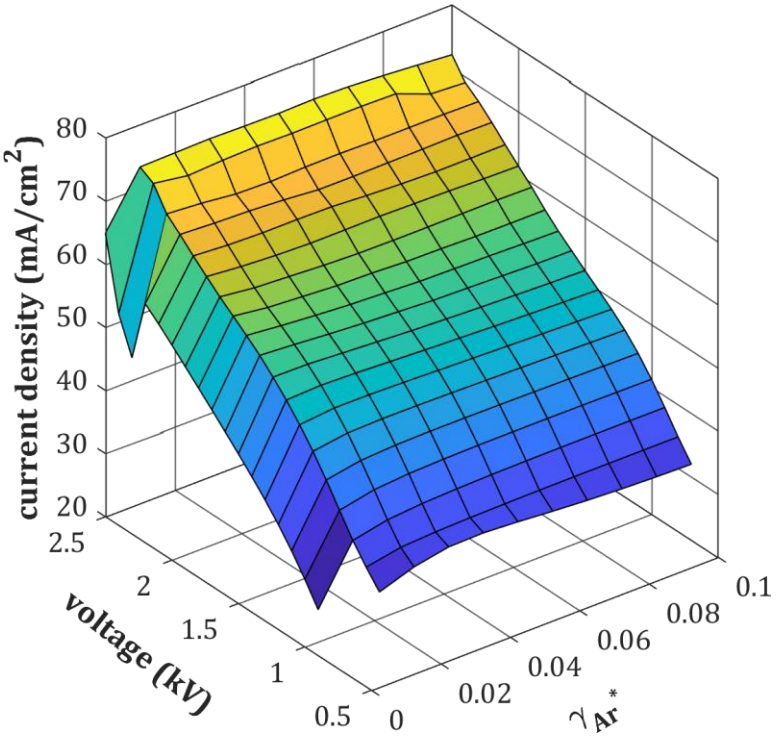


Figure 8.3. The maximum plasma current (first current peak) over a wide range of applied voltages and SEE coefficients, while only considering electron emission by metastable atoms. The required calculated values of $C_{cell}$ are reported in Appendix II.B, Figure 5.

Figure 8.4 shows the single current voltage characteristics at an applied voltage of 1 kV and emission coefficient of 0.1 for the atomic ions only to facilitate comparison against Figure 8.1. It is clear that the first current peak has become much larger (and sharper), the multi-peak current characteristics of the full model (all SEE coefficients equal) are not recognized.

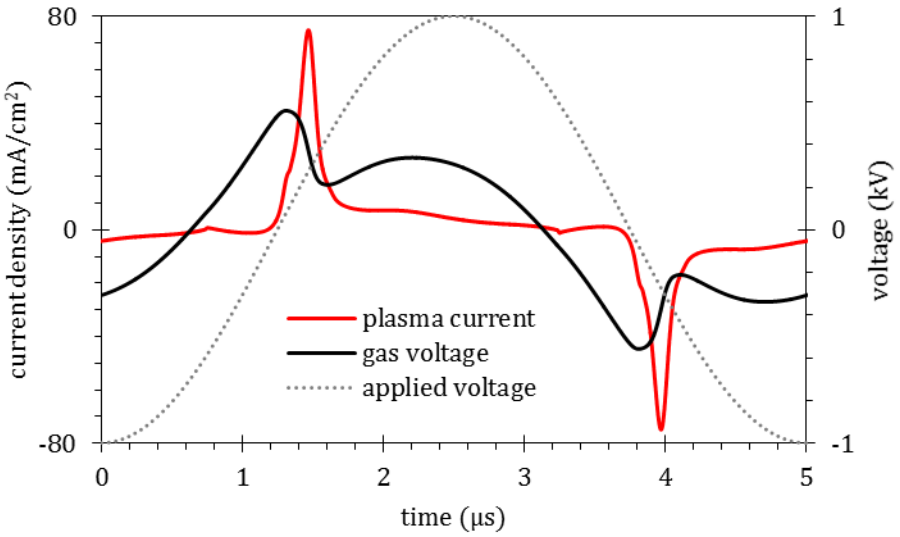


Figure 8.4. The current and voltage characteristics while only considering electron emission by atomic ions.

Figure 8.5 shows the first peak current maximum, it is seen that the maximum current increases not only with the applied voltage but also with the SEE coefficient of the atomic ions.

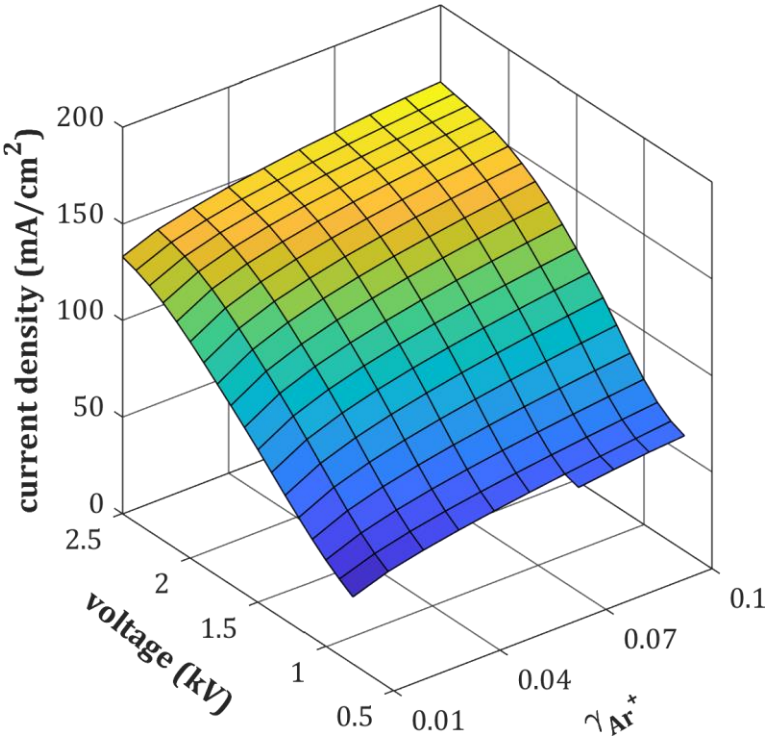


Figure 8.5. The maximum plasma current (first current peak) over a wide range of applied voltages and SEE coefficients, while only considering electron emission by atomic ions. The required calculated values of $C_{cell}$ are reported in Appendix II.B, Figure 6.

Finally only molecular ions are considered. Figure 8.6 shows the single current voltage characteristics at an applied voltage of 1 kV and emission coefficient of 0.1 for the molecular ions only as a comparison against Figure 8.1. Clearly, the (electron emission due to) molecular ions dominates the current characteristics of the full model.

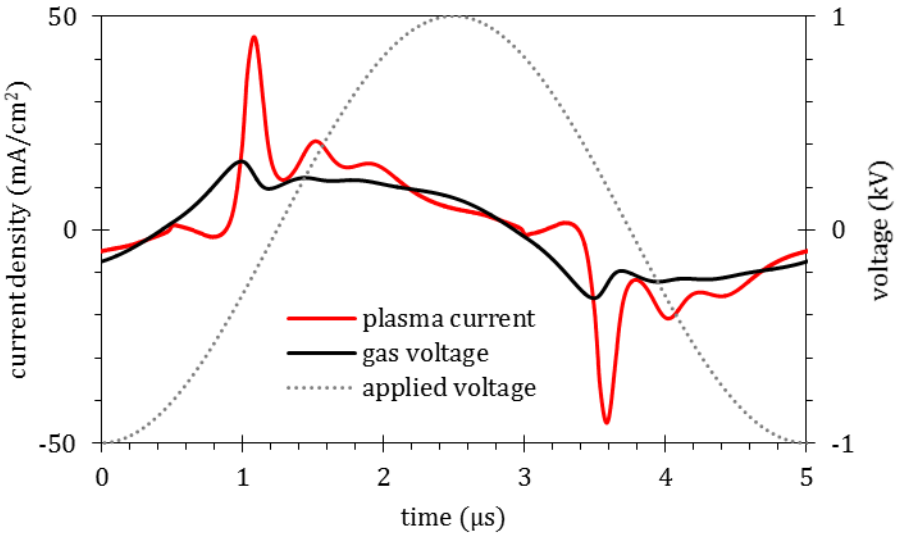


Figure 8.6. The current and voltage characteristics while only considering electron emission by molecular ions.

Figure 8.7 shows the first peak current maximum over the wide range of applied voltage and SEE coefficients. The overall behavior is completely different to Figure 8.5. In this case (Figure 8.7) a plasma was always maintained, starting at 500 V. Starting from 800-900 V the maximum current tends to decrease with increase voltage before increasing again at very high voltages. With increasing SEE coefficient, the current decreases. Compared to the atomic ions, the molecular ion behavior is more in line with the expectancy of higher secondary electron emission yields, causing a discharge that is easier to maintain thus requiring less current. Note that for high SEE coefficients and applied voltages, the maximum current after the first current peak was observed to be in the same order or sometimes even higher. The latter is especially true if the total current would have been considered.

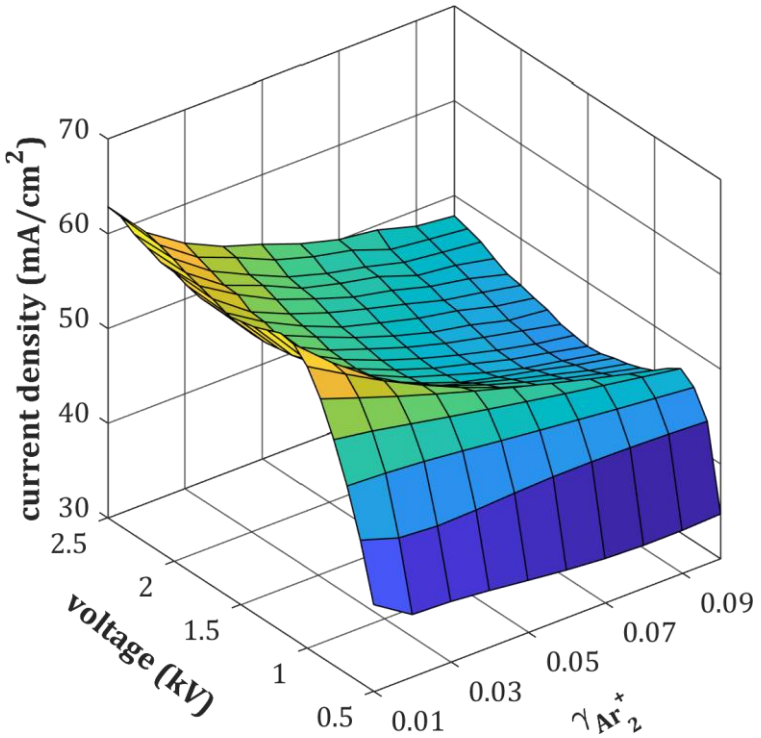


Figure 8.7. The maximum plasma current (in the first current peak) over a wide range of applied voltages and SEE coefficients, while only considering electron emission by molecular ions. The required calculated values of $C_{cell}$ are reported in Appendix II.B, Figure 7.

In section 8.3, combinations of the secondary electron emission coefficients of both ions are considered. The applied voltage will be kept constant. In order to determine voltages of interest, various regimes of the current characteristics are chosen based on the models where electron emission by molecular ions was considered only, because the comparison to the full model showed that it was the dominant process. Table 8.1 lists the current characteristics of interest, the chosen applied voltage and the $\gamma_{Ar_2^+}$ values for which it was observed. Figure 8.8 shows the corresponding current characteristics.

Table 8.1. The various observed current characteristics (in the models accounting for electron emission by molecular ions only) and the applied voltage with which those regimes are associated.

| | Current characteristics of interest | Chosen applied voltage (V) | Approximately observed for $\gamma_{Ar_2^+}$ |
|---|---|---|---|
| (a) | Single peak without shoulder (monotonically decreasing after 1st peak) | 500 | 0.01 … 0.1 |
| (b) | Single peak, with shoulder | 900 | 0.02 … 0.1 |
| (c) | multi-peak, with a clear first peak maximum | 1200 | 0.04 … 0.1 |
| (d) | Multi-peak, with secondary current peaks of the same order | 2500 | 0.05 … 0.1 |

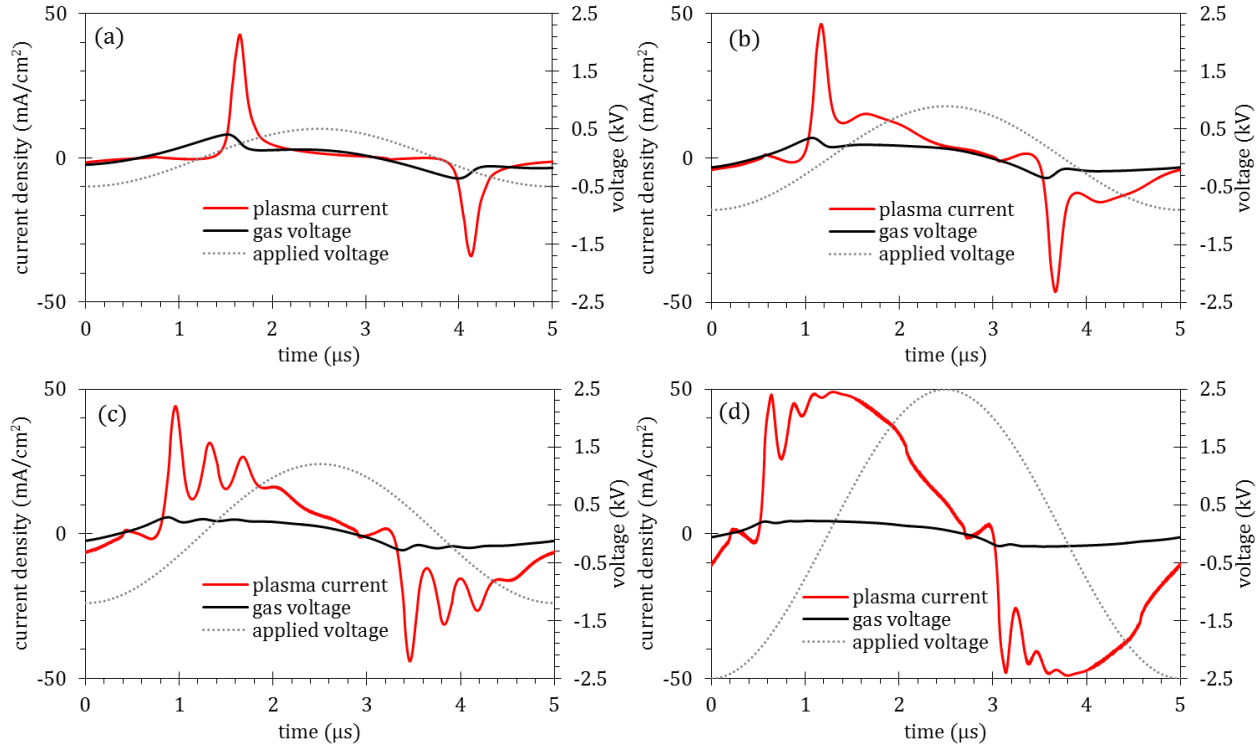


Figure 8.8. The various types of current characteristics observed over the wide range of applied voltages, corresponding to table 8.1 with secondary electron emission by the molecular ions only (coefficient set to 0.1).

In summary, a large difference in behavior is observed when the ion-electron emission at the dielectric surfaces are considered in isolation. SEE by atomic ions only causes a larger first current peak. It is assumed that in this case the atomic ion-electron emission is significant during the first negative glow formation, where the electric field is still high and direct ionization takes place mainly (see also section 5.1.4), and relatively insignificant in the latter phases. The electron are thus emitted during the high electric field phase allowing them to still participate in direct ionization and consequently promoting the initial negative glow further. Figure 8.9 shows the spatial electron density corresponding to a model without SEE (right figure of Figure 8.1) and of the model with SEE by atomic ions only (corresponding to Figure 8.4). For the applied voltage of 1 kV it is not extremely clear, but the negative glow reaches closer to the cathode and the peak is widened.

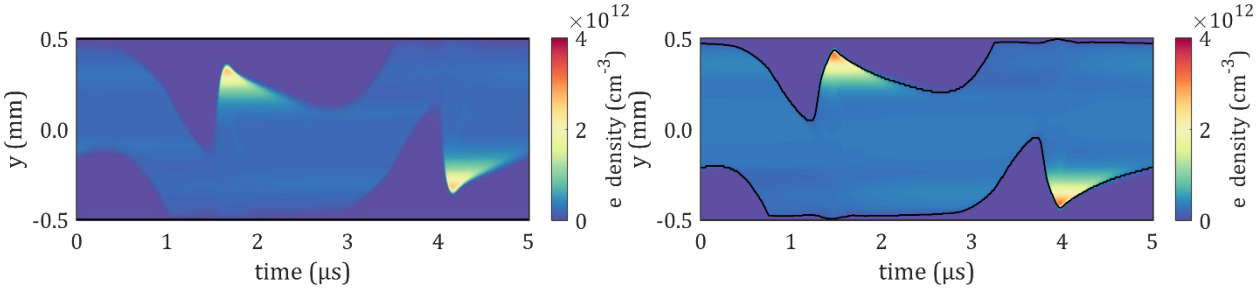


Figure 8.9. The spatial temporal electron density during a steady state voltage cycle for a model without any secondary electron emission (left) and one by atomic ions only (coefficient of 0.1, right). For an applied voltage of 1 kV.

Chapter 6 discussed how the formation of the positive column in the previous half cycle was responsible for memory charge preceding the current half cycle, causing breakdown at lower applied voltages and subsequently allowing the gas voltage to again pass the breakdown voltage causing a

multi peak structure in the discharge. The formation of the positive column was due to metastable-metastable ionization. In turn, this requires metastables which are created through excitation in the cathode fall regions. The IV characteristics due to the molecular ions are assumed to be due to this mechanism. The molecular ion-electron emission is significant enough during phases after the initial breakdown such that emitted electrons significantly contribute to excitation, effectually leading to a positive column of higher density, increasing the ease at which the discharge occurs and reducing the current required to maintain the discharge. Figure 8.10 shows the spatial electron density corresponding to the models of Figure 8.8, indeed showing pronounced positive columns with higher densities for the multi-peak cases. With higher applied voltage the bulk in between the positive column and negative glow (the Faraday dark space) becomes wider and the discharge become more continuous.

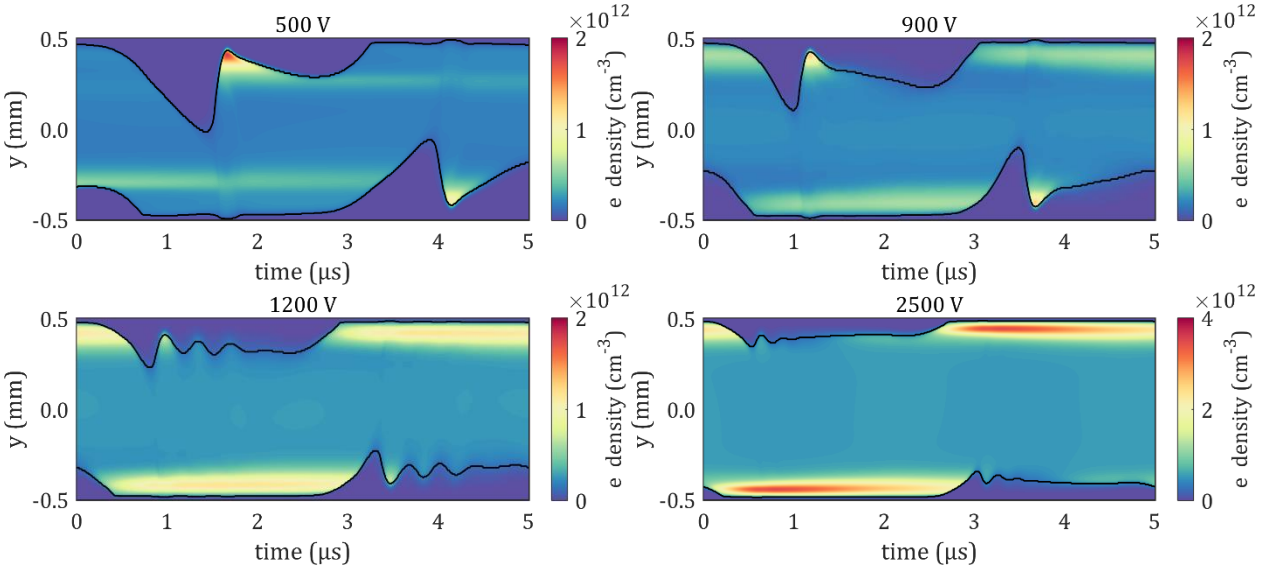

Figure 8.10. The spatial temporal electron density during a steady state voltage cycle for models only considering secondary electron emission by molecular ions (coefficient is 0.1) at various applied voltages.

## 8.3. Combined ion-electron emission coefficients

A wide range of combinations of the atomic and molecular ion SEE coefficients will be considered – 10 × 11 SEE coefficients, including 0 for the atomic ions – at the applied voltages as determined in the previous section and listed in Table 8.1 (0.5, 0.9, 1.2 and 2.5 kV). The SEE coefficient of the metastable is set to 0.1 and will no longer be considered specifically as the current was shown to not increase significantly at any given applied voltage, in the isolated treatment, apart from turning this SEE process on (see Figure 8.3).

Figure 8.11 shows the current peak maximum corresponding to the four chosen voltages. The lines indicate equal ion-electron emission coefficients. For all applied voltages (0.5, 0.9, 1.2 and 2.5 kV) it is seen that the current decreases with secondary electron emission coefficient $\gamma(Ar_2^+)$. The atomic ions in isolation caused the current to increase with increasing $\gamma(Ar^+)$ (Figure 7.5), this behavior still comes through upon combination, though it is not significant enough. It is found that the current maximum in the intermediate applied voltage (900 V) is more or less linear in $\gamma(Ar_2^+)$, while the higher applied voltages (1.2 and 2.5 kV) are logarithmic in $\gamma(Ar_2^+)$.

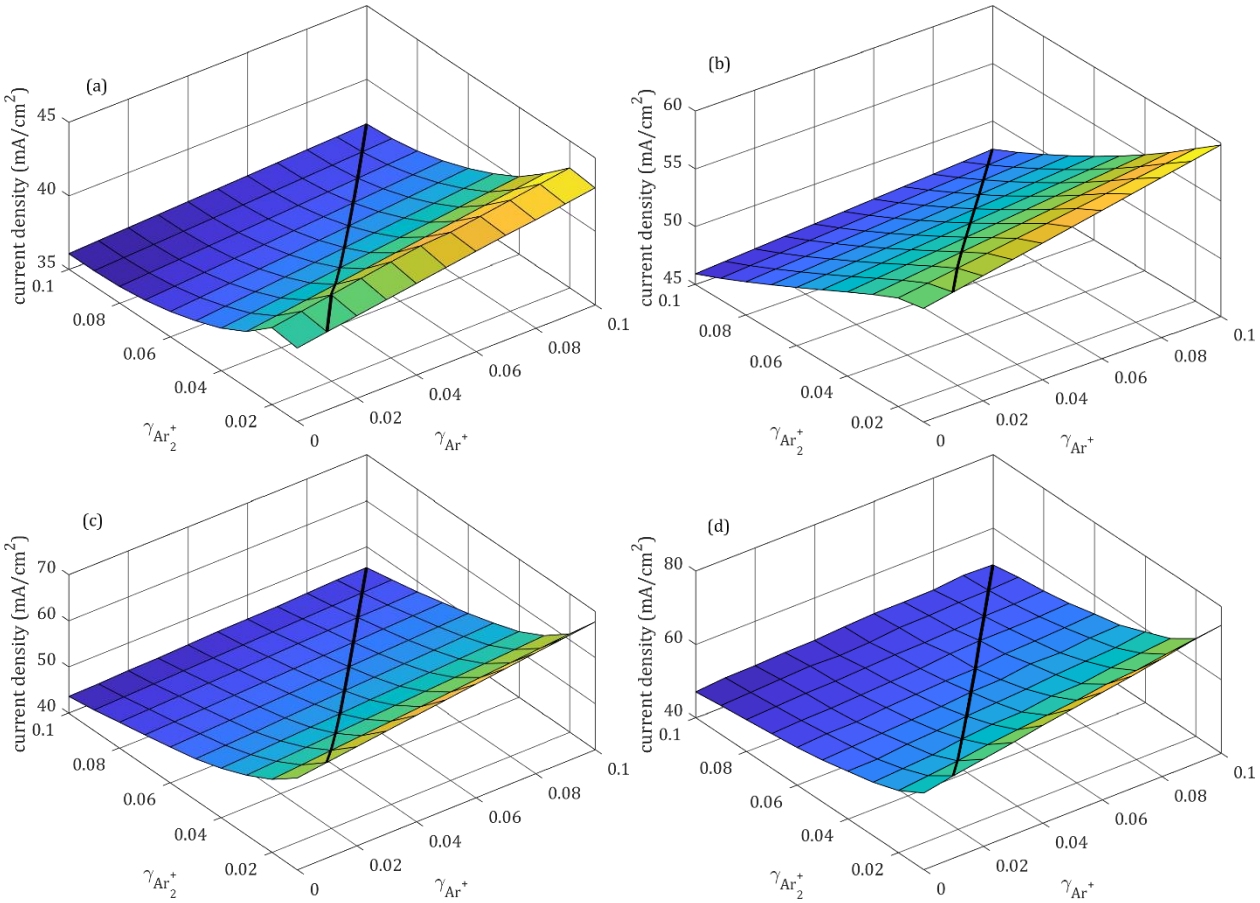


Figure 8.11. The first peak current maximum over a wide range of secondary electron emission coefficient for both ions at specific applied voltages; 0.5 kV (a), 0.9 kV (b), 1.2 kV (c) and 2.5 kV (d) (see table 8.1). The solid line indicates $\gamma_{Ar_2^+} = \gamma_{Ar^+}$. The required calculated values of $C_{cell}$ are reported in Appendix II.B, Figure 8 through 11.

Based on those results there is an ambiguity in choosing secondary electron emission coefficients for the ions. As noted in the introduction, the atomic ions and molecular ions are chosen equal in most argon modelling studies. Indeed the modelled current shows similar behavior for choosing $\gamma(Ar_2^+) \equiv \gamma(Ar^+)$ or $\gamma(Ar_2^+) \leq \gamma(Ar^+)$ with the atomic ion value fixed to a certain value. This is reflected in Figure 8.12, where the current densities reported in Figure 8.11 are plotted as a function of $\gamma(Ar_2^+)$ for the case of equal SEE coefficients (solid line in Figure 8.11) and for when $\gamma(Ar^+) = 0.1$. Considering that relatively smooth trends are shown for all the applied voltages under investigation expect for one outlying case through low $\gamma(Ar_2^+)$ and low applied voltage (0.01 at 500 V, Figure 8.11a), a minimum value for any $\gamma_{ion}$ can be chosen, say 0.01 or 0.02. Then there is actually a possibility to determine if $\gamma(Ar_2^+) \equiv \gamma(Ar^+)$ or $\gamma(Ar_2^+) \leq \gamma(Ar^+)$ would be true, if measured current – at a specific applied voltage – are high enough to differentiate between the two, as can be seen in Figure 8.12. The modelling results indicate that higher applied voltages could facilitate this approach better.

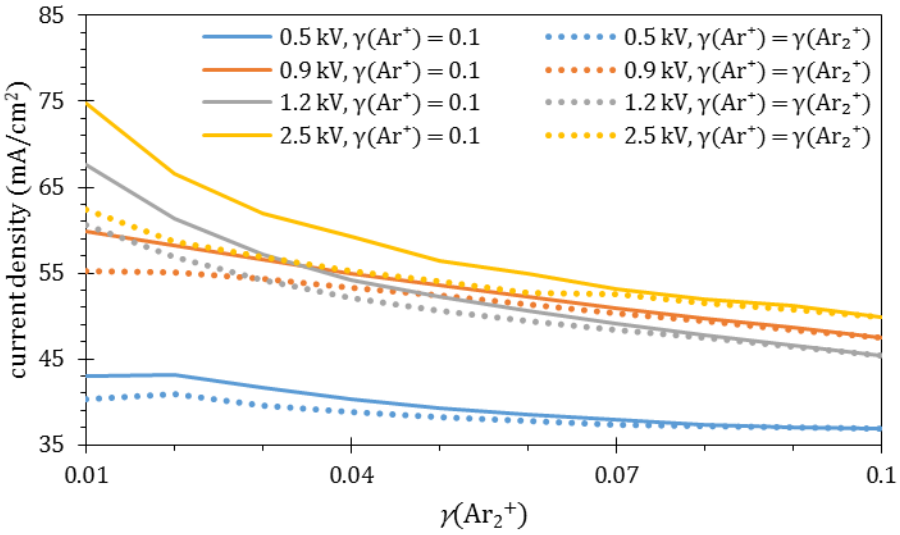


Figure 8.12. The first peak current maximum over a range of secondary electron emission coefficient by either choosing the SEE coefficients of atomic ions equal to molecular ions (dashed lines) or by choosing a fixed value for the atomic ions (solid lines) at specific applied voltages (legend).

In addition to the first current peak maximum, the latter current characteristics can also be considered – except for the case where the current is monotonically decreasing (500 V). The maximum current in the second current peak (Figure 8.8c and 8.8d) or of the broad shoulder (Figure 8.8b) shows smooth behavior over the modelled SEE coefficients, like Figure 8.11. Figure 8.13 shows the current maximum in the characteristics after the first peak, again both for $\gamma(Ar_2^+) \equiv \gamma(Ar^+)$ and $\gamma(Ar_2^+) \leq \gamma(Ar^+)$. The intermediate ranges are of interest (900 and 1200 V), it is seen that the characteristics do not differ from each other based on the choice of $\gamma(Ar_2^+) \equiv \gamma(Ar^+)$ or $\gamma(Ar_2^+) \leq \gamma(Ar^+)$. Thus, in those regimes the secondary current characteristics depend only on $\gamma(Ar_2^+)$ and could be used to find this value after which the first peak characteristics can be used to determine $\gamma(Ar^+)$.

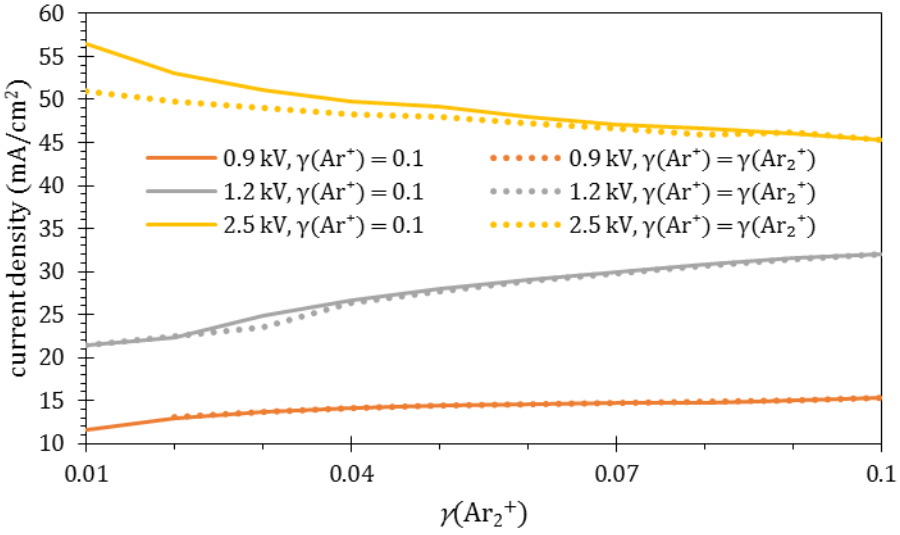


Figure 8.13. The current maximum in secondary current characteristics (second peak or broad shoulder) over a range of secondary electron emission coefficient by either choosing the SEE coefficients of atomic ions equal to molecular ions (dashed lines) or by choosing a fixed value for the atomic ions (solid lines) at specific applied voltages (legend).

Finally, instead of considering either Figure 8.12, 8.13 or both separately in possible determination of SEE coefficients from experimental measurements, ratios determined from the current (peak) characteristics can also be a reliable approach for such comparisons because those comparisons will then be based on unit less quantities and thus do not depend on discharge areas.

## 8.4. Conclusions

Secondary electron emission was considered on a per species basis in an atmospheric pressure argon dielectric barrier discharge. Upon isolation of secondary electron emission of the atomic ions and molecular ions it was found to change the current characteristics in different ways. With increasing ion-electron emission by atomic ions only, the first peak current maximum is promoted significantly. This was attributed to the electron emission mainly taking place during the discharge when there is still a high electric field in the cathode fall regions allowing the emitted electrons to participate in direct ionization processes such that the negative glow of the discharge is promoted further. With increasing ion-electron emission by molecular ions only, the multi-peak behavior of the discharge gets promoted. This was attributed to significant electron emission, during later stages of the discharge, into the cathode fall, such that those electrons participate in excitation instead. The increased amount of excited argon causes larger positive columns in subsequent breakdowns which in turn enable the gas to break down easier in subsequent breakdowns. Upon combination of those secondary electron emission coefficients, both behaviors were still visible. However, the contribution of the atomic ions can be considered insignificant under the investigated conditions. In a numerical study of those coefficients and current characteristics it was shown that there indeed is an ambiguity between choosing the molecular ion secondary electron emission coefficient equal to that of the atomic ion and setting a specific value for the atomic ion, while varying the molecular ion coefficient. Still, by considering multiple aspects of the current characteristics, modelling to experimental comparison methods are proposed to confirm one of those relations, including possible determination of those ion-electron emission coefficients.

# 9. Numerical simulation of atmospheric pressure 200 kHz / 13.56 MHz dual frequency dielectric barrier discharges[1]


## Abstract

A one-dimensional drift-diffusion model is used to study atmospheric-pressure dual frequency (DF) dielectric barrier discharges in argon using the plasma modelling platform PLASIMO. The simulation exhibits an excellent agreement with the experimental results and gives insight into the DF plasma dynamics e.g. the electric field, the sheath edge profiles, the ionization/excitation rate and the electron energy distribution function (EEDF) profiles. The results indicate that due to the RF oscillation, the electric field, the sheath edge and thus the ionization/excitation are temporally modulated. As a result, the plasma conductivity is enhanced as the plasma density is higher. The discharge development is slowed down with a lower current amplitude and a longer duration. The time-averaged sheath is getting thinner with a more pronounced ionization rate near the substrate, which could help to improve the efficiency of plasma-assisted surface processing. In addition, the DF excitation exhibits a capability of modifying the EEDF profiles and controlling the plasma chemical kinetics, which can be applied to the other relevant fields e.g. gas phase chemical conversion.


In the simulation a conventional DBD system with two parallel electrodes is used. Both the electrodes are covered by an insulating layer with a dielectric constant of 3.4. The discharge is generated in an effective discharge area of 1 m × 1 m with a narrow gas gap of 1.0 mm. One electrode is grounded, while the other one is driven by a DF voltage composed of 200 kHz LF and 13.56 MHz RF waveforms. The gas temperature is fixed at $T_g = 450$ K [51]. The secondary electron emission coefficient (γ) is set to 0.07 [59]. The LF voltage ($U_{LF}$) is maintained at 1000 V, while the RF voltage ($U_{RF}$) gradually increases from 0 V to 250 V.

## 9.1. Voltage-current waveforms

The simulated voltage and current density waveforms of the DF discharges within one LF cycle (5 μs) are illustrated in Figure 9.1. The LF discharge current contains a single smooth peak every half LF cycle, while in the DF discharges ($U_{RF} > 0$ V), both the current density and the voltage are a superposition of the LF and RF components. By doing fast Fourier transform (FFT) of the original waveforms, the fundamental signals of LF (200 kHz) and RF (13.56 MHz) in the DF discharge can be separated in the frequency domain. Typical FFT spectra of voltage and current density in the DF discharge ($U_{LF} = 1000$ V, $U_{RF} = 250$ V) are shown in Figure 9.2. The FFT amplitudes of current density as a function of URF are presented in Figure 9.3. With URF increasing from 0 V to 250 V, the LF current density increases slightly from 17.3 A to 19.2 A, while the RF current density increases significantly from 0 A to 60.9 A. A similar electrical behaviour was also observed in the experimental study in [13], which is attributed to the fast increase of the capacitive component of the RF current [60].

[1] As output of the present study a paper (below) has been submitted for publication. In this chapter some excerpts from this paper – relevant to the participation – are presented (verbatim).

Liu, Y., van 't Veer, K., Peeters, F., Mihailova, D., van Dijk, J., Starostine, S., Van de Sanden, R., De Vries, H. "Numerical simulation of atmospheric-pressure 200 kHz / 13.56 MHz dual-frequency dielectric barrier discharges" Accepted for publication in Plasma Sources Science and Technology

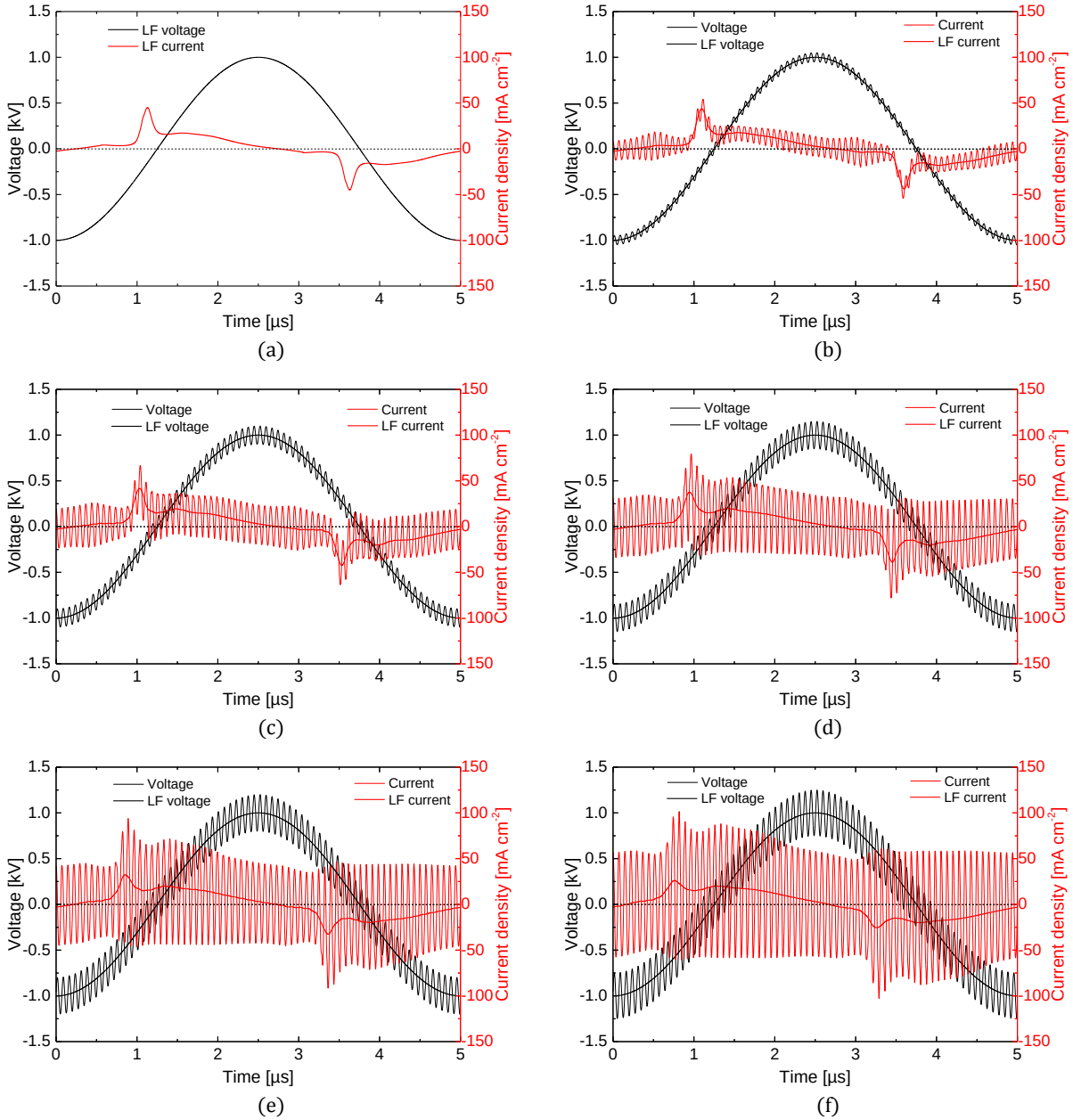


Figure 9.1. Original and FFT-filtered voltage-current density waveforms of the DF discharges with $U_{RF}$ of (a) 0 V, (b) 50 V, (c) 100V, (d) 150 V, (e) 200 V and (f) 250 V. $U_{LF}$ = 1000 V under all conditions.

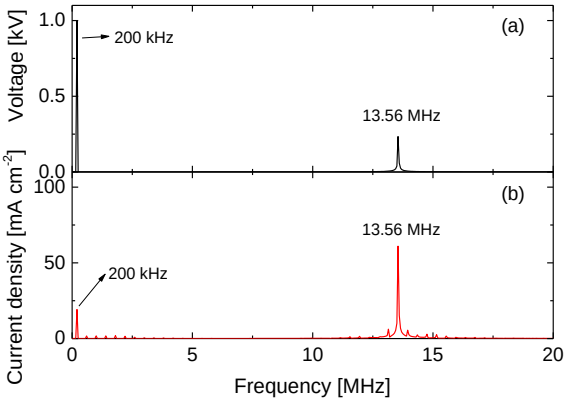


Figure 9.2. Fast Fourier transform (FFT) spectra of (a) voltage and (b) current density in the DF discharge with $U_{LF} = 1000$ V, $U_{RF} = 250$ V.

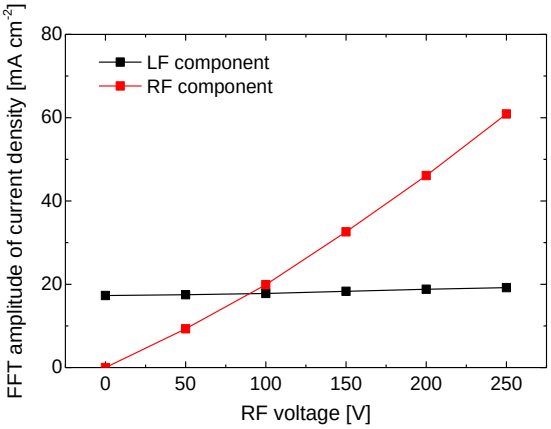


Figure 9.3. Variations of the FFT current density components as a function of $U_{RF}$.

## 9.2. Low frequency vs dual frequency

Figure 9.4 shows the plasma parameters from both simulations and experiments of LF and DF discharges within one LF cycle (5 μs). The phase and space resolved electric field, power absorbed by electrons, direct ionization rate, excitation rate and experimental discharge emission are presented in plots (a) to (j). The solid lines indicate the sheath edges between the plasma bulk and the plasma sheath, which are determined assuming an equivalent sharp electron step [52]. The method to obtain the phase resolved discharge emission was previously introduced in [61]–[63].

A good agreement between the experimental PROES [Phase Resolved Optical Emission Spectroscopy] of Ar 750 nm (Figure 9.4e and 9.4j) and the simulated excitation rate profiles (Figure 9.4d and 9.4i) is found in both LF and DF discharges. The asymmetrical structure of the discharge emissions between two opposite polarities of the voltage is attributed to the particular electrode configuration (a top curved electrode and a bottom flat electrode) in this study [13], [14]. The ionization rate (Figure 9.4c and 9.4h) is a few times lower than the excitation rate (Figure 9.4d and 9.4i) and can only be observed inside the sheath. This is due to the higher ionization threshold (15.8 eV) than the excitation threshold (11.5 eV). The high energy electrons are mainly generated in the strong electric field (maximum 4 kV/mm) inside the sheath (Figure 9.4a and 9.4f), while the dominant electron power absorbance in the bulk area is through Ohmic heating [64]. In this study, the electron power absorbance (Figure 9.4b and 9.4g) has the same spatio-temporal pattern as the excitation rate (Figure 9.4d and 9.4i).

## 9.3. Different phases of the dual frequency plasma

The detailed phase and space resolved plasma parameters at different phases in the initial stage of the DF discharge in Figure 9.4 are presented in Figure 9.5. Depending on the phase of the LF cycle, the RF oscillation results in a different discharge behaviour.

In phase (1) from 0.13 μs to 0.28 μs, the electric field is comparable on the two electrodes (Figure 9.5a). The maximal electric field is ~1850 V/mm inside the top sheath and ~1780 V/mm inside the bottom sheath. The ionization only occurs within the sheath regions (Figure 9.5c). Three structures

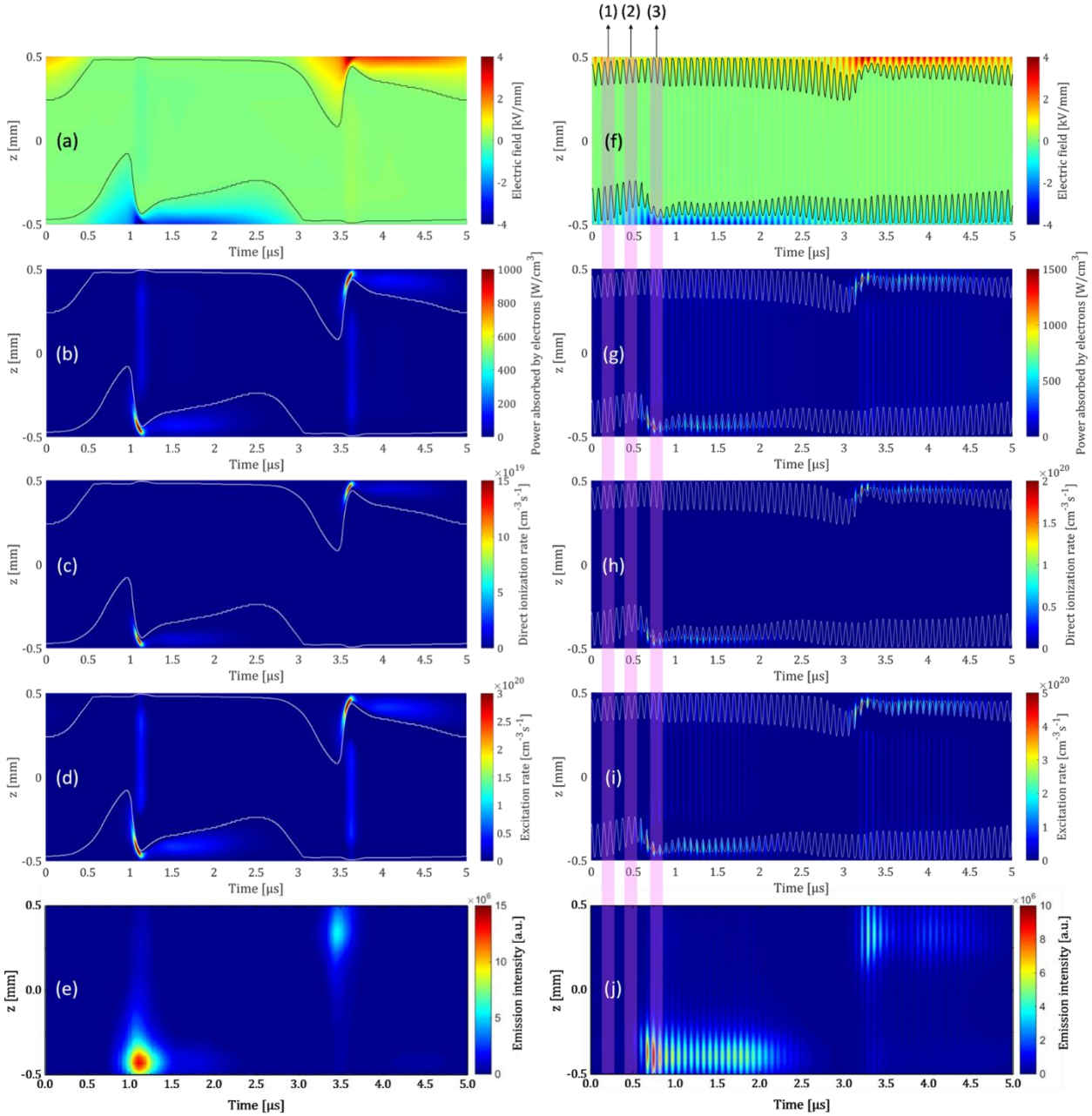


Figure 9.4. Phase and space resolved electric field (first row), power absorbed by electrons (second row), direct ionization rate (third row), excitation rate (fourth row) and experimental discharge emission (fifth row). Left column: LF discharge with $U_{LF} = 1000$ V, right column: DF discharge with $U_{LF} = 1000$ V and $U_{RF} = 250$ V. The solid lines indicate the sheath edges. The shaded areas in the right column indicate the 3 phases which would be discussed in the following section [Figure 9.5].

including sheath expansion, sheath collapse and excitation within the sheath [63], [65] can be observed near both the electrodes, as presented in the excitation rate profiles in Figure 9.5d and the discharge emission in Figure 9.5e.

In phase (2) from 0.40 μs to 0.55 μs, due to the increase of the LF voltage, the sheath thickness as well as the electric field on the bottom electrode are higher than the top electrode (Figure 9.5f). The maximal electric field is ~1550 V/mm inside the top sheath and ~ 2300 V/mm inside the bottom sheath. The ionization however can only be observed within the bottom sheath (Figure 9.5h). The excitation rate and the discharge emission exhibit asymmetrical structure with a more pronounced discharge near the bottom electrode, see Figure 9.5i and 9.5j.

In phase (3) from 0.70 μs to 0.85 μs, due to the particularly high ion density close to the cathode, the sheath thickness is minimum, while the electric field is maximum close to the bottom electrode (Figure 9.5k). The maximal electric field is ~1490 V/mm inside the top sheath and ~4300 V/mm inside the bottom sheath. As a result, the ionization intensity within the bottom sheath is maximum. The excitation rate and the discharge emission are pronounced in both the bottom sheath and the bulk region, as presented in Figure 9.5n and 9.5o.

It has been demonstrated that at different phases of the LF cycle, the DF discharge experiences temporally-modulated dynamics with different ionization/excitation mechanisms depending on sheath edge, electric field and charge density. Within the sheath region, the ionization/excitation mechanisms are mainly dominated by the electric field and thus the electron energy in the sheath. The sheath expansion structure of the excitation, however, is due to the electron acceleration by the sheath oscillation towards the opposite electrode. Therefore it is mainly influenced by the sheath oscillation velocity [66] which depends on the spatial movement of the sheath edge and thus on the local ion density [67]. When the sheath collapses, the collision rate at atmospheric-pressure is so high that the generated electrons cannot instantaneously follow the retreating sheath merely by diffusion. Instead, a self-consistent electric field builds up to drive the electrons, creating a region of negative space charge. The resulting electric field accelerates the electrons toward the electrode and heats the electrons in the process [68].

## 9.4. Conclusions

A time-dependent, one-dimensional (1D) drift-diffusion model […] was employed to study the atmospheric-pressure DF dielectric barrier discharges in argon. The simulation results exhibit an excellent agreement with the experimental results e.g. the electrical characteristics and the phase-resolved discharge emission. In addition, the simulation gives an insight into the DF plasma dynamics e.g. the electric field, the electron density distribution, the ionization/excitation mechanisms, [and] the sheath edge profiles […]. […] Due to the RF oscillation, the electric field and the sheath edge are temporally modulated, leading to a time-varying ionization/excitation rate. As a result, the discharge development is slowed down with a lower current amplitude and a longer duration, which can help to improve the uniformity and stability of discharge. […]

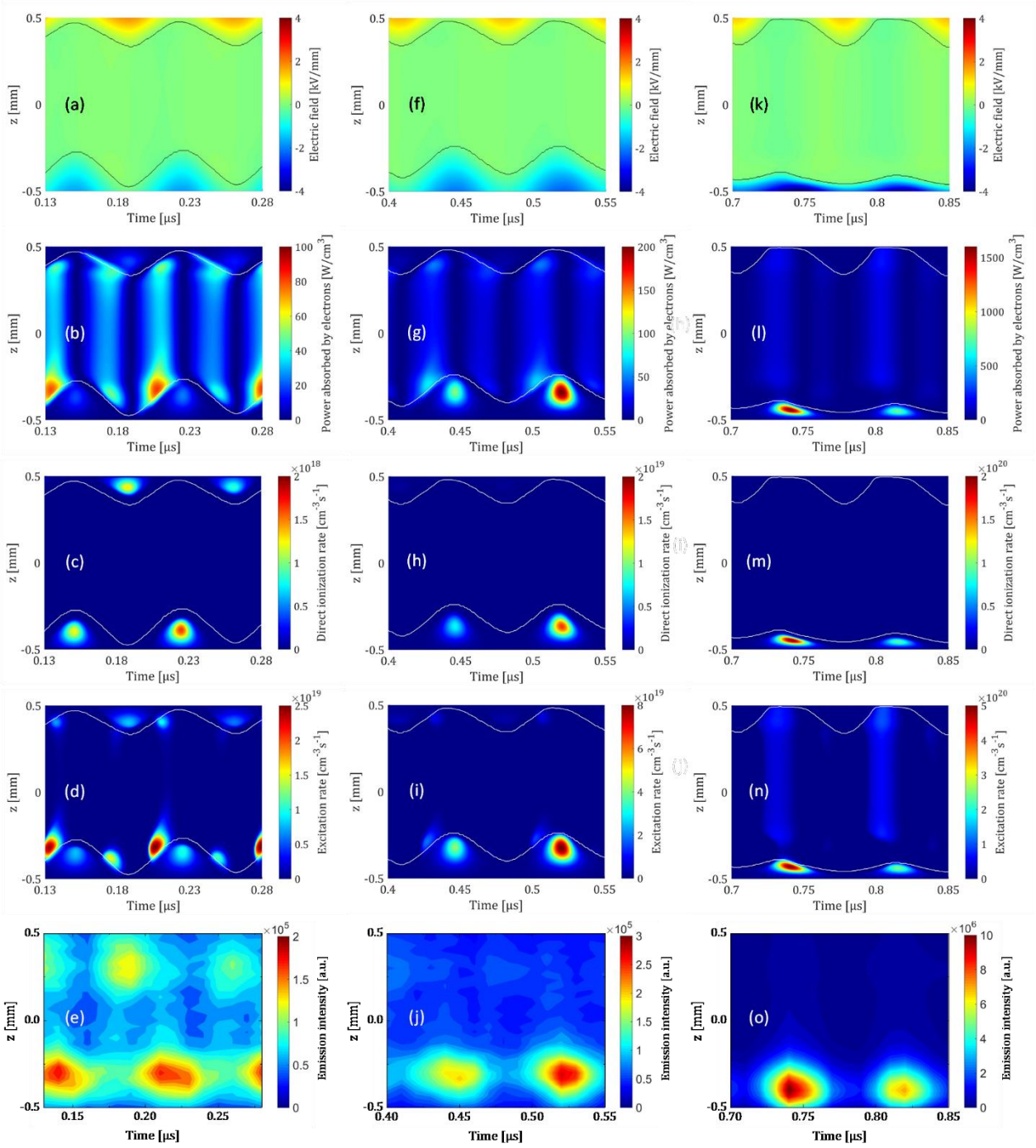


Figure 9.5. Phase and space resolved electric field (first row), power absorbed by electrons (second row), direct ionization rate (third row), excitation rate (fourth row) and experimental discharge emission (fifth row) of the DF discharge with $U_{LF}$ = 1000 V and $U_{RF}$ = 250 V. Left column: phase (1) from 0.13 µs to 0.28 µs, middle column: phase (2) from 0.40 µs to 0.55 µs, and right column: phase (3) from 0.70 µs to 0.85 µs. The solid lines indicate the sheath edges. The numbers of the phases correspond to those in Figure 9.4.

# 10. Two-dimensional modelling of a dielectric barrier discharge in a roll-to-roll geometry


## Abstract

A two-dimensional drift-diffusion model is used to model an argon dielectric barrier discharge in a roll-to-roll plasma reactor. Due to the non-homogenous field with a lateral component the glow-like plasma is seen to expand over multiple half cycles. This expansion occurs during the phases where a negative glow exists. The negative glow first forms in the main discharge direction, after charge deposition on the instantaneous cathode the negative glow develops according to a preferential path along the dielectric surface. Different secondary electron emission coefficients are considered. Higher values yield higher plasma widths. A model that is non-uniform in the electron emission coefficient showed to ignite away from the smallest gap and yield an asymmetric steady state plasma.


## 10.1. Introduction

Past experimental work by Starostin and coworkers [9]–[11] has shown how an diffuse atmospheric pressure dielectric barrier discharge is formed in both parallel and roll-to-roll geometries (curved electrode configurations). Experiments in parallel plate configurations [9], [10] showed that first a (mostly uniform) Townsend discharge occurs which transitioned to a glow discharge at one or more spots. Those spots are local and diffuse. The typical atmospheric pressure glow structure (cathode fall, negative glow, faraday dark space and the plasma bulk) were observed. Those glow current spots induce horizontal ionization waves. The discharge extinguished at the origin of those waves. The glow discharge was not observed to momentarily occupy the whole electrode. However, time averaged the discharge was uniform [9], [10]. The ionization wave is explained through the local deposition of surface charge at the glow current spot on the dielectric where consequently the electric field reduces. It becomes too low to support the plasma, while the electric field in the transverse direction is still strong enough to support ionization processes [9], [10].

Due to the modelling approaches in the present study, the above behavior would not be correctly grasped. If a two-dimensional parallel plate model would be used, the boundary conditions imposed on the electric field at open boundaries will be Homogenous Neumann as the models employed in this present study do not include any specific region exterior to the gaseous gap itself. The drift-diffusion model does not capture the stochastic processes, as are involved with the formation of the Townsend discharge and local current spots. This combined results in that a parallel plate two-dimensional model, in current modelling efforts, would simply be a translated one-dimensional model.

Later Starostin et al. [11] reported on the plasma expansion in a, thin film deposition relevant, roll-to-roll geometry, where the plasma expansion was reported with respect to curved electrode configurations, i.e. non uniform gap size. The plasma ignition occurred at the smallest gap due to lower $pd$ values and overall operation on right branch of the Paschen curve. Also here the first observed stages of the discharge were attributed to a Townsend discharge. This is again followed by the ionization wave. Here a weak asymmetry was observed and attributed to the gas flow. The asymmetry was assumed to be caused by less excited species and lower gas temperature near the gas inlet [11].

In modelling this curved electrode system, the electric field is by definition not homogenous across the full gap width, thus globally the experimental behavior could principally be studied using the drift-diffusion model and aforementioned modelling approaches in present study.

In recent experiments conducted by Liu et al. [12] the plasma expansion was investigated in a similar roll-to-roll geometry over larger time scales (up to 10 s). It was found that the eventual steady state plasma could be asymmetric depending on the gas flow, the used dielectric and its surface properties and the transport direction of the dielectric foil. Specifically, it was shown that the surface roughness and thus the effective surface area increased for specific polymeric dielectric foils due to plasma etching. Upon transporting this foil out of the plasma, the dielectric surface is effectively changed when – somewhere around – passing the smallest gap distance. The steady state plasma width was shown to be asymmetric, extending more in the areas where the dielectric was modified. The increased surface roughness and area was assumed to yield a higher secondary electron emission rate, such that the plasma is easier to ignite and be maintained there, explaining the preferential location of the plasma reflected through an asymmetric width.

In present study, the global plasma expansion is of interest as well as the influence of non-uniform/asymmetric surface properties. The parallel plate experiments in [9], [10] were typically conducted with gaseous gaps of 0.6 to 1.2 mm. The applied voltage was sinusoidal at frequencies around 100 to 140 kHz. The dielectrics were polymers (PEN – polyethylene naphthalate) foils, 0.1 mm thick. The used gas mixtures reported were relevant for thin film deposition. The main components were either argon/oxygen or argon/nitrogen (for both roughly 80/20 % of the gas inflow). Experiments in the latter reports that considered curved electrodes [11] used the same dielectric foil. The gas gap was 0.6 mm and the discharge was operated at approximately 200 kHz. The electrodes were identical and had a radius of 120 mm. The recent experiments [12] were conducted in the same setup, with a variety of dielectric foils related to the etchability of those foils. Argon/oxygen gas mixtures were used. Within the same frame work [12], the plasma has been investigated under dual frequency excitation (the aforementioned low frequency and 13.56 MHz radio frequency) where a slightly different roll-to-roll setup has been used [13], [14]. There the gaseous gap was of the same order, the low frequency component was 200 kHz and the dielectric foil is also the same. Argon/oxygen gas mixtures were used. The electrodes were asymmetric. The top electrode had a radius of 60 mm and the bottom electrode is flat. This latter setup will actually be presented here by modelling. A schematic is shown in Figure 10.1 [13], [14].

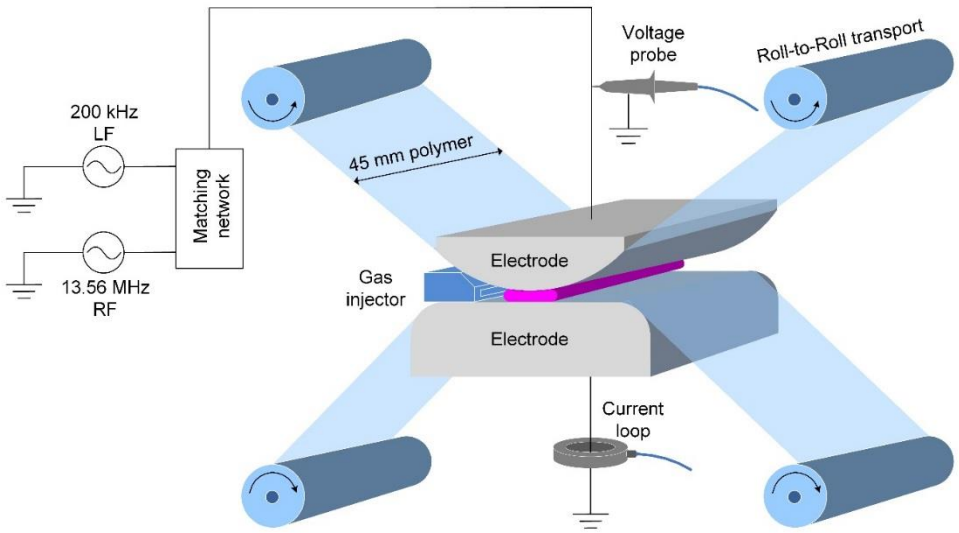


Figure 10.1. Schematic of the roll-to-roll plasma reactor used for experiments related to dual frequency excitation [13], [14], i.e. the setup of which two-dimensional modelling results will be presented in this chapter (with single low frequency excitation).

In this chapter are reported two-dimensional models after the above experimental setups with curved electrodes. The discharge gas is argon. The gas temperature is assumed constant at 450 K and the pressure at 1 atm. The applied voltage is sinusoidal with a 1 kV amplitude at 200 kHz applied to the top electrode, the bottom electrode is grounded. The (smallest) gas gap is 1 mm and the (smallest) dielectric thickness is 0.1 mm, having a dielectric constant of 3.4. The electrode radius for the top electrode is 60 mm and the bottom electrode is flat. The used secondary electron emission coefficients (0.01 or ranging from 0.01 to 0.07) are stated when models are reported. The argon chemistry description consists of a reduced amount of reactions, as discussed in section 5.2.3. Excitation, direct ionization, regular metastable-metastable ionization, atomic to molecular ion conversion, dissociative recombination, radiative decay and stepwise ionization are included. The models are initialized with low densities (see Table 3.1). The construction of the two-dimensional grid is done by using the bipolar coordinate system, described in detail in chapter 4. Here a brief summary is given. The model is created within the coordinate ranges $\tau \in [0, \tau_E]$ and $\sigma \in [\sigma_0, 2\pi - \sigma_0]$ given by

$$\tau_E = \operatorname{acosh}\frac{b}{R_E} \tag{10.1}$$
(4.3.3)

$$\sigma_0 = 2\operatorname{atan}\frac{\alpha}{l}, \qquad l \geq 0 \tag{10.2}$$
(4.3.5)

where $b = d_g/2 + d_\epsilon + R_E$ (equation 4.1.1) is the electrode center, $R_E$ the electrode radius, $d_g$ the gap size, $d_\epsilon$ the dielectric thickness, $\alpha^2 = b^2 - R_E^2$ (equation 4.3.4) the location of the foci of the coordinate system and $l$ the model width. The dielectric foil profile is given by

$$\tau_\epsilon = 2\operatorname{atanh}\frac{d_g}{2\alpha} \tag{10.3}$$
(4.3.6)

$$\tau_{\epsilon,flat} = 2\operatorname{atanh}\frac{d_\epsilon}{\alpha} \tag{10.4}$$
(4.3.10)

for the top and bottom electrode respectively. The dielectric do not cover the electrodes uniformly (see Figure 4.6) due to the constraints of the orthogonal coordinate systems as used by PLASIMO. However the main interest lies in the plasma formation and expansion due to the inhomogeneous electric field, which is still true despite non-uniform coverage of the electrodes by the dielectric. The global mechanisms can still be investigated. Here the bipolar coordinates are projected to a Cartesian representation by

$$x(\sigma, \tau) = -\alpha\frac{\sin\sigma}{\cosh\tau - \cos\sigma} \tag{10.5}$$
(4.3.7)

$$y(\sigma, \tau) = \alpha\frac{\sinh\tau}{\cosh\tau - \cos\sigma} \tag{10.6}$$
(4.3.8)

The model exists on $y \geq 0$ only. See also the discussion in section 4.3.1 especially, before construction of this asymmetric model after this brief description.

First the modelling results will be presented globally and compared to one-dimensional modelling, as used in all other chapters. Then the plasma expansion and width is considered with both uniform and

non-uniform surface properties. Finally the validity of the model with respect to the open boundaries in particular are discussed briefly.

## 10.2. Overview and comparison to one-dimensional modelling

Two model types are considered. One with a fixed value for the secondary electron emission coefficients (chosen 0.1) of all argon minority species $p$ and one with an asymmetric profile over the dielectric foil (ranging from 0.01 to 0.07). The models with fixed values are fully symmetric over the $y = 0$ axis, such that those models can be modelled on $\sigma \in [\sigma_0, \pi]$ instead of $\sigma \in [\sigma_0, 2\pi - \sigma_0]$ to save on computational time (see also section 4.4 for further details). For the asymmetric profile the following (step) function is used

$$\gamma_p(\sigma, \tau) = (\gamma_{max} - \gamma_{min}) \left[1 + \exp\left(k \frac{\pi - \sigma}{\pi - \sigma_0}\right)\right]^{-1} + \gamma_{min}, \qquad \tau = \tau_\epsilon \vee \tau = \tau_{\epsilon,flat} \qquad (10.7)$$

where $\gamma_{min} = 0.01$, $\gamma_{max} = 0.07$ and $k = 10$ is a chosen constant to determine the sharpness of the step. The grid smoothly resolved this function. In both models the two dielectrics are equal in their electron emission coefficients. Figure 10.2 shows the profile $\gamma_p(\sigma)$ for a model width $l = 30$ mm, which was the width used for the non-uniform model. The width for the half model with fixed secondary electron emission coefficients was 50 mm. In this section the latter model will be presented. The non-uniform model appears in section 10.3.

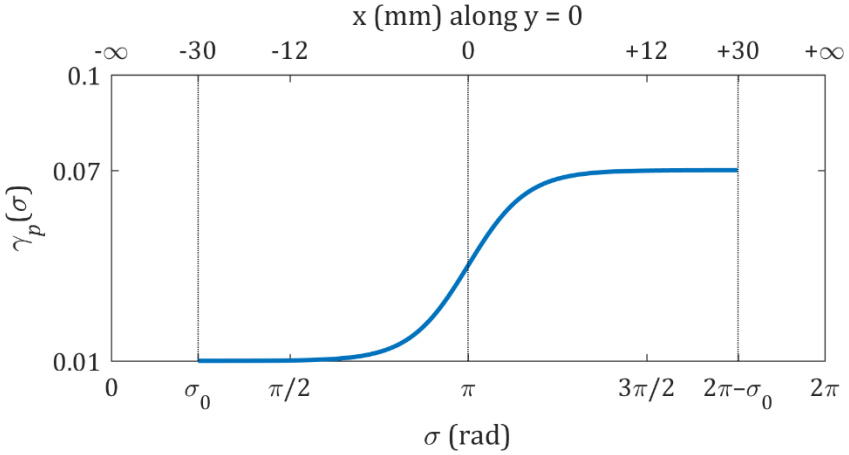


Figure 10.2. The profile used for the secondary electron emission coefficients on both dielectric for the model with non-uniform surface properties. The, to $\sigma$, corresponding model width at $y = 0$ is also displayed (top x-axis).

The regular – with uniform secondary electron emission – two-dimensional model is shown first. Figure 10.3 shows the steady state current characteristics. At the current peak maxima the typical glow structure was always observed. Figure 10.4 shows the spatial electron density at that instant. A thin positive column and negative glow is observed. The electrodes are asymmetric thus asymmetry in the current between positive and negative half cycles can be expected. The observed divergence is however seemingly minor with $+5.61$ and $-5.65$ A observed. This results in a ratio of 1.007. The ratio between the full model dielectric arc lengths is higher, approximately 1.04. In 1D modelling the start of the secondary current peaks under similar conditions were also observed (see section 5.1), however the first peak was more pronounced relative to the secondary peaks. Here, in the 2D model, the first and secondary peaks are more near to each other in current amplitude.

The ratio between positive and negative half cycle currents will be revisited in section 10.3. The relative first peak amplitude will be revisited later also. Figure 10.4 shows much more interesting

features than just a positive column and negative glow in the spatial electron density, those will be discussed in section10.4.

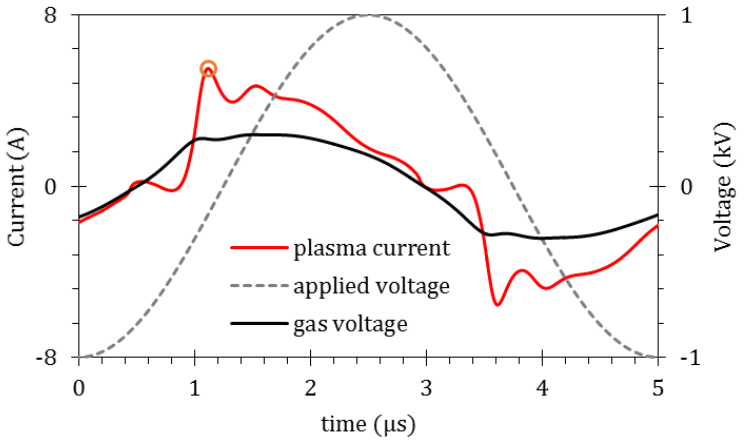


Figure 10.3. The current and voltage characteristics for the uniform model during one steady state voltage cycle. The current magnitude is corrected for having modelled only half the model.

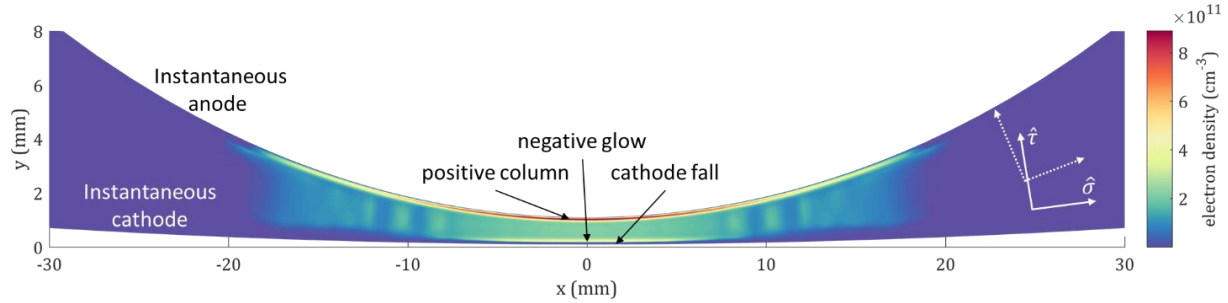


Figure 10.4. The spatial electron density at the moment of maximum current for an excerpt of the uniform (half) model. The right side is replicated from the left side data to better represent the actual geometry of interest. The y to x axis ratio is 3:2. The direction of the unit vectors of the bipolar coordinates used are also sketched on the right.

The above model is compared to a steady state 1D model (see section 5.1 for its first occurrence). In order to do so, the electron density is integrated over the $\sigma$ coordinate and normalized. This direction was indicated in Figure 10.4. Figure 10.5 shows the results corresponding to the IV characteristics of Figure 10.3 and the equivalent 1D model. For this representation of the 2D model the sheath edge has also been calculated (see equation 5.1).

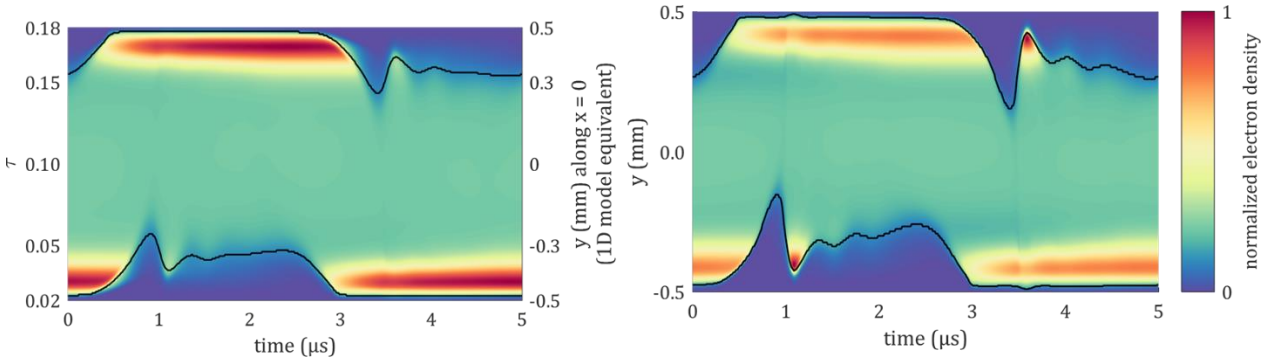


Figure 10.5. Comparison of the glow structure through the electron density between the 2D model (left), to the 1D model results (right), through integrating the 2D model over the $\sigma$ direction of the bipolar coordinate system $(\sigma, \tau)$ and subsequent normalization. The equivalent distances in mm is shown on its right axis. The color bar (right) is shared.

Between the 2D and 1D model compared in Figure 10.5 the input was equivalent. The presented 1D results used the same reduced chemistry scheme as mentioned earlier (see also section 5.2.3). In the 2D model the rate coefficient of radiative decay was assumed to depend on the local gap size (see section 3.2), resulting in a lower metastable destruction rate at larger gap sizes. In the 1D model this destruction rate, considering radiative decay, is constant and corresponds to the highest value in the 2D model. The electron density has its maximum in the positive columns in the 2D model. For the 1D model this is in the negative glow. The sheath edge show globally the same behavior and the breakdown is shown to occur at the same time. Figure 10.6 more closely compares the sheath edge against each other. The cathode sheath is overall thinner for the 2D model expect for the first negative glow peak itself. Overall the 2D sheath edge is less sharp in the peak features.

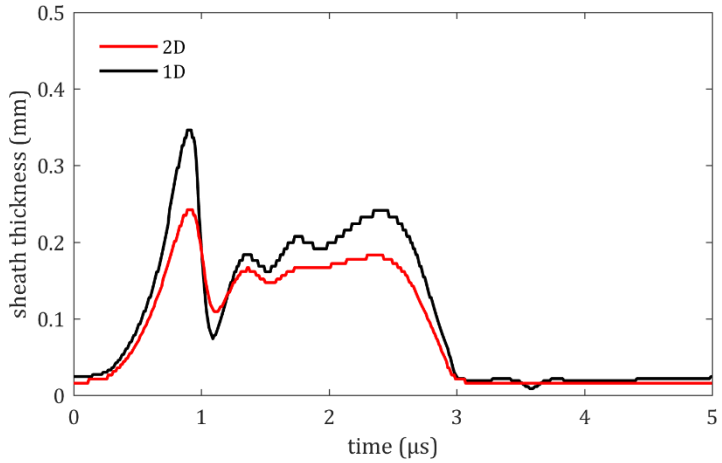

Figure 10.6. Temporal comparison of an effective sheath edge in the 2D model to that of the equivalent 1D model.

The above comparisons showed that the discharge structure is equal between 1D and 2D modelling. To explain the observed differences, the full 2D model must be considered, as is done in the next section. Based on the agreement between the global behaviors, the 1D modelling reported in previous chapters is judged representative of the higher dimensional discharge.

## 10.3. The plasma width

First the plasma width is considered for the model with uniform secondary electron emission during the voltage cycle shown in Figure 10.3. To do so the electron density is now integrated over the $\tau$ coordinate. This direction was indicated in Figure 10.4. In order to systematically determine a plasma width, the plasma edge is calculated analogous to the sheath edge (see equation 5.1). Figure 10.7 shows this plasma edge and the corresponding (half) plasma width at the end of the voltage cycle, indicated on the right axis. The occurrence of the first negative glow is indicates as well as the abrupt decrease of the positive column preceding it. Stripe-like features are also observed in this representation of the plasma, those are attributed to the plasma expansion phases in the first few half cycles which will be addressed later in more detail.

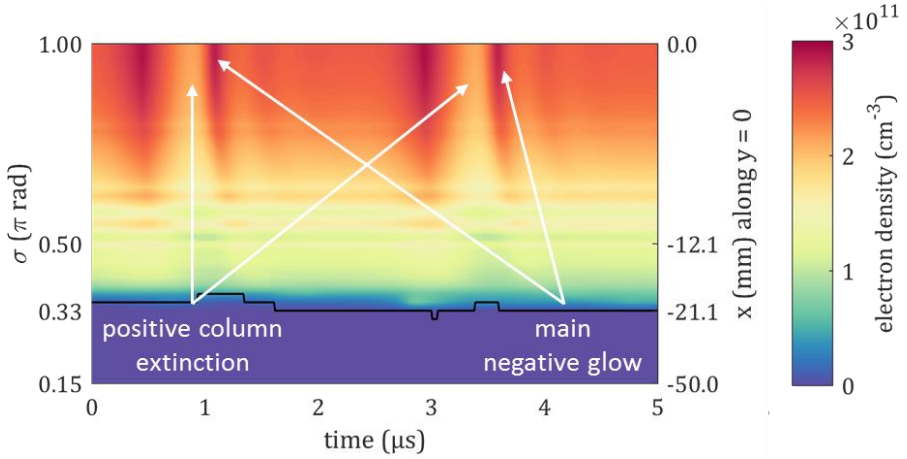


Figure 10.7. The electron density integrated over the $\tau$ direction of the bipolar coordinate system $(\sigma, \tau)$. The equivalent (half) widths are indicated on the right y axis. Two main features are indicates to help relate this figure to Figure 10.3 and the left figure of 10.5. The solid line represents the plasma edge.

Knowing the full plasma width and thus the discharge area of approximately 42 mm × 1 m, allows the comparison of the current in the 2D model to that of the 1D model. In the 2D model the first current peak was less pronounced relative to secondary peaks compared to the 1D model. Figure 9.8 compares the IV characteristics through the current density. Good agreement is shown in both the gas voltage and global current behavior. The 2D modelled current is much less for the individual peaks, the first peak more significantly so.

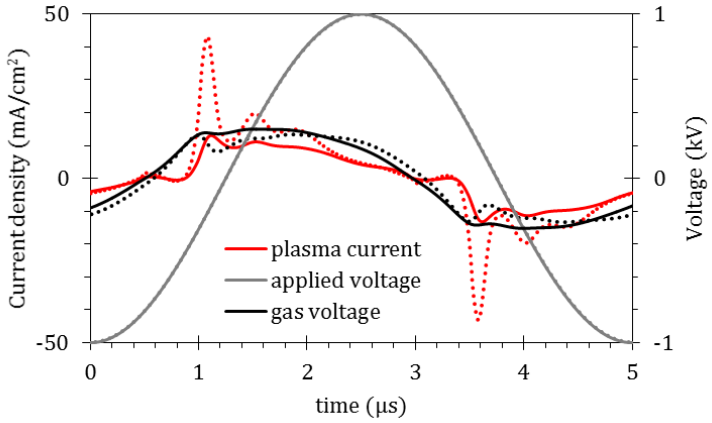


Figure 10.8. Comparison of the current and voltage characteristics between the 2D model with uniform electron emission coefficients (solid lines) and an equivalent 1D model (dotted lines).

Furthermore, knowing the (half) width in the bipolar coordinates, $\sigma = 0.33\pi$, allows calculation of a more representative discharge area and the ratio therein considering the top and bottom dielectric. Section 10.1 reported the current peak ratio between the positive and negative half cycle to be 1.007 while the full model dielectric widths yielded a ratio of 1.04. This latter value used $\sigma \in [\sigma_0, 2\pi - \sigma_0]$. Using $\sigma \in [0.33\pi, (2 - 0.33)\pi]$ instead yields 1.016, which is lower. Still it is not as low as the ratio in the current.

Two 2D models were introduced for this chapter. One with uniform secondary electron emission, of which results are shown up till now, and one model with non-uniform electron emission as described by equation 10.7 and in Figure 10.2. Figure 10.9 shows the plasma width for the latter model similar

to Figure 10.7, Figure 10.10 shows the complementary IV characteristics and Figure 10.11 shows the spatial electron density at the instant of maximum current. This moment is also indicated in Figure 10.9. In considering Figure 10.9 it should be realized that the positive column and the negative glow were more equal in density as shown in Figure 10.12, this is reflected by the less pronounced electron density corresponding to the positive column and its extinction (analogous to the indications in Figure 10.7) in Figure 10.9. Then, it is also seen that the negative glow already occurred in the part where the secondary electron emission coefficient was higher (top half of Figure 10.9), before the indicated current maximum. Figure 10.11 indeed shows that the negative glow is located in the low electron emission half of the model at the moment of maximum current. The current characteristics shown in Figure 10.10 are overall smoother. Overall for this model the chosen secondary electron emission coefficients where lower than the uniform model. Also in 1D modelling for the same conditions and secondary electron emission coefficient of 0.07, the multi-peaks was slightly less pronounced compared to 0.1 (see dotted lines in Figure 10.8) and for 0.01 only a small shoulder was observed.

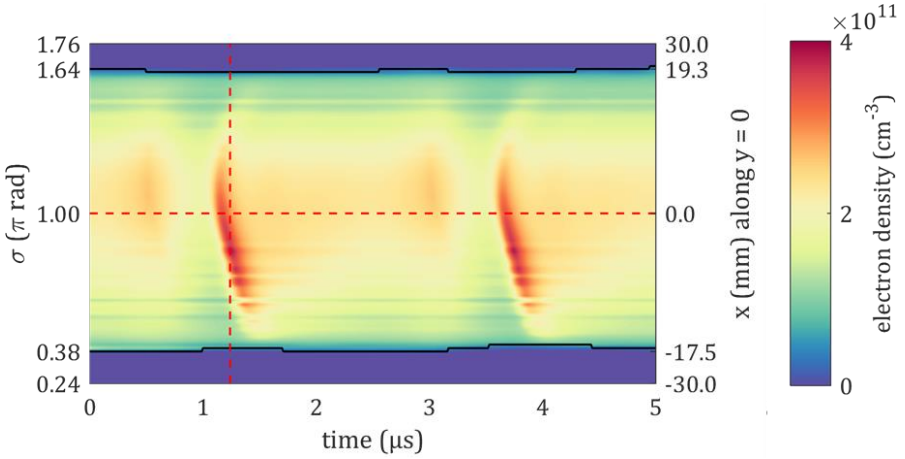


Figure 10.9. The electron density integrated over the $\tau$ direction of the bipolar coordinate system $(\sigma, \tau)$. The equivalent widths are indicated on the right y axis. Data is from the model with non-uniform secondary electron emission coefficients (see equation 10.7). The center and the moment of maximum current are indicated (horizontal and vertical line respectively).

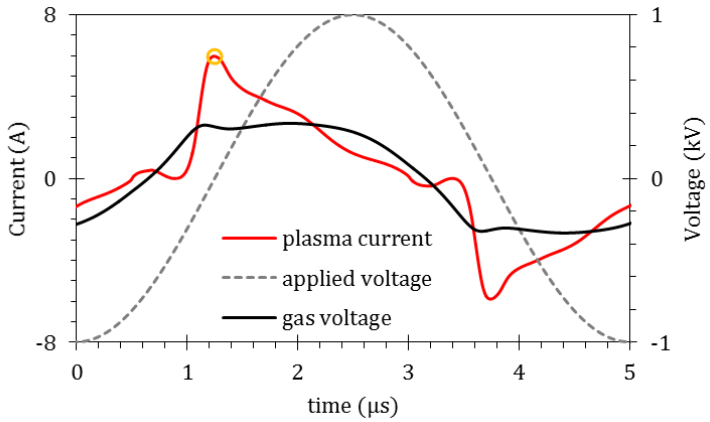


Figure 10.10. The current and voltage characteristics for the non-uniform model during one steady state voltage cycle. Indicating the point of maximum current at which Figure 10.11 is taken.

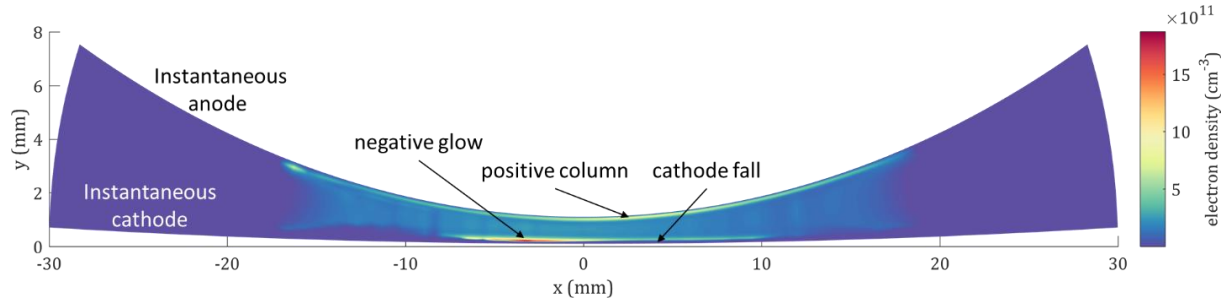


Figure 10.11. The spatial electron density at the moment of maximum current (as indicated in Figure 10.9 and 10.10) for the full non-uniform model. The y to x axis ratio is 3:2.

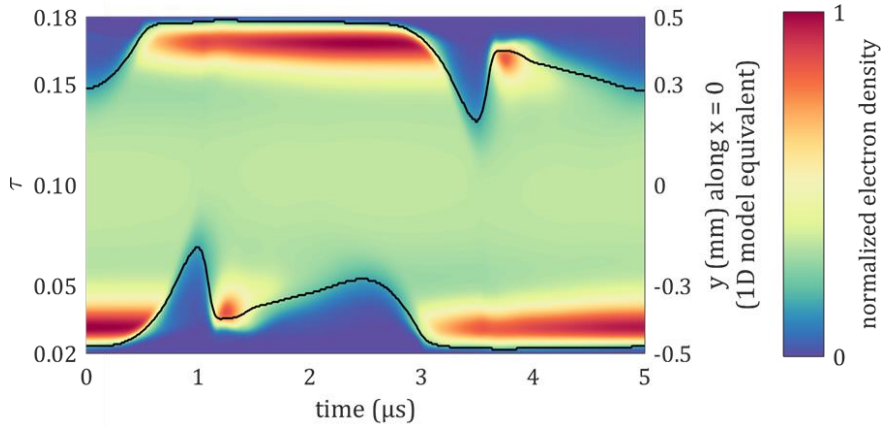


Figure 10.12. The electron density integrated over the $\sigma$ direction of the bipolar coordinate system $(\sigma, \tau)$ and normalized. The equivalent distances are indicated on the right y axis. Data is from the model with non-uniform secondary electron emission coefficients.

The plasma widths are consistent between the two 2D models. Higher secondary electron emission coefficients $\gamma_p$ yielding higher widths. In terms of approximate half plasma widths, the uniform model with $\gamma_p = 0.1$ yielded 21.1 mm, the non-uniform model yielded 19.3 mm at the $\gamma_p = 0.04..0.07$ side and 17.5 for the $\gamma_p = 0.01..0.04$ side. In experiments with an applied voltage of 1 to 1.1 kV the plasma width was estimated as 35 mm from emission measurements.

In both 1D and 2D modelling the same glow like discharge is observed. However under equal conditions the positive column was more pronounced relative to the negative glow in the 2D model whereas the 1D model had a more pronounced negative glow relative to the positive column. The first current peak in the 1D model was also more pronounced compared to secondary peaks while in the 2D model this was of the same order. It is assumed that those differences are cause by an (immediate) lateral ionization wave in the 2D model, occurring right after the negative glow and cathode fall formation, due to surface charge deposition and subsequent reduction of the electric field while the lateral electric field stays strong enough to maintain the glow. In the 1D model there is no lateral electric field such that the negative glow continues to develop along the same path instead of a different, preferential, path. The lateral expansion in the 2D model is explored in section 10.4.

## 10.4. Plasma density evolution

The plasma electron density evolution will be presented during single half cycles for both the uniform and non-uniform models. The full plasma formation, from the first breakdown towards the full plasma width, will be considered for the non-uniform model also.

### 10.4.1. Single half cycle

The spatial plasma evolution during one steady state half cycle is shown in Figure 10.14 for the uniform model. Figure 10.13 indicates the chosen frames. Before the negative glow formation, first the positive column together with a contracted bulk is observed (Figure 10.14, frame 0.95 µs). The gas voltage increases still, the electric field gets stronger, the electrons gain energy and cause ionization, the plasma expands towards the (new) cathode (1.02 µs). This continues and the negative glow is formed and expands along the dielectric surface (1.11 µs). Surface charge is deposited and the electric field reduced in the initial negative glow area (smallest gap), the negative glow extinguishes there but continues to expand laterally (1.16..1.26 µs). At this point this can – and does in this case – reoccur. Each subsequent negative glow formation, within the same half cycle, is weaker. Eventually the negative glow completely extinguishes (2.65 µs). The polarity is changed and electrons from at the previous anode traverse the gap (2.85 µs), extinguishing the previous positive column and creating a new one (3.10 µs) until the plasma bulk contracts again (3.38 µs), allowing the electric field to build up again and start the cycle anew.

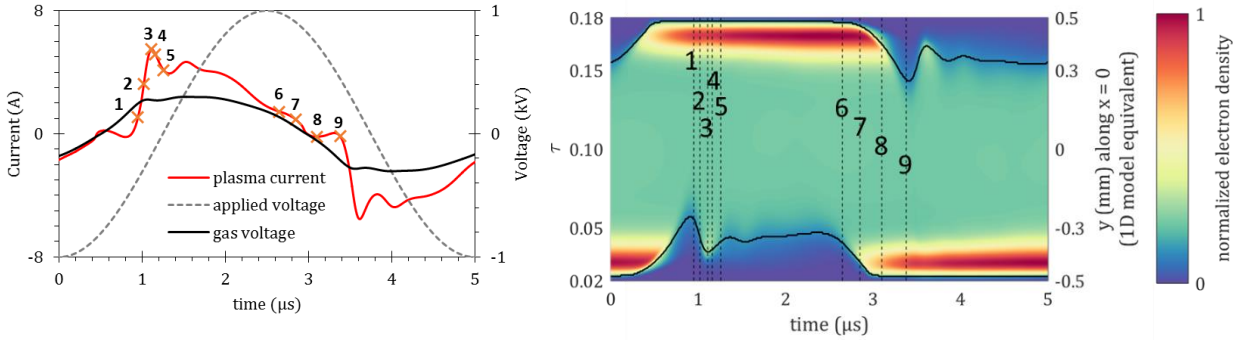


Figure 10.13. Time references to the current (left) and glow structure (right) of the frames in Figure 10.14 (uniform model).

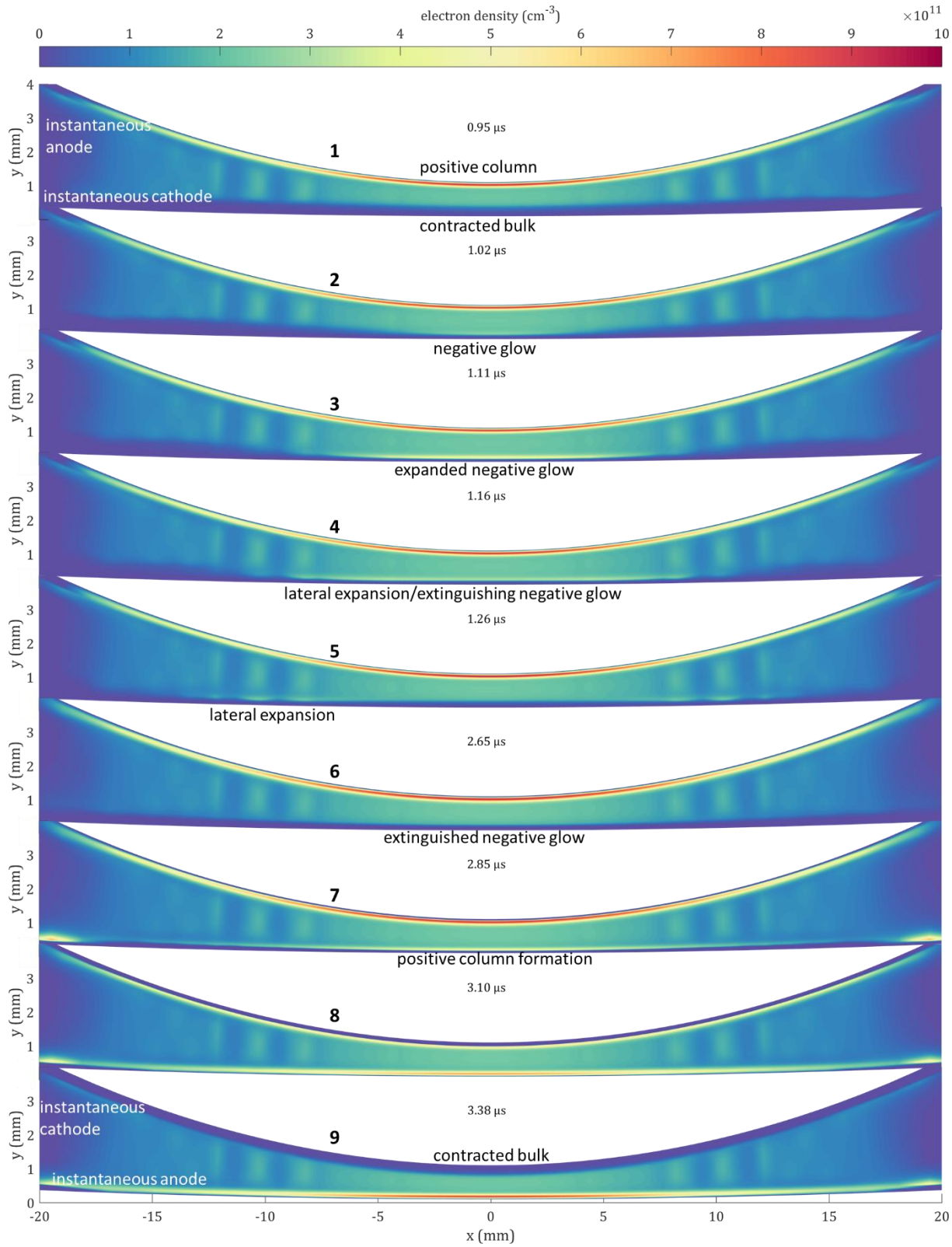


Figure 10.14. Plasma evolution of the uniform model starting from a contracted bulk (top) and showing the negative glow (1st peak only), lateral expansion, negative glow extinction and eventual positive column formation (bottom) with y:x, 3:2.

Figure 10.16 shows the evolution for the non-uniform electron emission model. Figure 10.15 indicates the chosen moments in time with respect to the current characteristics and temporal glow structure. The positive column is seen to be off center (Figure 10.16, frame 0.95 µs). The negative glow is first formed in the higher electron emission area (1.11 µs) after which the lateral expansion again follows, towards both the smaller gap and the larger gap distances (1.31 µs). The negative glow front that passes the smaller gap and goes into the lower electron emission area increases in density, this is attributed to the local growth of surface charge. This process is assumed slower in the low electron emission area, causing the electric field that warrants further growth of the local negative glow to decrease at a slower rate such that the negative glow is indeed able to grow still instead of only being able to expand laterally. The negative glow expands until it stays rather stationary (1.46..2.01 µs) until it is extinguished completely (2.41 µs) after which the positive column starts to form on the other side with a preference of the high electron emission area (3.05 µs). Eventually a positive column is formed along the whole dielectric (3.49 µs) and the cycle is repeated. The next negative glow also starts at the high secondary electron emission coefficients (3.60 µs).

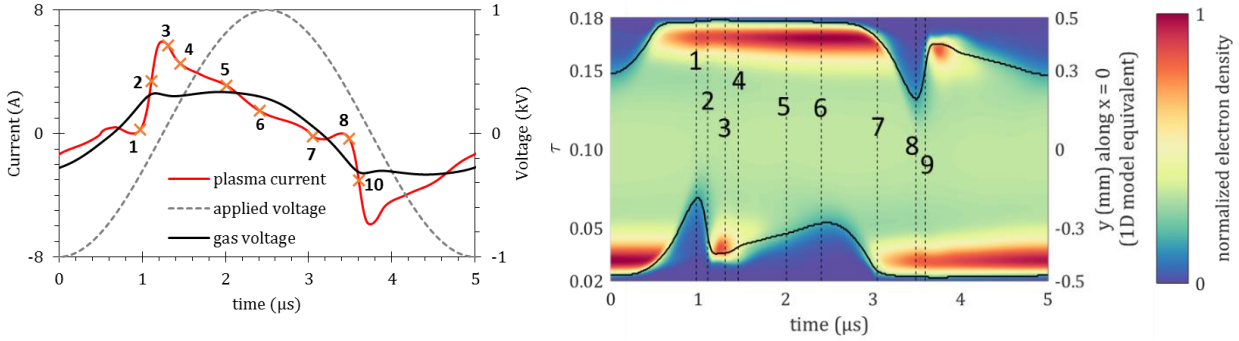


Figure 10.15. Time reference to the current (left) and glow structure (right) of the frames in Figure 10.16. Data is of the non-uniform electron emission model.

Considering that the negative glow evolution of the non-uniform model was due to a single negative glow formation, whereas the uniform model did have a multi peak behavior, the (single/first) negative glow existed for much longer – as a crude indication based on Figure 10.16 and 10.14; 1.11..2.01 µs against 1.02..1.26 µs for the non-uniform and uniform model respectively.

For the non-uniform model, the smoother current characteristics are explained due to the longer lasting expansion of the negative glow into the smaller gap and the lower secondary electron emission area.

Both models showed the occurrence of highly localized spots near the plasma periphery, mostly connected to the formation of the positive column. Experimentally the occurrence of such spots is also observed but the analogy is not necessarily clear.

The results discussed up till now in this chapter have also systematically shown triple like features or channels of high and low electron density out of the small gap areas. This has not yet been addressed and is a main topic of the next subsection.

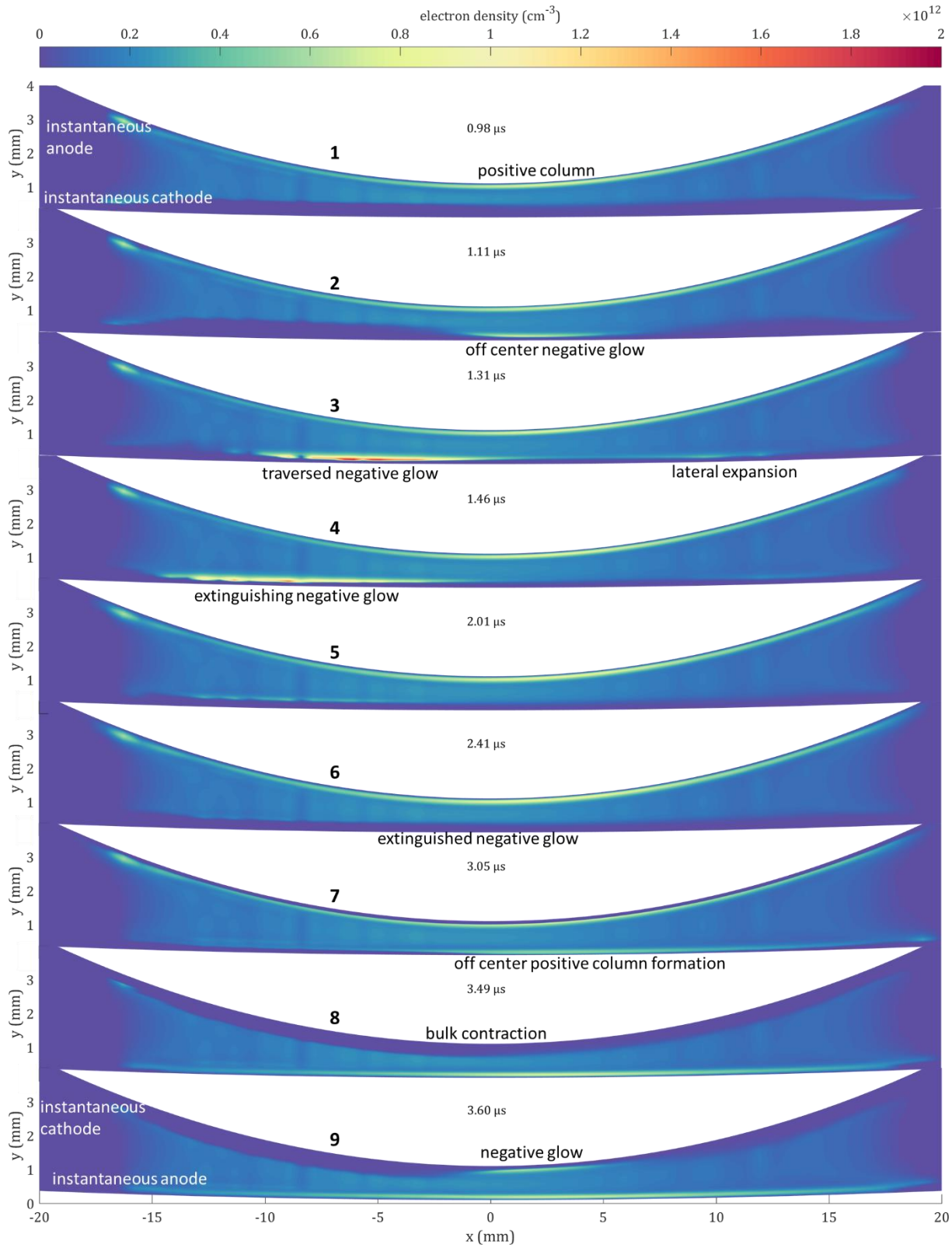


Figure 10.16. Plasma evolution of the non-uniform model starting from a contracted bulk (top), showing the negative glow (1st peak only), lateral expansion and eventual positive column formation and the next negative glow (bottom) with y:x, 3:2.

### 10.4.2. Towards steady state

Chapter 7 considered the various breakdown mechanisms starting from a very first breakdown up to steady state based on 1D modelling. That discussion validated that the models starting from low densities do have physical meaning across the whole modelled time range. The 2D models inherently required the same modelling approach (starting with low densities). Here the spatial averaged density evolution and the temporal plasma width, similar to Figures 10.7 and 10.9, will be reported over the full modelled time range of the non-uniform model only. Figure 10.17 shows this plasma width. In total 17 breakdowns are seen. Horizontal lines indicate the time instants at which the spatial electron density is reported in Figure 10.18. It is seen that the eventual width is reached after multiple breakdowns. Figure 10.18 shows that the spatial plasma profile up to a certain width is still visible upon further expansion during the next half cycle. The electron density does not reduce significantly at the plasma perimeter. Once the subsequent breakdown occur the plasma is able to form over this whole area and expand further. The individual expansions were explained in section 10.4.1. That the electron density does not reduce to zero on the plasma perimeter is assumed to be due to memory effects facilitated by low energy requiring (or energy independent) ionization processes (metastable-metastable ionization) and is assumed analogous to the formation of the positive column (see also chapter 6 on the role of metastable-metastable ionization). The occurrence of non-uniform electron density on subsequent expansion, i.e. the vertical channels that are observed at the perimeter after each expansion with reduced electron density, are assumed to be due to local reduction of the electric field due to volume charge already – still – present. The expansion itself is assumed mainly due to still high electric fields near the dielectric boundaries as described in section 10.4.1, allowing the negative glow to facilitate the plasma expansion. It is seen that those channels last multiple half cycles and less long at the high secondary electron emission coefficient area (right side of Figure 10.17). This is assumed to be due to the higher electron source at the wall when the negative glow passes those channels upon lateral expansion.

## 10.5. Conclusions

Two-dimensional modelling results of an argon dielectric barrier discharge in a roll-to-roll plasma reactor with non-homogenous electric field were presented both for uniform and non-uniform secondary electron emission across the dielectric surfaces. The uniform electron emission modelling was compared to a one-dimensional model. Overall the same discharge characteristics were seen. In the two-dimensional model the first current peak was lower in magnitude relative to secondary current peak characteristics compared to the one-dimensional model. This is assumed to be due to the non-zero lateral electric field in the two-dimensional model allowing the negative glow to develop along a preferential path created by this lateral electric field. In the two-dimensional models the lateral expansion of the negative glow causes the plasma to reach an eventual width over multiple half cycles. This width is observed to increase with the secondary electron emission coefficient, as the plasma is now maintained also at larger gap sizes due to higher secondary electron yields and subsequent surface charge. The non-uniform secondary electron emission model showed that the breakdown starts away from the smallest gap, in the high electron emission area. The negative glow lateral expansion into the lower valued secondary electron emission area caused the negative glow to exist longer in turn causing the current characteristics of the latter model to be more smooth.

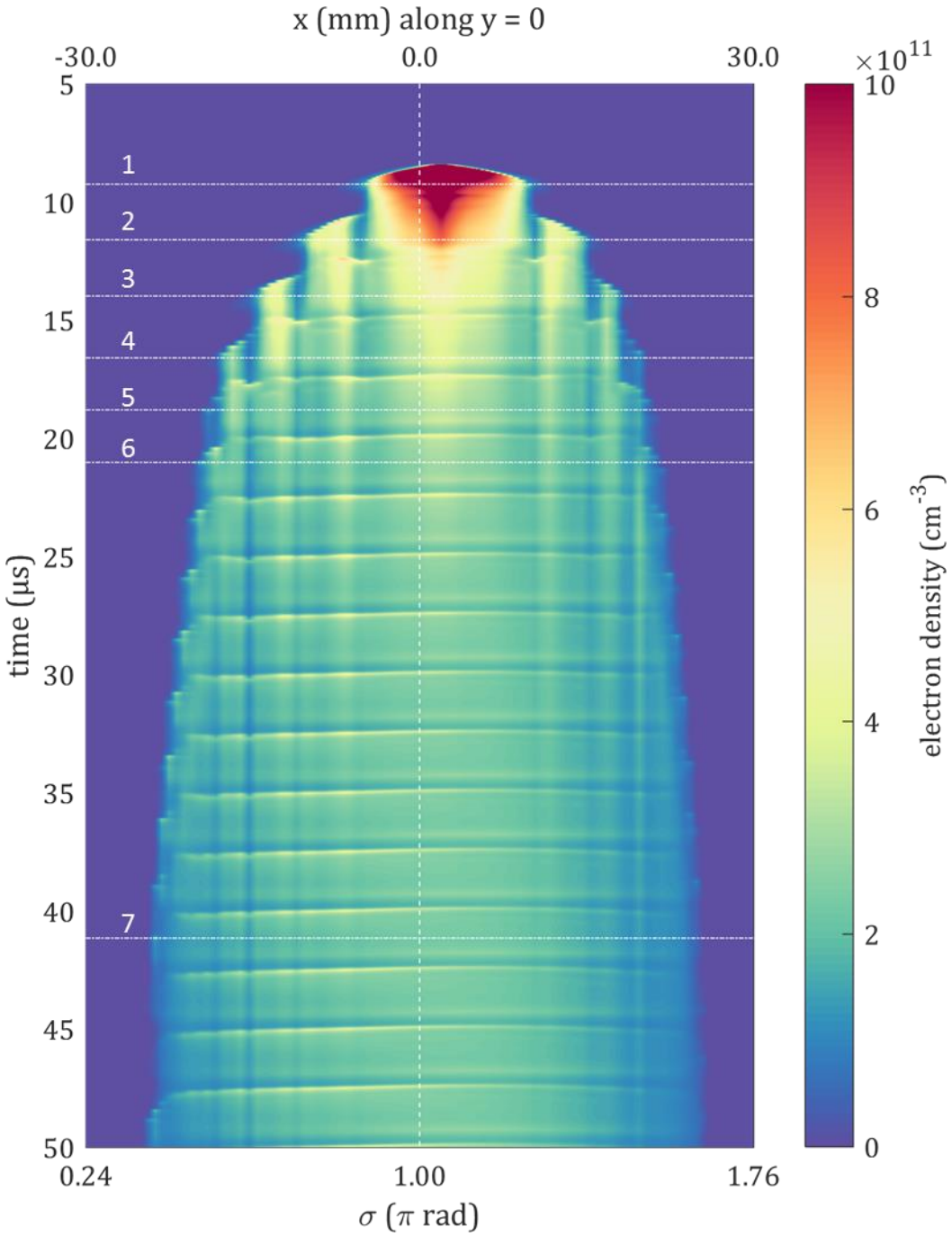


Figure 10.17. Evolution of the plasma width for the full simulation of the non-uniform model by integrating and averaging over the $\tau$ direction of the bipolar coordinate system $(\sigma, \tau)$. The vertical line indicates the center. The equivalent width in mm (top x axis) is not linear in $\sigma$ (see for example Figure 10.9). The horizontal lines indicate the time instants of Figure 10.18. The dark red area, right after the first breakdown, has electron densities in the order of $10..30 \cdot 10^{11}$ cm$^{-3}$.

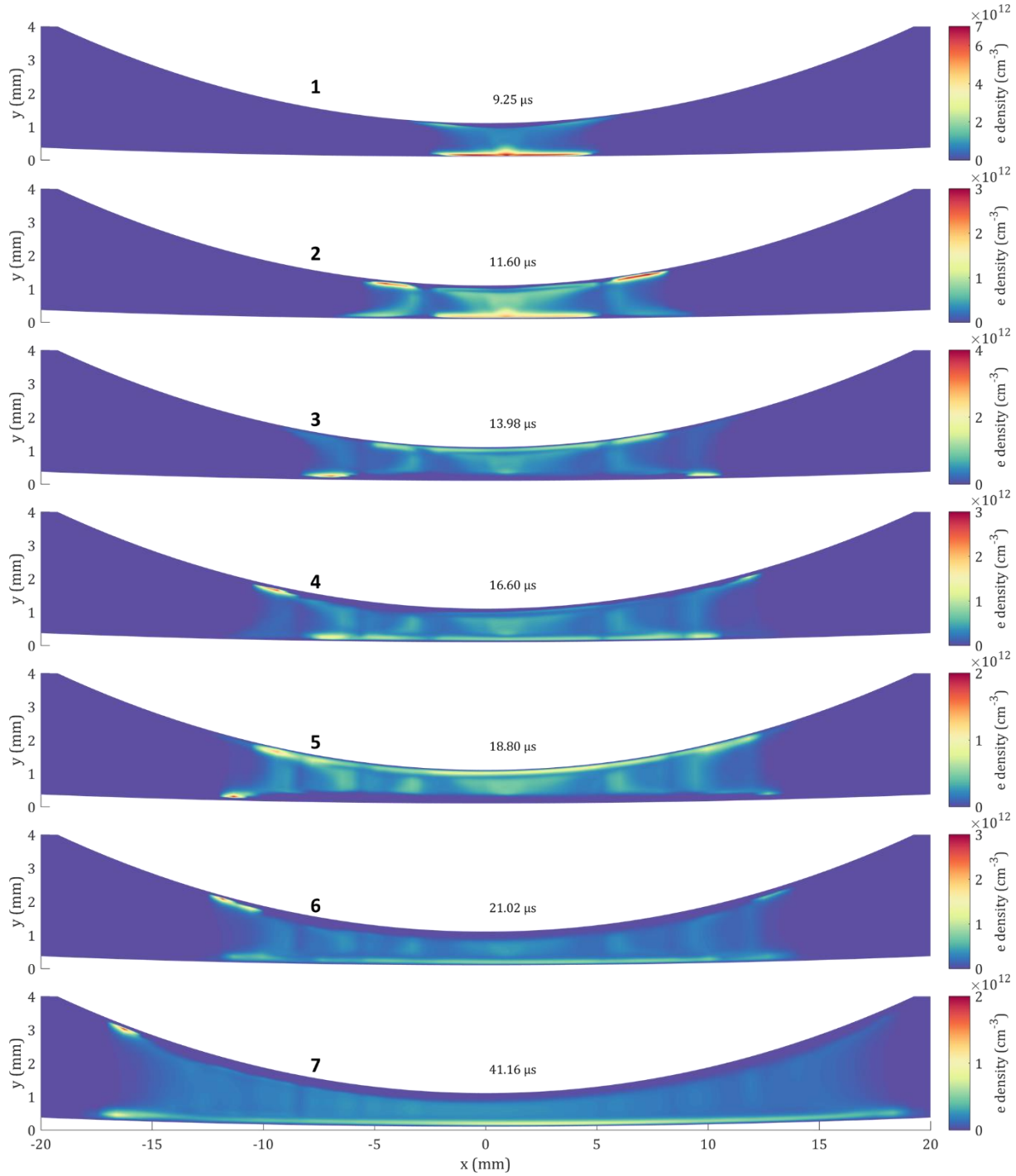


Figure 10.18. Evolution of the plasma width over the full simulation time range of the non-uniform model at specific moments as indicated in Figure 10.17.

# Part 3:
# Conclusions

# 11. Discussion, overall conclusions and recommendations

Overall the multi-peak characteristics – or in general the secondary current characteristics (after the first peak) – are a recurring theme in this thesis. The multi-peak behavior is shown to increase with (molecular) ion-electron emission coefficients, the metastable-metastable ionization rate and applied voltage for the fixed low frequency case of 200 kHz. Starting from a steady state breakdown towards the multi-peak characteristics in the negative glow at the same dielectric, one voltage cycle later; the multi-peak characteristics are explained as follows. The electric field in the cathode fall areas in stages after the initial negative glow formation mainly facilitate excitation. Higher ion-electron emission yields in this stage cause more electrons to excite the argon gas. After the polarity change, the same dielectric becomes the anode where a positive column is formed through metastable-metastable ionization which does not depend on the electric field. The low electric fields trap the ion in the plasma bulk and positive column. The larger the positive column the more memory charge is accumulated which allows the gas to breakdown at lower applied voltages. Consequently the gas voltage is able to exceed the breakdown voltage again, causing the multi-peak behavior. From this explanation, the first cause is the creation of excited atoms in the cathode fall areas.

## 11.1. Discussion (experimental current characteristics)

Unfortunately no comparison of (low frequency) modelled current characteristics to experimental ones are reported, despite notions of comparisons to experimental observations through different means. Experimental current characteristics that were retrieved do not agree completely with other experimental measured plasma parameters such as the measured emission. The current characteristics showed oscillations, which are attributed to resonances in the electrical circuit, but the cause is not understood. Based on the measured emission, no multi-peak characteristics were seen. Still in the experimental current characteristics a defined first peak was always measured. All of this, combined with the comparison of the one-dimensional to two-dimensional current characteristics with the latter – which should be more realistic – losing a defined first current peak, results in that the comparison between modelled and experimental current characteristics is not trivial.

Additional experimental measurement should be conducted to facilitate such a comparison. Additionally considering the current characteristics after the first peak as are retrieved in modelling, it should be a real consideration that the model which assumes pure argon does not capture all the important mechanisms of the experimental argon discharges. The role of impurities and the plasma polymer interaction is not truly known in the experimental (*pure*) argon discharges.

## 11.2. Overall conclusions

A model for an argon atmospheric pressure dielectric barrier discharge has been made that is shown to be able to model a wide range of conditions. In creating this model, special attention has been given to the implementation of the two-dimensional grids of roll-to-roll reactors, using the bipolar coordinate system, for implementation in PLASIMO. With chapter 4 such grids should be able to be recreated reliably.

The low frequency discharge has been described in detail in chapter 5. It was found that excitation, direct ionization, metastable-metastable ionization, atomic to molecular ion conversion, dissociative recombination and radiative decay were the main processes governing the discharge characteristics under present conditions. Exclusion of stepwise ionization was shown to only influence the atomic ion density in the bulk areas without a significant impact on the discharge characteristics. Both

associative and regular metastable-metastable ionization was considered, it was shown that exclusion of the associative kind did not significantly alter the discharge characteristics other than increasing the atomic ion density throughout. This was attributed to the fast conversion rate of atomic to molecular ions at high pressure.

In general the discharge structure was found to be glow-like with a clear cathode fall, negative glow, faraday dark space, positive column and anode dark space. Chapter 6 considered a few artificial models with respect to the rate coefficient of metastable-metastable ionization. Through those models it was confirmed that metastable-metastable ionization is responsible for the existence of (pronounced, high density) positive columns. Those positive columns were found to not influence the discharge within a single half cycle, instead they influence the next half cycle through memory charge effects which cause the breakdown to occur earlier. For those discharges, multi-peak behavior was seen.

The individual breakdowns, preceding the negative glow formation, were not identified as a Townsend breakdown. Instead the discharge was considered to never extinguish completely under current conditions and to be in a state of either subnormal glow or (normal) glow. Chapter 7 did consider the very first breakdown, which was attributed to a Townsend breakdown. In this first plasma formation, multi-peak characteristics were also seen. In this case it was attributed to ionization processes taking place at the instantaneous anode, which was in contrast with the steady state multi-peak behavior.

A numerical study over a wide range of applied voltages and secondary electron emission coefficients as input parameters was conducted in chapter 8. It was seen that electron emission by atomic ions and molecular ions change the discharge in different ways. Though because of the domination of the molecular ion, the characteristics specific due to atomic ion-electron emission did not come through significantly in the discharge characteristics when considering combined ion-electron emission processes. Still based on the small atomic ion influences observed, comparison methods have been proposed to determine from experimental measurements whether or not the atomic ion and molecular ion secondary electron emission coefficients require equal or different treatment.

Chapter 9 showed that the model has been used to study both low frequency and dual frequency plasma excitation (by addition of a radiofrequency component). Spatial characteristics of the dual frequency plasma showed excellent agreements with experimental results. The discharge development is slowed down with a lower current amplitude and a longer duration.

Two-dimensional modelling results were presented in chapter 10. The overall (spatial) discharge behavior was in good agreement with experimental observations. In comparison of the two-dimensional models to the one-dimensional model results, both of which contained multi-peak behavior, it was found that the first current peak in the two-dimensional model was less pronounced compared to latter current characteristics. This was in contrast with the one-dimensional model and was explained through the lateral expansion of the negative glow in the two-dimensional model, such that the negative glow did not develop to intensities as high as in the one-dimensional models where lateral expansion is not possible.

## 11.3. Recommendations (miscellaneous)

### Argon/oxygen

When it was introduced that this study would focus on modelling argon discharges it was also noted that it could serve as a good starting point to model admixtures with argon. Indeed initially a goal was also to model argon/oxygen mixtures. However this has been troublesome, especially considering wide ranges of oxygen percentages. Various oxygen/argon chemistry schemes were considered, such as by Gudmundsson and coworkers, both involving ozone [69] and without [70] – with BOLSIG+ calculations [71] and by Moravej et al. [72] – who also uniquely describes one reaction between $Ar_2^+$ and $O_2$. The most success was achieved with the scheme from Park et al. [73], however only for very small oxygen percentages ($\leq 0.1\%$) and an actual discharge with the long lived oxygen related species at steady state was not explored. Based on infrared gas phase studies of the experimental plasma [74], it is not completely clear if such oxygen schemes should also describe ozone. Still, achieving an atmospheric pressure dielectric barrier discharge model for a wide range of argon/oxygen mixtures is of high interest due to introduced quenching mechanisms such as [73]:

$$O_2 + Ar^* \rightarrow O_2 + Ar, \qquad k = 1.0 \cdot 10^{-9}\ \mathrm{cm^3 s^{-1}}$$

$$O + Ar^* \rightarrow O + Ar, \qquad k = 8.1 \cdot 10^{-12}\ \mathrm{cm^3 s^{-1}}$$

$$O_2 + Ar^* \rightarrow O + O + Ar, \qquad k = 5.8 \cdot 10^{-11}\ \mathrm{cm^3 s^{-1}}$$

### Computational time

All the models reported in this study progressed with a very small time step (10 ps – as an indication; all presented data was logged approximately every 1-10 ns). This value is approximately what follows from the Courant-Friedrich-Lewy condition [16], [26]. However this conditions should be irrelevant as it does not apply to the semi-implicit calculations (as in the drift-diffusion code) [16]. Modifying existing user input parameters to determine the time step were very sensitive to deviations from the 10 ps steps and always resulted in instability upon breakdown from which the model could not recover. In current implementation the calculation of the time step is based on a relative change and the calculated time step is proportional to the maximum density and depends on a maximum observed change, among others. This maximum density and maximum observed change are not particularly related to each other. It is believed that the current implementation could be improved upon by considering that the current user input parameters related to the determination of the time step are always applicable and that in the calculation of the time step two things can occur:

1. The maximum density lies elsewhere than the maximum change.
2. The maximum density and the maximum change occur at the same point.

The second case is thought of as a (fully) local calculation of the time step. Current user input related to the calculation influences both cases equally. What is proposed is a parameter that lets the user have some kind of control over when those two cases occur, the goal being for the second case to occur earlier: case two (the *local* case) should no longer only be true when

$$n_{max} = n_{at\_max\_change}$$

but when

$$\zeta \cdot n_{max} \leq n_{at\_max\_change}$$

with $\zeta$, assumed to be chosen in the order of 0.1. .1. This does not alter the current calculation, except sometimes, based on a local condition, the time step is, say, halved. As the time step used in this study required a severe limitation of 10 ps and the model was very sensitive to doubling (or less) of this value, and the instabilities always occurred on breakdown, where in present study a highly dynamic plasma area (the negative glow) is formed next to a highly stationary area with possible higher density (the positive column) – both local features – still with densities of the same order, it is thought that a brief examination of the impact of the above modifications is worth it.

# Appendix

## I. Geometry

### I.A. Derivation for equation 4.3.6

Isocurve of $\tau$

$$\tau(x,y) = \operatorname{atanh}\left(\frac{2\alpha x}{x^2+y^2+\alpha^2}\right)$$

Derivation of

$$\tau(x,0) = \operatorname{atanh}\left(\frac{2\alpha x}{x^2+\alpha^2}\right) = 2\operatorname{atanh}\left(\frac{x}{\alpha}\right)$$

Identities

$$\operatorname{atanh} x = \frac{1}{2}\ln\left(\frac{1+x}{1-x}\right)$$

$$\ln\left(\frac{a}{b}\right) = \ln a - \ln b$$

$$\ln\left(a^b\right) = b\ln a$$

Derivation

$$\begin{aligned}\tau(x,0) &= \frac{1}{2}\ln\left(1+\frac{2\alpha x}{x^2+\alpha^2}\right) - \frac{1}{2}\ln\left(1-\frac{2\alpha x}{x^2+\alpha^2}\right)\\ &= \frac{1}{2}\ln\left(\frac{x^2+\alpha^2+2\alpha x}{x^2+\alpha^2}\right) - \frac{1}{2}\ln\left(\frac{x^2+\alpha^2-2\alpha x}{x^2+\alpha^2}\right)\end{aligned}$$

$$x^2+\alpha^2+2\alpha x = (\alpha+x)^2$$

$$x^2+\alpha^2-2\alpha x = (\alpha-x)^2$$

$$\begin{aligned}\tau(x,0) &= \frac{1}{2}\ln\left(\frac{(\alpha+x)^2}{x^2+\alpha^2}\Big/\frac{(\alpha-x)^2}{x^2+\alpha^2}\right)\\ &= \ln\left(\frac{\alpha+x}{\alpha-x}\cdot\frac{1/\alpha}{1/\alpha}\right)\\ &= \ln\left(1+\frac{x}{\alpha}\right) - \ln\left(1-\frac{x}{\alpha}\right)\\ &= 2\operatorname{atanh}\left(\frac{x}{\alpha}\right)\end{aligned}$$

Q.E.D.

## I.B. $\sigma(x, y)$ and $\tau(x, y)$ for the rotated bipolar coordinate system

Section 4.3 introducing a rotated bipolar coordinate system (equation 4.3.7 and 4.3.8 and Figure 4.5). Equation 4.2.7 and 4.2.8 gave $\sigma(x, y)$ and $\tau(x, y)$ respectively, for the standard bipolar coordinate system. In order to calculate back $\sigma$ and $\tau$ values within the ranges $\sigma \in [\sigma_0, 2\pi - \sigma_0], \tau \in [-\tau_E, +\tau_E]$ (section 4.3) from the coordinates $\vec{x}$ (section 4.6) from geometries like Figure 4.5, the following formulas where used

$$\tau(x, y) = \operatorname{atanh}\left(\frac{2\alpha y}{x^2 + y^2 + \alpha^2}\right) \tag{I.B.1}$$

$$\sigma(x, y \neq \alpha) = \operatorname{atan}\left(\frac{-2\alpha x}{x^2 + y^2 - \alpha^2}\right) + n_1(x) \cdot \pi \tag{I.B.2}$$

$$n_1(x) = \begin{cases} 0, & x < -\alpha \\ 1, & -\alpha < x < +\alpha \\ 2, & x > +\alpha \end{cases} \tag{I.B.3}$$

$$\sigma(x, y = \alpha) = -2 \operatorname{atan}\left(\frac{\alpha}{x}\right) + n_2(x) \cdot \pi \tag{I.B.4}$$

$$n_2(x) = \begin{cases} 0, & x < 0 \\ 2, & x > 0 \end{cases} \tag{I.B.5}$$

Formula I.B.1 can be used for all $x$ and $y$. Formulas I.B.2 and I.B.4 do not hold for $y > \alpha$, however – within reason – this won't occur in present study as the foci and the electrode center are close to each other, $\alpha/b \approx 1$, and the model width never exceeds the electrode radius, $l < R_E$. The construction of the above equations can be considered empirical.

During present study, PLASIMO added the geometry coordinate mappings (i.e. $(x, y) \leftrightarrow (\sigma, \tau)$) as an output in the drift-diffusion model.

## I.C. Derivation of equation 4.4.3 (and 4.4.4)

Model boundaries for (a) Cartesian (b) bipolar systems:

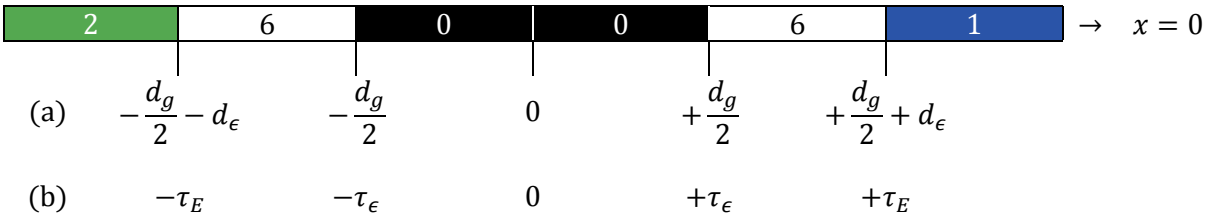


Ratio to determine the cell matrix layout (Cartesian translated to Bipolar systems):

$$\frac{d_\epsilon}{d_g + 2d_\epsilon} \to \frac{\tau_E - \tau_\epsilon}{2\tau_E}$$

Derivation of:

$$\frac{\tau_E - \tau_\epsilon}{2\tau_E} \approx \frac{d_\epsilon}{d_g + 2d_\epsilon}$$

Series expansions:

$$\operatorname{atanh}(x = 0) = x + \frac{x^3}{3} + \frac{x^5}{5} + O(x^7)$$

$$\operatorname{acosh}(x = 1) = \sqrt{2x - 2} - \frac{(x-1)^{3/2}}{6\sqrt{2}} + O\left((x-1)^{5/2}\right)$$

Derivation:

$$\frac{\tau_E - \tau_\epsilon}{2\tau_E} = \frac{1}{2} - \frac{\tau_\epsilon}{2\tau_E} = \frac{1}{2} - \frac{2\operatorname{atanh}(d_g/2\alpha)}{2\operatorname{acosh}(b/R_E)} \approx \frac{1}{2} - \frac{d_g/2\alpha}{\sqrt{2b/R_E - 2}} \quad \text{(i)}$$

$$\frac{d_g/2\alpha}{\sqrt{2b/R_E - 2}} \cdot \frac{R_E}{R_E} = \frac{d_g R_E}{2\alpha} \cdot \frac{1}{\sqrt{2bR_E - 2R_E^2}} \quad \text{(ii)}$$

$$\sqrt{2bR_E - 2R_E^2} = \sqrt{d_g R_E + 2d_\epsilon R_E} \quad \text{(using eq. 4.1.1)}$$

$$\frac{d_g R_E}{2\alpha} = \frac{d_g R_E}{2\sqrt{b^2 - R_E^2}} \quad \text{(using eq. 4.3.4)}$$

$$\sqrt{b^2 - R_E^2} = \sqrt{\frac{d_g^2}{4} + d_\epsilon^2 + d_g d_\epsilon + d_g R_E + 2d_\epsilon R_E} \quad \text{(using eq. 4.1.1)}$$

Continuing from (ii):

$$\frac{d_g R_E}{2\alpha}\cdot\frac{1}{\sqrt{2bR_E-2R_E^2}}=\frac{d_g R_E}{2\sqrt{\frac{d_g^2}{4}+d_\epsilon^2+d_g d_\epsilon+d_g R_E+2d_\epsilon R_E}}\cdot\frac{1}{\sqrt{d_g R_E+2d_\epsilon R_E}} \qquad \text{(iii)}$$

$$\left(\frac{d_g^2}{4}+d_\epsilon^2+d_g d_\epsilon+d_g R_E+2d_\epsilon R_E\right)\cdot\left(d_g R_E+2d_\epsilon R_E\right)$$
$$=\frac{d_g^3 R_E}{4}+d_g d_\epsilon^2 R_E+d_g^2 d_\epsilon R_E+d_g^2 R_E^2+2d_g d_\epsilon R_E^2+\frac{d_g^2 d_\epsilon R_E}{2}+2d_\epsilon^3 R_E+2d_g d_\epsilon^2 R_E$$
$$+2d_g d_\epsilon R_E^2+4d_\epsilon^2 R_E^2$$
$$=R_E\left(\frac{d_g^3}{4}+d_g d_\epsilon^2+d_g^2 d_\epsilon+\frac{d_g^2 d_\epsilon}{2}+2d_\epsilon^3+2d_g d_\epsilon^2\right)+R_E^2\left(d_g^2+4d_g d_\epsilon+4d_\epsilon^2\right)$$
$$=R_E\left(\frac{d_g^3}{4}+\frac{3d_g^2 d_\epsilon}{2}+3d_g d_\epsilon^2+2d_\epsilon^3\right)+R_E^2\left(d_g+2d_\epsilon\right)^2$$

$$\frac{d_g^3}{4}+\frac{3d_g^2 d_\epsilon}{2}+3d_g d_\epsilon^2+2d_\epsilon^3\equiv D$$

Continuing from (iii):

$$\frac{d_g R_E}{2\alpha}\cdot\frac{1}{\sqrt{2bR_E-2R_E^2}}=\frac{d_g R_E}{2\sqrt{R_E D+R_E^2\left(d_g+2d_\epsilon\right)^2}}$$

If $R_E D \ll R_E^2\left(d_g+2d_\epsilon\right)^2$:

$$\frac{d_g R_E}{2\sqrt{R_E D+R_E^2\left(d_g+2d_\epsilon\right)^2}}=\frac{d_g}{2\left(d_g+2d_\epsilon\right)}$$

Continuing from (i):

$$\frac{\tau_E-\tau_\epsilon}{2\tau_E}\approx\frac{1}{2}\cdot\frac{d_g+2d_\epsilon}{d_g+2d_\epsilon}-\frac{d_g}{2\left(d_g+2d_\epsilon\right)}$$

$$\frac{\tau_E-\tau_\epsilon}{2\tau_E}\approx\frac{d_g+2d_\epsilon-d_g}{2\left(d_g+2d_\epsilon\right)}=\frac{d_\epsilon}{d_g+2d_\epsilon}$$

Q.E.D.

## I.D. The n-point stretch functions in PLASIMO

The n-point stretch functions $f_{(n)}(d_1, \dots, d_n, c_1, \dots, c_n, c)$ define the grid densities $d_n$ at $c_n$, the grid density is given by $1/f'_{(n)}$. The stretch function $f_{(n)}$ are given by

$$f_n(c) = c + \sum_{k=0}^{2n-1} b_k\left(c^{k+2} - c^{k+1}\right) \tag{I.D.1}$$

where the coefficients $b_k$ are solved through a set of $2n$ linear equations (1st and 2nd derivative for each $c_n$)

$$\sum_{k=0}^{2n-1} b_k\left((k+2)c_n^{k+1} - (k+1)c_n^{k}\right) = \frac{1}{d_p} - 1 \tag{I.D.2}$$

$$\sum_{k=0}^{2n-1} b_k\left((k+1)(k+2)c_n^{k+1} - k(k+1)c_n^{k^*}\right) = 0 \tag{I.D.3}$$

with

$$k^* = \max(k-1, 0) \tag{I.D.4}$$

Examples of $f_{(n)}(d_1, \dots, d_n, c_1, \dots, c_n, c)$:

$$f_{(1)}(0,4,c) = c + \frac{3}{4}(c^2 - c) + \frac{3}{4}(c^3 - c^2) \tag{I.D.5}$$

$$f_{(1)}(1/2,4,c) = c - \frac{3}{2}(c^2 - c) + 3(c^3 - c^2) \tag{I.D.6}$$

$$f_{(1)}(1,4,c) = c - \frac{3}{2}(c^2 - c) + \frac{3}{4}(c^3 - c^2) \tag{I.D.7}$$

$$f_{(2)}(1/4, 3/4, 2,2,c) = c - \frac{56}{23}(c^2 - c) + \frac{304}{23}(c^3 - c^2) - \frac{576}{23}(c^4 - c^3) + \frac{384}{23}(c^5 - c^4) \tag{I.D.8}$$

The Figure below shows the functions $f_{(n)}$ (left) and the grid densities $1/f'_{(n)}$ (right).

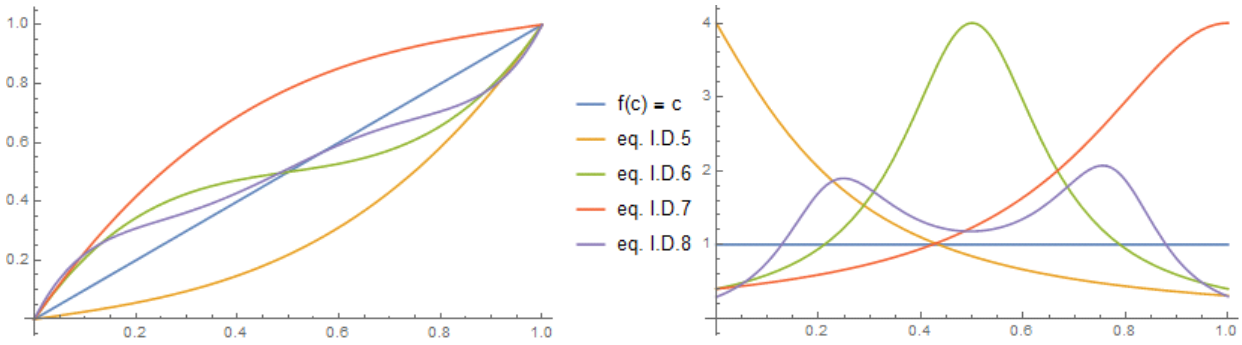

# II. The plasma current

## II.A. Plasma current calculation and cell capacitance determination for model batches

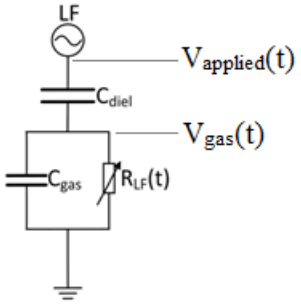


Figure II.1. Equivalent circuit of a dielectric barrier discharge. The capacitance $C_{diel}$ represents both dielectric layers (two capacitors in series) [14].

The plasma current $I_{plasma}$ is calculated by [1]:

$$V_{gas}(t) = V_{applied}(t) - \frac{1}{C_{diel}} Q(t) \tag{II.A.1}$$

$$I_{plasma}(t) = I_{total}(t) - C_{gas} \frac{dV_{gas}(t)}{dt} \tag{II.A.2}$$

$$\frac{1}{C_{cell}} = \frac{1}{C_{gas}} + \frac{1}{C_{diel}} \rightarrow C_{gas} = \frac{C_{diel} C_{cell}}{C_{diel} - C_{cell}} \tag{II.A.3}$$

Where $Q$ is the charge on a dielectric (PLASIMO model output) and the applied voltage $V_{applied}$ is PLASIMO model input (and output).

Capacitances $C_{cell}$ and $C_{diel}$ are determined from the Q-V (Lissajous) Figures:

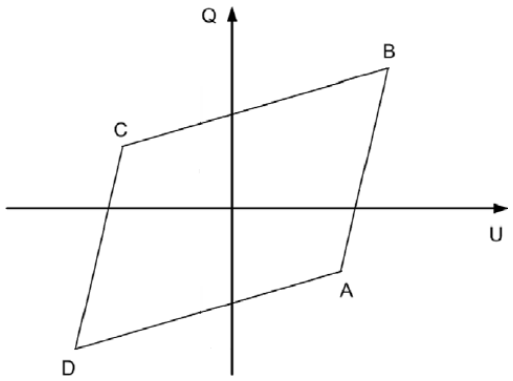


Figure II.2. Schematic of a typical Q-V Lissajous Figure for a dielectric barrier discharge, after [75]. The slope AB and DC correspond to $C_{diel}$ and the slope DA and CB correspond to $C_{cell}$ [1].

Alternatively, the geometrically determined dielectric capacitance is given by:

$$C_{diel} = \frac{\epsilon_r \epsilon_0}{2 d_\epsilon} \cdot A \tag{II.A.4}$$

Example of the determination of $C_{cell}$ from the Lissajous Figures for model batches:

Get $Q, V$ model output during steady state:

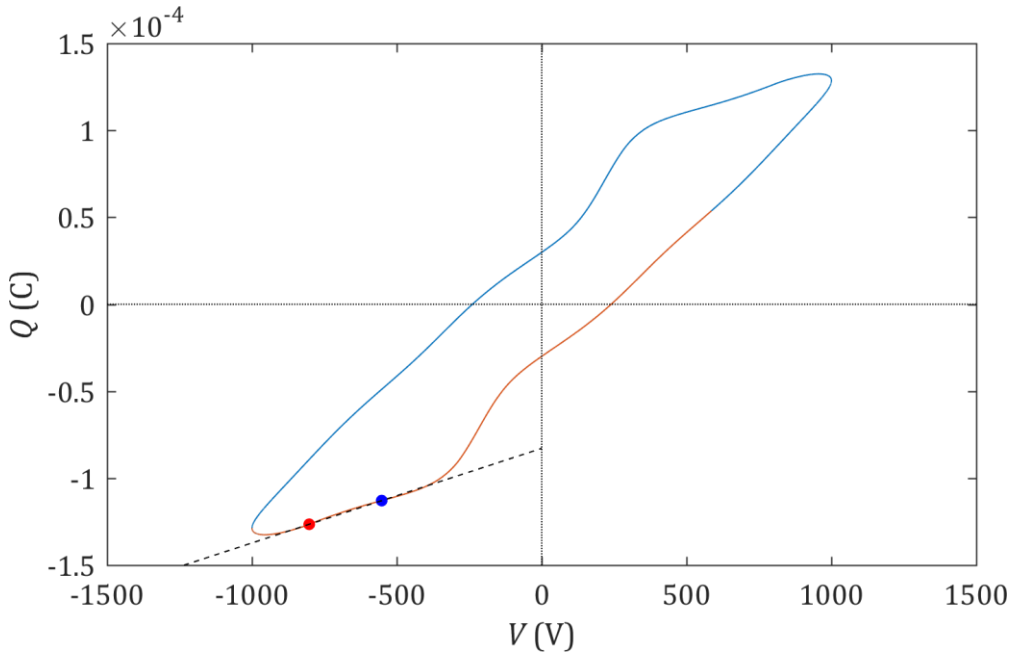


Figure II.3 Example of a Q-V Lissajous plot from a standard model model – see section 8.1, including all secondary electron emission processes. The red sections corresponds to Figure 4.

Take one "plasma off" phase and determine $dQ/dV$:

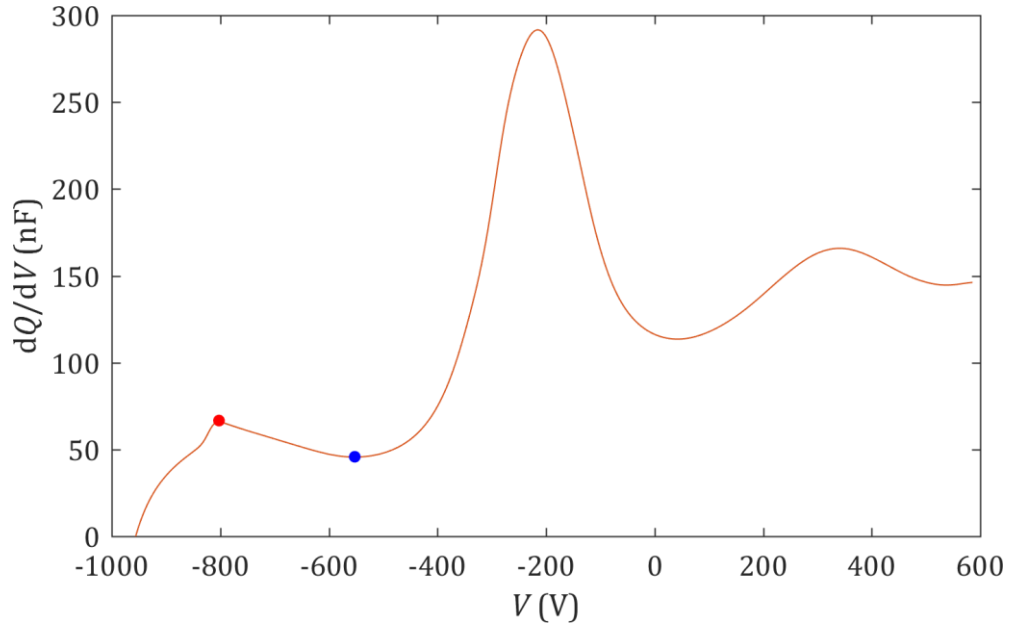


Figure II.4. Curve used in the determination of the slope in the Q-V Lissajous Figure. Corresponding to the red section in Figure 3.

A maximum (red dot) and minimum (blue dot) are observed related to the breakdown extinction and onset respectively. A linear fit between those points yields a good approximation of $C_{cell}$.

## II.B. Calculated cell capacitances for model batches

Current characteristics were considered over a wide range of the applied voltage (500 to 2500 V) and electron emission was considered for each species (metastables, atomic ions and molecular ions) separately over a range of (0 and 0.01 to 0.1 for $\gamma_p$). The background gas temperature is 450 K, the pressure is 1 atm, the dielectric thickness is 0.1 mm, the dielectric constant is 3.4 and the gas gap is 1 mm. The applied voltage is sinusoidal at a frequency of 200 kHz. The full chemistry set is used (Table 3.2). Here the calculated $C_{cell}$, used in the calculation of the plasma current, are reported for all model batches used in chapter 8.

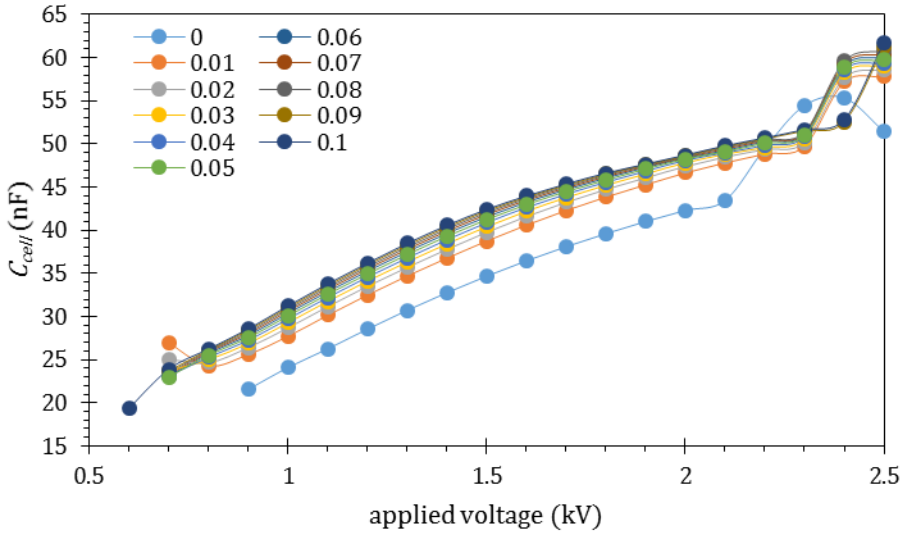


Figure II.5. The capacitance of the full reactor calculated for a model batch over a wide range of applied voltage and SEE coefficients of metastable atoms (legend). The electron emission by the remaining minority argon species is ignored. This Figures includes a set without any SEE.

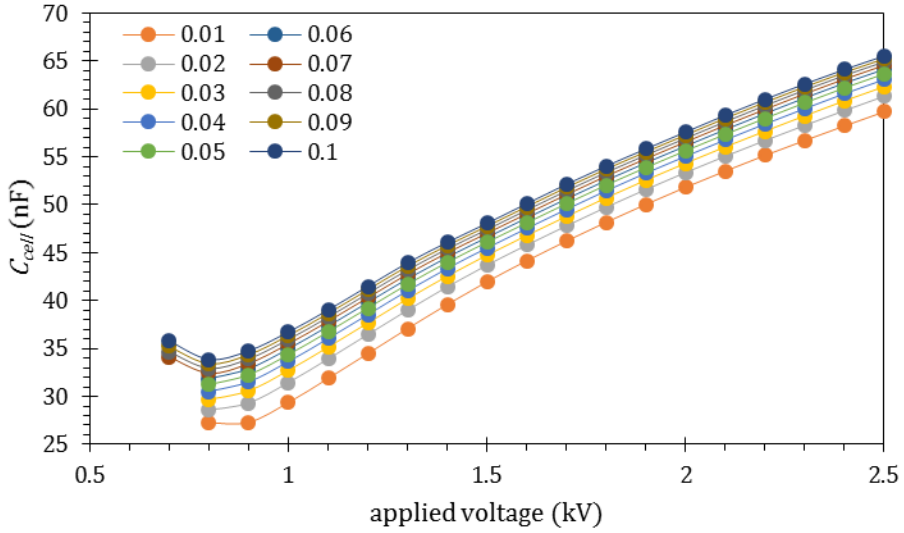


Figure II.6. The capacitance of the full reactor calculated for a model batch over a wide range of applied voltage and SEE coefficients of atomic ions (legend). The electron emission by the remaining minority argon species is ignored.

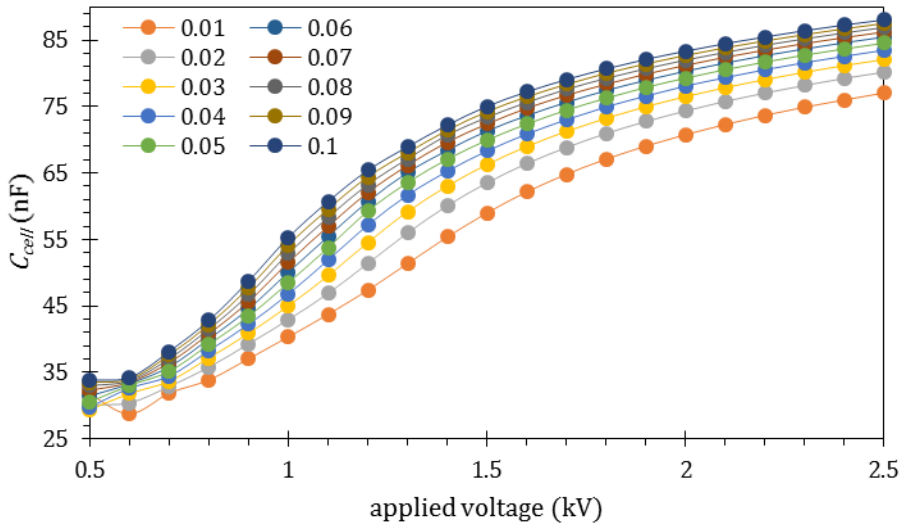


Figure II.7. The capacitance of the full reactor calculated for a model batch over a wide range of applied voltage and SEE coefficients of molecular ions (legend). The electron emission by the remaining minority argon species is ignored.

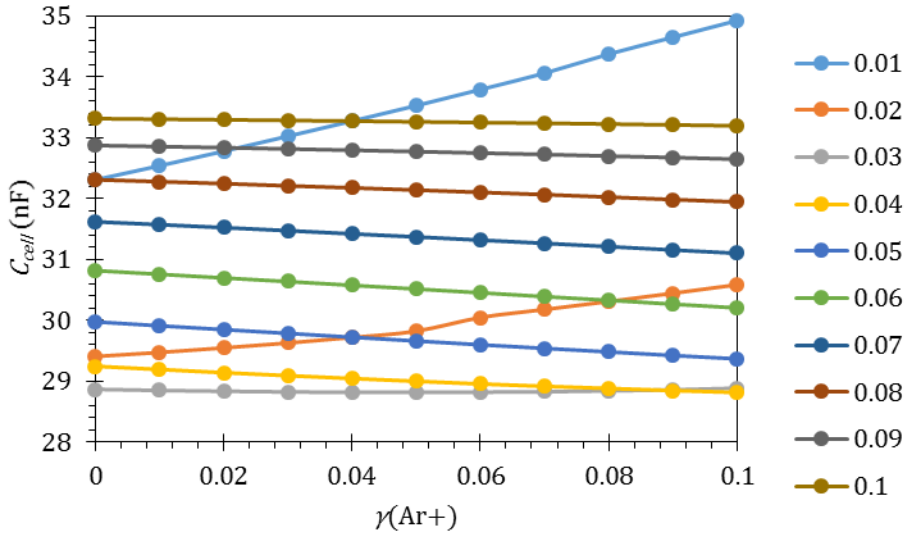


Figure II.8. The capacitance of the full reactor calculated for a model batch over a wide range of SEE coefficients of molecular ions (legend) and atomic ions (x axis). The SEE coefficient for metastables was set to 0.1. For an applied voltage of 500 V.

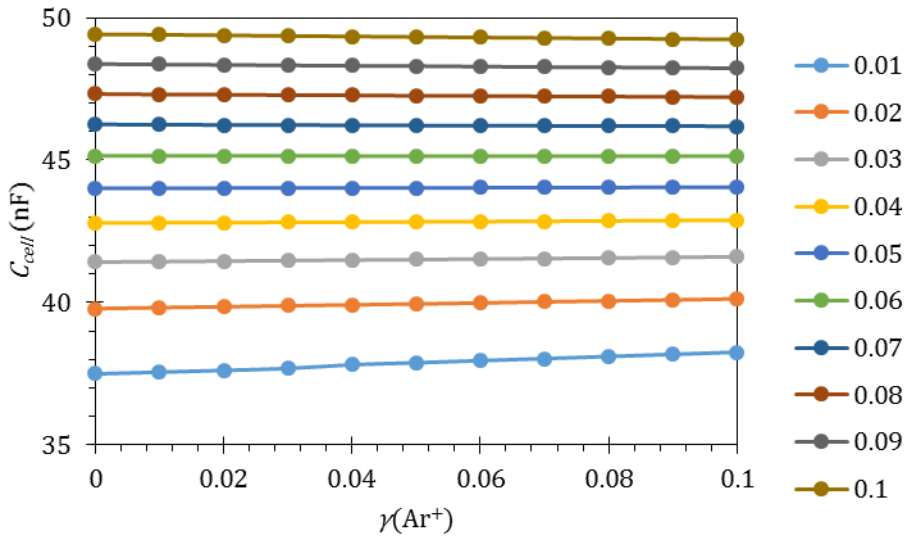


Figure II.9. The capacitance of the full reactor calculated for a model batch over a wide range of SEE coefficients of molecular ions (legend) and atomic ions (x axis). The SEE coefficient for metastables was set to 0.1. For an applied voltage of 900 V.

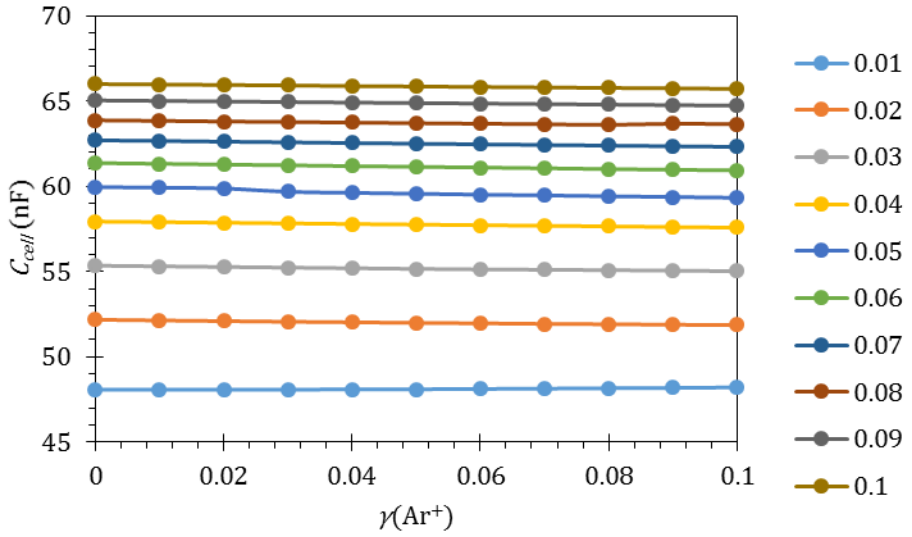


Figure II.10. The capacitance of the full reactor calculated for a model batch over a wide range of SEE coefficients of molecular ions (legend) and atomic ions (x axis). The SEE coefficient for metastables was set to 0.1. For an applied voltage of 1200 V.

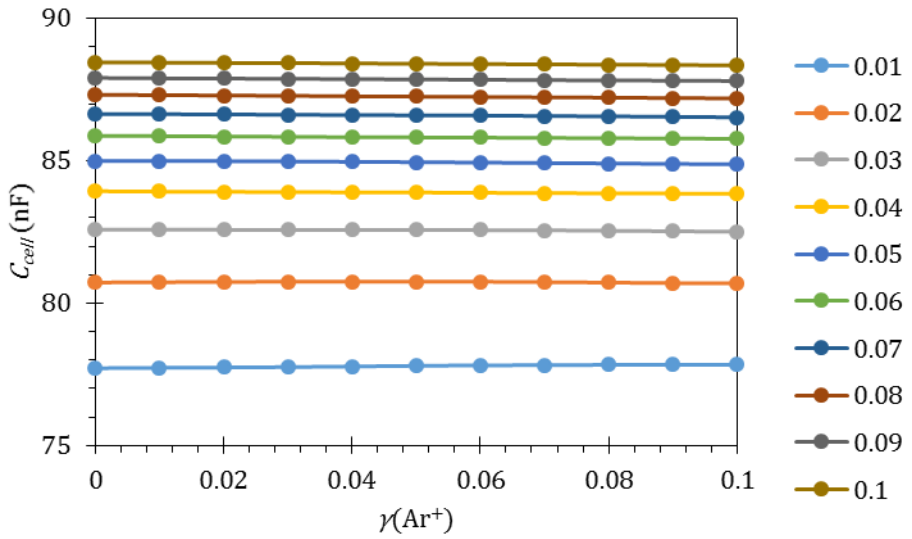


Figure II.11. The capacitance of the full reactor calculated for a model batch over a wide range of SEE coefficients of molecular ions (legend) and atomic ions (x axis). The SEE coefficient for metastables was set to 0.1. For an applied voltage of 2500 V.

# References


[1] F. Peeters, “The Electrical Dynamics of Dielectric Barrier Discharges,” 2015.

[2] S. Samukawa *et al.*, “The 2012 plasma roadmap,” *J. Phys. D. Appl. Phys.*, vol. 45, no. 25, 2012.

[3] T. Review and O. Access, “The 2017 Plasma Roadmap : Low temperature The 2017 Plasma Roadmap : Low temperature plasma science and technology,” 2017.

[4] D. Merche, N. Vandencasteele, and F. Reniers, “Atmospheric plasmas for thin film deposition: A critical review,” *Thin Solid Films*, vol. 520, no. 13, pp. 4219–4236, 2012.

[5] U. Kogelschatz, B. Eliasson, W. Egli, U. Kogelschatz, B. Eliasson, and W. E. D. D. Principle, “Dielectric-Barrier Discharges . Principle and Applications To cite this version : HAL Id : jpa-00255561,” 1997.

[6] R. D’Agostino, P. Favia, C. Oehr, and M. R. Wertheimer, “Low-temperature plasma processing of materials: Past, present, and future,” *Plasma Process. Polym.*, vol. 2, no. 1, pp. 7–15, 2005.

[7] U. Kogelschatz, “Atmospheric-pressure plasma technology,” *Plasma Phys. Control. Fusion*, vol. 46, no. 12 B, pp. 63–75, 2004.

[8] S. A. Starostin, M. Creatore, J. B. Bouwstra, M. C. M. Van De Sanden, and H. W. De Vries, “Towards roll-to-roll deposition of high quality moisture barrier films on polymers by atmospheric pressure plasma assisted process,” *Plasma Process. Polym.*, vol. 12, no. 6, pp. 545–554, 2015.

[9] S. A. Starostin, M. A. M. ElSabbagh, E. Aldea, H. de Vries, M. Creatore, and M. C. M. van de Sanden, “Formation and expansion phases of an atmospheric pressure glow discharge in a PECVD reactor via fast ICCD imaging,” *IEEE Trans. Plasma Sci.*, vol. 36, no. 4 PART 1, pp. 968–969, 2008.

[10] S. A. Starostin *et al.*, “On the formation mechanisms of the diffuse atmospheric pressure dielectric barrier discharge in CVD processes of thin silica-like films,” *Plasma Sources Sci. Technol.*, vol. 18, no. 4, p. 045021, 2009.

[11] S. A. Starostin *et al.*, “Dynamics of the atmospheric pressure diffuse dielectric barrier discharge between cylindrical electrodes in roll-to-roll PECVD reactor,” *Eur. Phys. J. Appl. Phys.*, vol. 71, no. 2, p. 20803, 2015.

[12] Y. Liu, “Understanding atmospheric plasma for functional thin film deposition on polymeric substrate,” 2018.

[13] Y. Liu, F. J. J. Peeters, and S. A. Starostin, “Improving uniformity of atmospheric-pressure dielectric barrier discharges using dual frequency excitation,” pp. 3–9, 2018.

[14] Y. Liu, S. A. Starostin, F. J. J. Peeters, M. C. M. Van De Sanden, and H. W. De Vries, “Atmospheric-pressure diffuse dielectric barrier discharges in Ar/O2gas mixture using 200 kHz/13.56 MHz dual frequency excitation,” *J. Phys. D. Appl. Phys.*, vol. 51, no. 11, 2018.

[15] J. van Dijk, K. Peerenboom, M. Jimenez, D. Mihailova, and J. van der Mullen, “The plasma modelling toolkit Plasimo,” *J. Phys. D. Appl. Phys.*, vol. 42, no. 19, p. 194012, 2009.

[16] D. B. Mihailova, “Sputtering hollow cathode discharges designed for laser applications,” Eindhoven University of Technology, The Netherlands, 2010.

[17] Y. B. Golubovskii, V. A. Maiorov, J. Behnke, and J. F. Behnke, "Modelling of the homogeneous barrier discharge in helium at atmospheric pressure," *J. Phys. D. Appl. Phys.*, vol. 36, no. 1, pp. 39–49, 2003.

[18] D. Petrovi??, T. Martens, J. Van Dijk, W. J. M. Brok, and A. Bogaerts, "Fluid modelling of an atmospheric pressure dielectric barrier discharge in cylindrical geometry," *J. Phys. D. Appl. Phys.*, vol. 42, no. 20, 2009.

[19] I. Radu, R. Bartnikas, and M. R. Wertheimer, "Frequency and Voltage Dependence of Glow and Pseudoglow Discharges in Helium Under Atmospheric Pressure," *IEEE Trans. Plasma Sci.*, vol. 31, no. 6 II, pp. 1363–1378, 2003.

[20] G. Gouda and F. Massines, "Role of excited species in dielectric barrier discharge mechanisms\nobserved in helium at atmospheric pressure," *1999 Annu. Rep. Conf. Electr. Insul. Dielectr. Phenom. (Cat. No.99CH36319)*, vol. 2, no. iii, pp. 496–499, 1999.

[21] F. Massines, N. Gherardi, N. Naudé, and P. Ségur, "Recent advances in the understanding of homogeneous dielectric barrier discharges," *Eur. Phys. J. Appl. Phys.*, vol. 47, no. 2, p. 22805, 2009.

[22] T. Martens, W. J. M. Brok, J. Van Dijk, and A. Bogaerts, "On the regime transitions during the formation of an atmospheric pressure dielectric barrier glow discharge," *J. Phys. D. Appl. Phys.*, vol. 42, no. 12, pp. 1–6, 2009.

[23] V. A. Maiorov and Y. B. Golubovskii, "Modelling of atmospheric pressure dielectric barrier discharges with emphasis on stability issues," *Plasma Sources Sci. Technol.*, vol. 16, no. 1, 2007.

[24] A. Sobota, F. Manders, E. M. Van Veldhuizen, J. Van Dijk, and M. Haverlag, "The role of metastables in the formation of an argon discharge in a two-pin geometry," *IEEE Trans. Plasma Sci.*, vol. 38, no. 9 PART 1, pp. 2289–2299, 2010.

[25] X. Li, R. Liu, P. Jia, K. Wu, C. Ren, and Z. Yin, "Influence of driving frequency on discharge modes in the dielectric barrier discharge excited by a triangle voltage," vol. 013512, 2018.

[26] T. Yoshinaga and H. Akashi, "Effects of secondary electron emission coefficients on Townsend's second ionization coefficient in argon dielectric barrier discharges," *IEEJ Trans. Electr. Electron. Eng.*, vol. 9, no. 5, pp. 459–464, 2014.

[27] G. J. M. Hagelaar, "Modeling of Microdischarges for Display Technology," Eindhoven University of Technology, The Netherlands, 2000.

[28] W. J. M. Brok, "Modelling of Transient Phenomena in Gas Discharges," Eindhoven University of Technology, The Netherlands, 2005.

[29] A. Sobota, "Breakdown processes in HID lamps," Eindhoven University of Technology, The Netherlands, 2011.

[30] The PLASIMO team, "PLASIMO website." [Online]. Available: https://plasimo.phys.tue.nl/. [Accessed: 18-Jun-2018].

[31] M. A. Lieberman and A. J. Lichtenberg, *Principles of plasma discharges and materials processing*. John Wiley & Sons, 2005.

[32] R. Y. Pai, E. W. Mcdaniel, and L. A. Viehland, "Transport properties of gaseous ions over a wide energy rang," *At. Data Nucl. Data Tables*, no. 3, 1976.

[33] J. F. J. Janssen, *Equilibrium and transport in molecular plasmas*. 2016.

[34] G. J. M. Hagelaar and L. C. Pitchford, "Solving the Boltzmann equation to obtain electron transport coefficients and rate coefficients for fluid models," *Plasma Sources Sci. Technol.*, vol. 14, no. 4, pp. 722–733, 2005.

[35] Y. Sakiyama and D. B. Graves, "Corona-glow transition in the atmospheric pressure RF-excited plasma needle," *J. Phys. D. Appl. Phys.*, vol. 39, no. 16, p. 3644, 2006.

[36] S. R. Sun, S. Kolev, H. X. Wang, and A. Bogaerts, "Coupled gas flow-plasma model for a gliding arc: Investigations of the back-breakdown phenomenon and its effect on the gliding arc characteristics," *Plasma Sources Sci. Technol.*, vol. 26, no. 1, 2017.

[37] S. Kolev and A. Bogaerts, "A 2D model for a gliding arc discharge," *Plasma Sources Sci. Technol.*, vol. 24, no. 1, 2015.

[38] M. Database, "No Title," 2017. [Online]. Available: http://www.lxcat.laplace.univ-tlse.fr. [Accessed: 01-Sep-2017].

[39] J. Gregório, P. Leprince, C. Boisse-Laporte, and L. L. Alves, "Self-consistent modelling of atmospheric micro-plasmas produced by a microwave source," *Plasma Sources Sci. Technol.*, vol. 21, no. 1, 2012.

[40] A. Bogaerts and R. Gijbels, "Role of Ar 2+ and Ar2 + ions in a direct current argon glow discharge: A numerical description," vol. 053305, 2010.

[41] N. Balcon, G. J. M. Hagelaar, and J. P. Boeuf, "Numerical model of an argon atmospheric pressure RF discharge," *IEEE Trans. Plasma Sci.*, vol. 36, no. 5 SUPPL. 4, pp. 2782–2787, 2008.

[42] Y. P. Raizer, *Gas Discharge Physics*. Springer-Verlag Berlin Heidelberg New York, 1991.

[43] J. P. Pavlik, J. K. Glosik, M. S. SiCha, M. Tichy, and P. P. Ek, "A Probe Method for Determination of Time Evolution of Metastable Atoms Density i n a Flowing Afterglow Plasma," *Langmuir*, vol. 80, pp. 437–448, 1990.

[44] A. Bultel, B. van Ootegem, A. Bourdon, and P. Vervisch, "Influence of Ar2+ in an argon collisional-radiative model," *Phys. Rev. E - Stat. Nonlinear, Soft Matter Phys.*, vol. 65, no. 4, p. 046406/1-046406/16, 2002.

[45] N. B. Kolokolov and A. B. Blagoev, "lonization and quenching of excited atoms with the production of fast electrons," *Physics-Uspekhi*, vol. 36, no. 3, p. 152, 1993.

[46] S. Neeser, T. Kunz, and H. Langhoff, "A kinetic model for the formation of excimers," *J. Phys. D. Appl. Phys.*, vol. 30, pp. 1489–1498, 1997.

[47] T. Holstein, "Imprisonment of resonance radiation in gases," *Phys. Rev.*, vol. 72, no. 12, pp. 1212–1233, 1947.

[48] T. Holstein, "Imprisonment of resonance radiation in gases. II," *Phys. Rev.*, vol. 83, no. 6, p. 1159, 1951.

[49] K. Engelen, P. Jacqmaer, and J. Driesen, "Electric and magnetic fields of two infinitely long parallel cylindrical conductors carrying a DC current," *Eur. Phys. J. Appl. Phys.*, vol. 64, no. 2, p. 24515, 2013.

[50] E. W. Weisstein, "Orthogonal Circles.," *From MathWorld--A Wolfram Web Resource.* .

[51] H. W. de V. S. A. Starostin, Welzel S, Sanden MCM van de, Bouwstra JB, "Thermometry of the atmospheric pressure high current dielectric barrier discharge in a cylindrical electrode geometry," in *Proceedings of the XXII Europhysics Conference on Atomic and Molecular Physics of Ionized Gases (ESCAMPIG)*, 2014, p. p.3-10-1.

[52] A. Salabaş and R. P. Brinkmann, "Non-neutral/quasi-neutral plasma edge definition for discharge models: A numerical example for dual frequency hydrogen capacitively coupled plasmas," *Japanese J. Appl. Physics, Part 1 Regul. Pap. Short Notes Rev. Pap.*, vol. 45, no. 6 A, pp. 5203–5206, 2006.

[53] T. Martens, "Numerical simulations of dielectric barrier discharges," p. 174, 2010.

[54] Z. L. Zhang *et al.*, "Numerical studies of independent control of electron density and gas temperature via nonlinear coupling in dual-frequency atmospheric pressure dielectric barrier discharge plasmas," *Phys. Plasmas*, vol. 23, no. 7, 2016.

[55] X. Li, Q. Zhang, P. Jia, J. Chu, P. Zhang, and L. Dong, "Characteristics of a micro-gap argon barrier discharge excited by a saw-tooth voltage at atmospheric pressure," *Phys. Plasmas*, vol. 24, no. 3, 2017.

[56] A. Sublet, C. Ding, J. L. Dorier, C. Hollenstein, P. Fayet, and F. Coursimault, "Atmospheric and sub-atmospheric dielectric barrier discharges in helium and nitrogen," *Plasma Sources Sci. Technol.*, vol. 15, no. 4, pp. 627–634, 2006.

[57] T. Martens, W. J. M. Brok, J. van Dijk, and A. Bogaerts, "On the regime transitions during the formation of an atmospheric pressure dielectric barrier glow discharge," *J. Phys. D. Appl. Phys.*, vol. 42, no. 12, p. 122002, 2009.

[58] X. Li, D. Niu, Z. Yin, T. Fang, and L. Wang, "Numerical simulation of operation modes in atmospheric pressure uniform barrier discharge excited by a saw-tooth voltage Numerical simulation of operation modes in atmospheric pressure uniform barrier discharge excited by a saw-tooth voltage," *Phys. Plasmas*, vol. 083505, no. 2012, pp. 1–7, 2014.

[59] A. Sobota *et al.*, "Ac breakdown in near-atmospheric pressure noble gases: I. Experiment," *J. Phys. D. Appl. Phys.*, vol. 44, no. 22, p. 224002, 2011.

[60] R. Bazinette, R. Subileau, J. Paillol, and F. Massines, "Identification of the different diffuse dielectric barrier discharges obtained between 50kHz to 9MHz in Ar/NH3 at atmospheric pressure," *Plasma Sources Sci. Technol.*, vol. 23, no. 3, 2014.

[61] T. Gans, D. O'Connell, V. S. der Gathen, and J. Waskoenig, "The challenge of revealing and tailoring the dynamics of radio-frequency plasmas," *Plasma Sources Sci. Technol.*, vol. 19, no. 3, p. 34010, 2010.

[62] T. Gans, V. der Gathen, and H. F. Döbele, "Prospects of Phase Resolved Optical Emission Spectroscopy as a Powerful Diagnostic Tool for RF-Discharges," *Contrib. to Plasma Phys.*, vol. 44, no. 5-6, pp. 523–528.

[63] D. W. Liu, F. Iza, and M. G. Kong, "Electron heating in radio-frequency capacitively coupled atmospheric-pressure plasmas," *Appl. Phys. Lett.*, vol. 93, no. 26, p. 261503, Dec. 2008.

[64] X. Y. Liu *et al.*, "The discharge mode transition and O(5p1) production mechanism of pulsed radio frequency capacitively coupled plasma," *Appl. Phys. Lett.*, vol. 101, no. 4, p. 43705, Jul. 2012.

[65] F. Iza, J. K. Lee, and M. G. Kong, "Electron Kinetics in Radio-Frequency Atmospheric-Pressure Microplasmas," *Phys. Rev. Lett.*, vol. 99, no. 7, p. 75004, Aug. 2007.

[66] J. Schulze, Z. Donkó, E. Schüngel, and U. Czarnetzki, "Secondary electrons in dual-frequency capacitive radio frequency discharges," *Plasma Sources Sci. Technol.*, vol. 20, no. 4, p. 45007, 2011.

[67] T. Gans *et al.*, "Frequency coupling in dual frequency capacitively coupled radio-frequency plasmas," *Appl. Phys. Lett.*, vol. 89, no. 26, p. 261502, Dec. 2006.

[68] J. Waskoenig and T. Gans, "Nonlinear frequency coupling in dual radio-frequency driven atmospheric pressure plasmas," *Appl. Phys. Lett.*, vol. 96, no. 18, p. 181501, May 2010.

[69] J. T. Gudmundsson and E. G. Thorsteinsson, "Oxygen discharges diluted with argon: Dissociation processes," *Plasma Sources Sci. Technol.*, vol. 16, no. 2, pp. 399–412, 2007.

[70] J. T. Gudmundsson, D. Lundin, N. Brenning, M. A. Raadu, C. Huo, and T. M. Minea, "An ionization region model of the reactive Ar/O2 high power impulse magnetron sputtering discharge," *Plasma Sources Sci. Technol.*, vol. 25, no. 6, 2016.

[71] L. P. T. Schepers, "Illuminating the plasma - particle interaction," Technische Universiteit Eindhoven, 2018.

[72] M. Moravej, X. Yang, R. F. Hicks, J. Penelon, and S. E. Babayan, "A radio-frequency nonequilibrium atmospheric pressure plasma operating with argon and oxygen," *J. Appl. Phys.*, vol. 99, no. 9, pp. 1–7, 2006.

[73] G. Park, H. Lee, G. Kim, and J. K. Lee, "Global model of He/O2 and Ar/O2 atmospheric pressure glow discharges," *Plasma Process. Polym.*, vol. 5, no. 6, pp. 569–576, 2008.

[74] Y. Liu, S. Welzel, S. A. Starostin, M. C. M. Van De Sanden, R. Engeln, and H. W. De Vries, "Infrared gas phase study on plasma-polymer interactions in high-current diffuse dielectric barrier discharge," *J. Appl. Phys.*, vol. 121, no. 24, 2017.

[75] D. Mei, X. Zhu, Y. He, J. Yan, and X. Tu, "Plasma-assisted conversion of CO2 in a dielectric barrier discharge reactor: Understanding the effect of packing materials," *Plasma Sources Sci. Technol.*, 2015.